Strongly Coupled Systems:
From Quantum Antiferromagnets to Unified
Models for Superconductors

by

Victor Chudnovsky

S.B. Physics, Massachusetts Institute of Technology (1996)
S.B. Mathematics, Massachusetts Institute of Technology (1996)

Submitted to the Department of Physics
in partial fulfillment of the requirements for the degree of

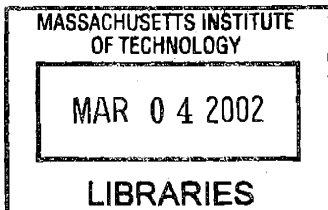Doctor of Philosophy

at the

MASSACHUSETTS INSTITUTE OF TECHNOLOGY

February 2002

Author . . . .
Department of Physics
October 5, 2001

Certified by . . . .
Uwe-Jens Wiese
Associate Professor of Physics
Thesis Supervisor

Accepted by . . . .
Thomas J. Greytak
Professor of Physics
Associate Department Head for Education

Strongly Coupled Systems:

From Quantum Antiferromagnets to Unified Models for

Superconductors

by

Victor Chudnovsky

Submitted to the Department of Physics
on October 5, 2001, in partial fulfillment of the
requirements for the degree of
Doctor of Philosophy

Abstract

I discuss the significance of the antiferromagnetic Heisenberg model (AFHM) in both high-energy and condensed-matter physics, and proceed to describe an efficient cluster algorithm used to simulate the AFHM. This is one of two algorithms with which my collaborators and I were able to obtain numerical results that definitively confirm that chiral perturbation theory, corrected for cutoff effects in the AFHM, leads to a correct field-theoretical description of the low-temperature behavior of the spin correlation length in various spin representations S. Using a finite-size-scaling technique, we explored correlation lengths of up to 10^5 lattice spacings for spins S=1 and 5/2. We show how the recent prediction of cutoff effects by P. Hasenfratz is approached for moderate correlation lengths, and smoothly connects with other approaches to modeling the AFHM at smaller correlation lengths.

I also simulate and discuss classical antiferromagnetic systems with simultaneous $SO(M)$ and $SO(N)$ symmetries, which have been proposed as models for magnets in external fields and for electronic and color superconductors. After detailing the algorithms which were employed, I present results for the various observables which confirm the existence of the expected ordered and disordered phases. I obtain a preliminary phase diagram from these systems, from which the location of an expected bicritical point may be estimated. This is a necessary first step in determining whether the point exhibits a dynamically-generated enhanced symmetry, a possibility first suggested by Wiese and Chandrasekharan but not fully resolved in three dimensions.

Thesis Supervisor: Uwe-Jens Wiese
Title: Associate Professor of Physics

Acknowledgments

I would like to thank Uwe-Jens Wiese for being my mentor and advisor during my years of graduate school. His grasp of physics and ability to clearly explain complex concepts have awed and inspired me.

My collaborators, Bernard B. Beard and Peter Keller-Marxer, have been the source of many interesting exchanges as we worked together to understand the results of the quantum Heisenberg antiferromagnet. It is no exaggeration to say that the first project described in this thesis would not have reached its present stage without them.

I would also like to thank the professors who made my physics experience at MIT (all nine years of it!) challenging and rewarding. In particular, I would like to thank John Negele, Patrick Lee, and Senthil Todadri for sitting on my thesis committee, and Richard Brower for interesting discussions over the years on quantum spins and quantum links.

My colleagues and friends at the Center for Theoretical Physics have been a constant source of support during my graduate career: Jürgen Cox, Brian Fore, Leonidas Pantelidis, and Eugene Shuster. Thank you! I also wish to express my appreciation to Boris Schlittgen, with whom I labored through several graduate classes and with whom I first embarked on the $SO(M) \otimes SO(N)$ project which comprises the second half of this thesis.

Thanks, too, to the friends in my life who heard me wax both enthusiastic and stressed about student life: Bill Cattey, Christine Hung, Kevin McLellan, Michael Saginaw, and David Sledge. I'm especially grateful to David Muldowney for his love and support.

And thanks to my parents, Myriam Gersenovic and Jorge Chudnovsky, for making the best opportunities available to me, and encouraging me all my life to be my best.

Contents

List of Figures

List of Tables

8

Chapter 1

Introduction

From subatomic particles to neutron stars, from the freezing lows of superconductors to the scorching highs of plasmas, the world around us is endowed with a rich collection of strongly-interacting systems. The high-energy physicist is still struggling to understand the non-perturbative aspects of the theory know as quantum chromodynamics (QCD), while the condensed matter physicist is still unraveling the mysteries behind superconductivity. With few analytical tools available to tackle these problems, they have frequently turned to numerical simulation to gain insight into the underlying physics. "Simulation," however, is fraught with its own pitfalls and complications, and practitioners often need to simplify their models so as to capture some of the interesting features while making their analyses amenable to the computer.

This dissertation is motivated by QCD in two strong-coupling regimes: low energy and non-zero density. The low-energy regime describes ordinary matter: how exactly *are* quarks held together to form larger subatomic particles like protons and neutrons? The non-zero density regime describes some compact stars: are neutron stars really a fundamentally *different* form of matter than we have here on earth? The complexity of these two regimes continues to hinder direct numerical simulation. Nevertheless, one can learn how to build better simulations, and at the same time gain some physical insight, by studying toy models with similar features. In this thesis, I focus on two related systems, the Heisenberg quantum and classical antiferromagnets, as condensed matter analogues of QCD at low energy and at non-zero

density, respectively. The analogy is not perfect, yet these two models have much to teach us about building more sophisticated simulations in the future. Furthermore, the two systems simulated herein are interesting in their own right: the former as a description of superconducting substrates, and the latter as a mechanism behind superconductivity.

1.1   QCD at Low Energy

Confinement

Quantum chromodynamics introduces the strong force into the standard model of particle physics. It describes how the fundamental building blocks of matter, quarks, interact with each other through the exchange of strong force carriers, gluons, in a manner somewhat reminiscent of electrical particles interacting through the exchange of photons in quantum electrodynamics (QED). The fundamental difference between QCD and QED is that there is only one electric charge while there are three strong charges (whimsically called colors). QCD is postulated to be invariant under a local ("gauge") symmetry that changes the color of any quark; this postulate gives rise to the eight gluons, which themselves carry color charge. This contrasts with QED, where a much smaller symmetry gives rise to the single, neutral photon.

The symmetry structure of QCD together with the existence of three colors and six different quark flavors leads to "asymptotic freedom:" the interaction between color charges is weak at high energies and strong at low energies. QCD also exhibits confinement: isolated color-charged objects are not observed in nature because the attractive potential between them grows linearly with distance. It takes high energies, such as those momentarily produced at accelerators, to separate a color-neutral composite into weakly-interacting color-carrying particles that can be analyzed through perturbation theory. At low energies, quarks combine to form mesons and hadrons (like the familiar proton and neutron), while gluons can combine to form color-neutral glueballs.

Attempts to understand QCD numerically have often focused on putting the the-

ory, formulated as a thermodynamic system of classical fields, in a lattice approximation to the space-time continuum assumed in the standard model. The lattice approach, first pioneered by Wilson[1], is useful in that it provides a natural way to deal with the infinities present in the continuum field theory, and in that it is non-perturbative and could, in principle, probe the low-energy dynamics of interest. Unfortunately, to get back to the real world, finer and finer lattices must be taken so as to approach the continuum again. In this limit, simulations suffer from "critical slowing down:" it takes more and more computer time to simulate the physically interesting events. Furthermore, because the classical fields are continuous variables and because finer and finer lattices must be taken, obtaining precise numerical results becomes computationally prohibitive.

D-Theory

Over the past few years, Wiese and collaborators have been investigating a novel approach to lattice simulations: D-theory[2, 3, 4, 5]. As in traditional lattice field theories, the fields are assumed to live at points on a lattice rather than everywhere in space-time. Now, however, the fields are no longer classical variables but become instead quantum operators. The advantage of simulating such a quantum system is that each lattice site can now take on one of a finite, rather than infinite, number of values— a drastic reduction in the computations involved. The price one pays is the introduction of an extra dimension not present in the original theory. One can recover the physics of the classical fields, however, through the mechanism of dimensional reduction: fields correlated over distances much longer than the length β of the extra dimension can be averaged in blocks of size β, obtaining the original model. This mechanism is depicted in Fig 1-1, where the large correlation length allows the fields in the $(d + 1)$-dimensional theory to be averaged into fields living in d dimensions.

One advantage of the D-theory formulation, then, is that there are only a finite number of possible states at each site. Another advantage is that D-theory allows the use of "cluster algorithms," thus potentially reducing or eliminating critical slowing
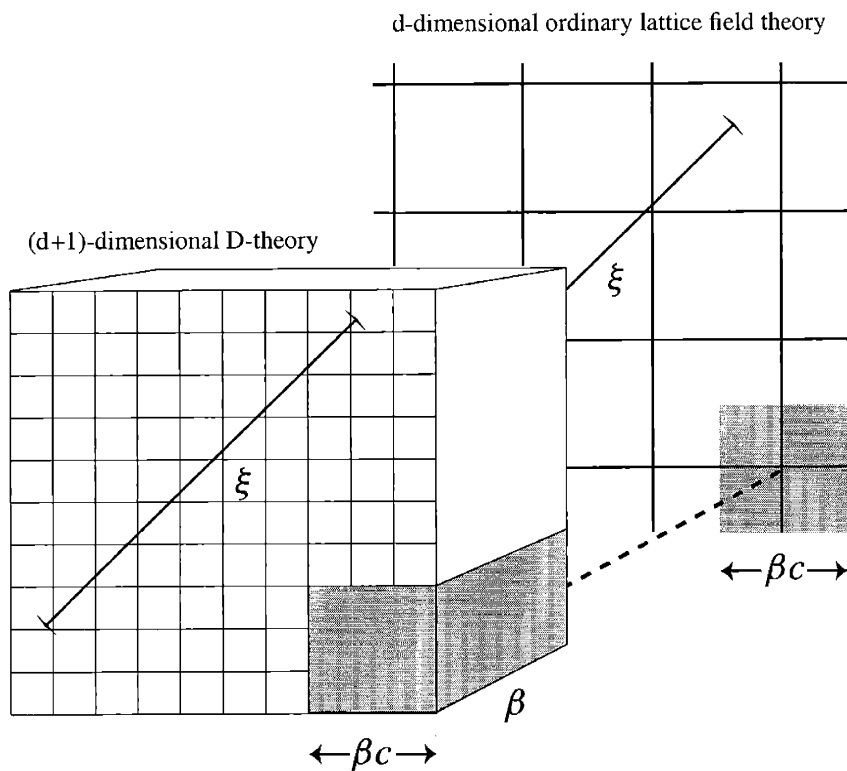
Figure 1-1: Dimensional reduction of a field theory. The fields living in $(d + 1)$-dimensional space-time are correlated over distances much larger than the extent of the extra dimension $(\xi \gg \beta)$. They can be averaged out to obtain the fields of a d-dimensional theory.

down. These algorithms create clusters of spins over physically-correlated regions and then flip them to generate new configurations of the system. The common simulation problem of wastefully proposing and rejecting small changes is thus circumvented, making much more efficient use of computer time. Furthermore, cluster algorithms in turn often allow "improved estimators" to be constructed for various observables; these are quantities which use cluster properties to arrive at measurements more precise than those obtained by naively averaging only those configurations actually created on the computer. Both cluster algorithms and improved estimators are used in the simulations described in the first part of this thesis, and are explained in more detail in Chapter 3.

The antiferromagnet as a toy model

While a D-theory formulation of QCD has already been devised, finding cluster algorithms to simulate it has remained a challenge. In order to gain insight into what such an algorithm may be, the focus has lain on simulating toy models in order to understand what works and what doesn't in cluster algorithms. One such model is the the 2-d $O(3)$ model, which shares several features with QCD: asymptotic freedom, a mass gap (*i.e.* the fields may be correlated over large but never infinite distances), and topologically non-trivial field configurations such as instantons. When formulated as a D-theory, the resulting quantum system is the Heisenberg antiferromagnet describing interacting spins, which, at sufficiently low temperatures, anti-align with their nearest neighbors to generate a "staggered magnetization." Furthermore, the Heisenberg model is interesting in its own right as a description of materials which, when doped with impurities, become high-temperature superconductors; it has been the subject of much theoretical analysis and simulation in the condensed matter community. In simulating this system, my collaborators and I employed two recent improvements in cluster algorithms: a technique to treat the extra dimension as continuous in our simulations (as first described by Beard and Wiese in Ref. [6]), and a formulation that extends the cluster algorithm to arbitrary values of the spin (an original formulation not heretofore described by our group, although independently used by others[7]). As described herein, the resulting simulations have enabled us to confirm theoretical predictions in various temperature ranges, agree with experimental data, and probe regimes where the correlation length becomes astronomical. All this while learning how to craft a cluster algorithm for QCD!

1.2   QCD at Non-zero Density

Color Superconductivity

Low temperature is not the only regime in which QCD is strongly interacting. Since quarks are fermionic particles, no two can be in the same energy state. Hence, at high

densities, even if the temperature is low, some of the quarks must be quite energetic (just like electrons in a superconductor) and be weakly coupled to one another through the strong force. Just as in electronic superconductors, an arbitrarily weak attractive interaction is enough to induce superconductivity. Unlike electronic superconductors, where the attractive interaction between otherwise repulsive electrons is indirectly generated by the vibrational degrees of freedom ("phonons") of the atomic lattice, so-called color superconductors arise from the direct attractive potential between the quarks. The quarks are again highly correlated, not due to confinement now at these high densities, but rather through color superconductivity to form non-color-neutral states.

The color superconducting phase is also marked by a change in the chiral symmetry of the quarks. The simplified model of QCD with two massless flavors (rather than the six found in nature) turns out to be invariant under *separate* global rotations of left-handed and right-handed quarks, $SU(2)_L \otimes SU(2)_R$. At low energies, such as ordinary matter, this symmetry breaks spontaneously and the theory is invariant only under *simultaneous* rotations of left- and right-handed quarks, the smaller symmetry group $SU(2)_{L=R}$. Thus, at low temperature and density, the quarks are in color-neutral, chirally broken states, while at low temperatures and high densities, the quarks are bound in a superconducting, chirally-symmetric condensate. At high enough temperatures, the quarks are free and have chiral symmetry.

Numerical simulation of the color superconducting phase, which would appear to be amenable due to the weak color coupling, remains problematic because of the high densities involved. The density is driven by a chemical potential μ in the the system, which, unfortunately, introduces a "sign problem" in numerical simulations. The crux of the sign problem is that quantities which are usually interpreted as probabilities in formulating algorithms now become negative or even complex. While significant breakthroughs have been made in solving the sign problem in simpler systems [8, 9, 10, 11, 12, 13, 14], these techniques have not yet been successfully applied to QCD. Furthermore, there are more straightforward ways to gain qualitative insight into the superconducting phase of QCD, as I now discuss.

The antiferromagnet as a toy model

The three phases of two-color QCD are reminiscent of those of two other systems. The first is an anisotropic antiferromagnet in a magnetic field **B**. At low temperatures, a small field generates a staggered magnetization along **B**, while a large field causes the staggered magnetization to flop onto the plane perpendicular to **B**. At high temperatures, the spins are randomly oriented. The other system is a high-temperature cuprate superconductor. There, the low temperature, low impurity density regime is the so-called Néel phase in which a spontaneous staggered magnetization arises. The low temperature, high density phase is the high-temperature superconductor. Finally, the high-temperature regime describes the metallic phase of the cuprates. These phase diagrams thus have a similar structure to that of QCD with two quark flavors. The generic phase diagram for all three systems is pictured in Fig. 1-2.

Fueled by these analogies, one can investigate the symmetry properties of color superconductors using models similar to those employed for the condensed matter systems. One collects the degrees of freedom into a single "supervector" whose first M components describe the $SO(M)$ symmetry (*e.g.* chiral symmetry) and whose last N components describe the $SO(N)$ symmetry (*e.g.* the color condensate). These vectors are then used to formulate a physical system that exhibits the relevant interactions between the M and N components. It turns out that all three systems involve rotational symmetries and can thus be represented as an antiferromagnet in a magnetic field— the only features that change from one toy model to the other are the values of M and N, that is, the number of components of the supervector. In the case of the antiferromagnet in a magnetic field, it is known that at point "bc" in the phase diagram, the $SO(M)$ and $SO(N)$ symmetries are enhanced to an $SO(M + N)$ symmetry[15]. It is then natural to ask whether in the electronic and color superconductors a similar unification takes place. Chandrasekharan and Wiese studied this problem analytically; their work in $4 - \epsilon$ spatial dimensions suggests that the electronic superconductor *may* display an enhanced symmetry but the color superconductor probably does not. It is not clear, however, whether this analysis remains

valid when $\epsilon = 1$.

Here, then, I aim to verify these claims numerically in three dimensions. Once again, a Monte Carlo algorithm is used, albeit a classical one now, as the chemical potential present in these models could again introduce a sign problem in the quantum formulation. The results are then used to map the phase diagrams and to determine the neighborhood in which the bicritical point with a possible enhanced symmetry may be found.

1.3 Outline

This dissertation will describe the work and results obtained in analyzing the quantum Heisenberg model and the classical $SO(M) \otimes SO(N)$ model. In Chapter 2, I describe the Heisenberg model in more detail and quote the theoretical predictions developed by Hasenfratz and Niedermayer, among others. I then explain the simulation algorithm in Chapter 3, and present an analysis of the results in Chapter 4. Chapters 2 and 4 are largely based both on an upcoming paper coauthored with B.B. Beard and P. Keller-Marxer[16], a draft version of which appears in Ref. [17]. The results have already been made available in Ref. [18].

Chapter 5 will then switch gears to explain more fully the $SO(M) \otimes SO(N)$ model and its relationship to QCD; this chapter is based on a paper I coauthored with U.-J. Wiese, S. Chandrasekharan, and B. Schlittgen[19]. The simulation algorithms are presented in some detail in Chapter 6, and the results are discussed in Chapter 7. The last chapter includes conclusions and final comments.
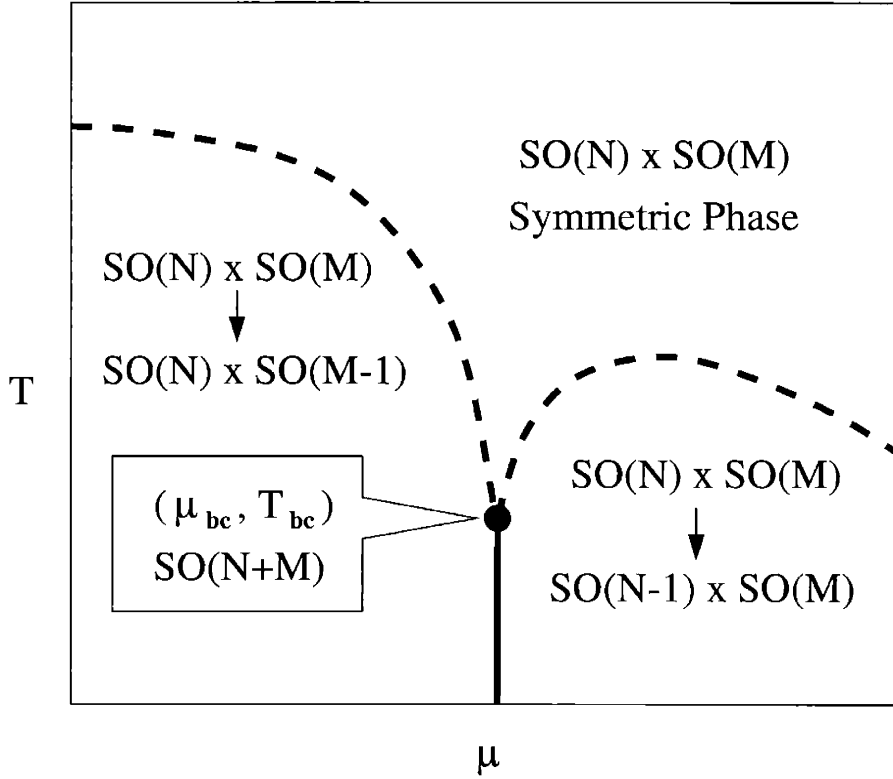
Figure 1-2: Conjectured phase diagram of $n_f = 2$ QCD and analogous systems. For QCD at non-zero density μ, $M = 4$, $N = 6$: the $SO(M)$ symmetry is chiral symmetry, while the $SO(N)$ symmetry is color symmetry. Analogously, for an antiferromagnet in a magnetic field μ ($M = 1$, $N = 2$), the component of the staggered magnetization along the direction of the field exhibits the $SO(M)$ symmetry, while the perpendicular components exhibit the $SO(N)$ symmetry. For an electronic superconductor ($M = 3$, $N = 2$), the staggered magnetization displays the $SO(M)$ symmetry while the Cooper pair condensate displays the $SO(N)$ symmetry; the impurity concentration is driven by μ.

Chapter 2

The Heisenberg Antiferromagnet

The discovery of high-temperature superconductivity in lamellar copper-oxides has revived interest in the two-dimensional quantum Heisenberg model. It was found[20] that the magnetic properties of undoped insulators and precursors with Cu-O planes, such as $Sr_2CuO_2Cl_2$ or La_2CuO_4, are well described by the spin $S = 1/2$ square-lattice quantum Heisenberg antiferromagnet with isotropic nearest-neighbor coupling (AFHM). There exist as well materials which are accurately described by the Heisenberg model in higher spin representations, such as K_2NiF_4 (S=1) and Rb_2MnF_4 and $KFeF_4$ (S=5/2). It is suspected that the quantum antiferromagnetic background plays a role in the generation of high-T_c superconductivity in the doped cuprates.

Theoretical and experimental interest[21] in the role of quantum fluctuations in the AFHM also increased with the realization that the model can undergo a sequence of crossovers[22, 23, 24, 25, 26], depending on temperature, spin coupling constant, and spin magnitude. Furthermore, it was realized that the low-temperature physics of the AFHM is dominated by magnon interactions which are described by the quantum field theory of the $O(3)$ non-linear σ-model, which allows analytic calculations in the framework of chiral perturbation theory. In fact, several analytic predictions[27, 28, 29, 30, 31] for the AFHM were derived from this quantum field theory, which, as mentioned in the introduction, shares qualitative features with QCD.

The field-theoretical prediction for the AFHM spin correlation length $\xi(T)$ agrees rather well[32] with neutron scattering measurements on $S = 1/2$ antiferromagnets

such as $Sr_2CuO_2Cl_2$ for the regime $\xi \leq 200$ lattice spacings a accessible in experiment. In the past decade, efficient $S = 1/2$ quantum Monte Carlo (QMC) algorithms offered "exact" AFHM data, unbiased by numerical approximations or structural details of real materials. This made it possible to validate the predictions of field theory accurately for the $S = 1/2$ AFHM over a broad range of correlation lengths[33] $\xi/a \approx 200 - 10^5$.

However, the agreement between the field-theoretical prediction, experimental measurement, and QMC results seemed to be constrained to the quantum limit $S = 1/2$. Recent experimental measurements[34, 35, 36] on higher-spin antiferromagnets like La_2NiO_4 ($S = 1$) and Rb_2MnF_4 ($S = 5/2$), as well as theoretical calculations[26, 37] and an $S = 1$ simulation[7] showed large deviations from the field-theoretical prediction for higher spins $S > 1/2$, with a strong dependence on S. These results suggest a serious discrepancy even at very large correlation lengths. This is highly unsatisfactory on theoretical grounds[38], as will be discussed later. In a recent publication, Hasenfratz[38] argued that this discrepancy is due to cutoff effects in the AFHM. He used spin-wave expansion to calculate the cutoff effects, and showed a proper way to incorporate them into the field-theoretical prediction for the correlation length.

In the course of this project, my collaborators and I[18] obtained QMC data for the correlation length of the full range of spins $S \leq 5/2$ up to $\xi/a \approx 10^5$, and also some complementary data in the extreme range up to $\xi/a \sim 10^{30}$. To our knowledge, the only QMC study available so far for a higher-spin AFHM was[7] for $S = 1$, covering very moderate $\xi/a < 25$. We show that the discrepancy between AFHM correlation length and field-theoretical prediction indeed persists at large correlation lengths $\xi/a \gg 10^5$. On the other hand, our results definitively confirm that the cutoff-corrected prediction describes the AFHM correlation length down to moderate $\xi(T) = \mathcal{O}(100)$ lattice spacings for all spins.

2.1 The Model

The Heisenberg model is formulated in terms of the interactions between quantum spins $\mathbb{S}$ on adjacent sites of a 2-d square lattice with an even number L of sites along each dimension and periodic boundary conditions:

$$\mathbb{H} = J \sum_{<xy>} \mathbb{S}_x \cdot \mathbb{S}_y \tag{2.1}$$

$$\left[\mathbb{S}_x^i, \mathbb{S}_y^j\right] = i\epsilon^{ijk}\mathbb{S}_x^k \delta_{x,y}$$

Here, $< xy >$ denotes nearest neighbor sites on the lattice, and the quantum spins $\mathbb{S}_x$ are all in an arbitrary spin S representation: $\mathbb{S}_x^2 = S(S+1)$.

In the case of antiferromagnets, which we consider here, $J > 0$. Since the total spin operator commutes with this Hamiltonian,

$$\left[\mathbb{H}, \sum_x \mathbb{S}_x\right] = 0,$$

the system has a global $SO(3)$ symmetry. As is often the case with quantum systems, it is useful to consider the classical analogue of this system to obtain some insight into how the quantum version behaves. The classical Hamiltonian has the same form, but the $\mathbb{S}_x$ are interpreted as classical unit vectors living on each site.

At low temperatures, the AFHM exhibits long range antiferromagnetic order. In the classical version, each spin tends to anti-align with its neighbors. In the process, a particular direction in space is singled out as the (staggered) magnetization direction: the symmetry breaks from $SO(3)$, rotations in three-dimensional space, to $SO(2)$, rotations in the plane. Similarly, the quantum system also exhibits spontaneous symmetry breaking[1][6, 40, 41], a fact which has been verified experimentally[32, 42].

The partition function of the quantum system, eq. (2.1), can be formulated as a

---

[1]This is rigorously established only for $S \geq 1$ [39]. However, approximate analytical and numerical results suggest that $S = 1/2$ is also in the broken phase [40].

path integral in Euclidean time of an $SO(3)$ classical model. According to Goldstone's theorem, two massless bosons (which in this case are called "magnons" or "spin-waves") are created by the $SO(3) \rightarrow SO(2)$ symmetry breaking, and are described by fields that live in the coset space $SO(3)/SO(2) = S^2$, the unit sphere. These magnons arise from the low-energy collective excitations of the quantum spins around the spontaneously-chosen magnetization direction.

The magnon dynamics can be described by chiral perturbation theory[43]. Chiral perturbation theory (CPT) is a framework for constructing low-energy effective theories; the name comes from its initial application to the study of pion decay. The low-energy effective action is obtained by writing all possible interactions of the magnons that respect the symmetries of the theory. The S^2 magnons $\mathbf{n}$ are then unit three-vectors $\mathbf{n}^2 = 1$ in three dimensions, and to lowest order the effective theory contains only two parameters, the spin stiffness ρ_s and the spin-wave velocity c:

$$\mathcal{A}_{\text{eff}} = \frac{\rho_s}{2} \int_0^\beta dx_3 \int d^2x \left[\partial_i \mathbf{n} \partial_i \mathbf{n} + \frac{1}{c^2} \partial_3 \mathbf{n} \cdot \partial_3 \mathbf{n} \right] \tag{2.2}$$

Here, the index i runs over the physical space-time dimensions 1 and 2 only, and not along the extra dimension 3 whose extent $\beta = 1/T$ is driven by the finite temperature of the system. When the correlation length ξ of this 3-d theory is much greater than this extra dimension, $\xi \gg \beta$, the system dimensionally reduces to two dimensions, as remarked in the introduction (see Figure 1-1): to lowest order, one may drop the ∂_3 derivatives in eq. (2.2), so that the leading part of the action becomes the 2-d $O(3)$ model,

$$\mathcal{S}_\sigma = \frac{1}{2g_0} \int d^2x \; \partial_\mu \mathbf{n} \, \partial_\mu \mathbf{n} \,, \quad \mathbf{n}^2 = 1 \,, \tag{2.3}$$

with $g = 1/\beta\rho_s$. However, the Mermin-Wagner-Coleman theorem[44, 45] rules out interacting massless Goldstone bosons in two dimensions at non-zero temperatures. The correlation length ξ is thus finite and the magnons acquire a mass $m \propto \xi^{-1}(T)$.

2.2 Field-Theoretical Predictions

Chakravarty, Halperin, and Nelson[27] made this argument more precise by employing renormalization group ideas. They performed a block spin renormalization group transformation that mapped the 3-d continuum $O(3)$ model, eq. (2.2), to the 2-d lattice $O(3)$ model, averaging the fields over space-time volumes of size β in the extra dimension and $c\beta$ in the physical dimensions. They thus predicted the leading behavior of the AFHM correlation length,

$$\xi/a = C_\xi \exp(2\pi \rho_s / T)$$

with C_ξ an undetermined constant. Subsequently, Hasenfratz, Maggiore, and Niedermayer[46, 47] calculated the exact mass gap of the $O(3)$ model in eq. (2.3),

$$\xi = \frac{e}{8\Lambda_{\overline{\mathrm{MS}}}}. \tag{2.4}$$

Hasenfratz and Niedermayer[29] utilized this result, as well as the three-loop β-function[48] to get the correlation length of the $O(3)$ model:

$$\xi = \frac{e}{8} \frac{1}{\mu} \frac{g(\mu)}{2\pi} \exp\left(\frac{2\pi}{g(\mu)}\right) \times \left[1 + \frac{g(\mu)}{8\pi} + \mathcal{O}(g^2)\right], \tag{2.5}$$

where $g(\mu)$ is the running coupling for an arbitrary scale μ, for example $\mu = T$. To exploit this result for the AFHM at low temperatures, the challenge is to find a proper way to connect the coupling $g(\mu)$ with the parameters of the AFHM, T and $\rho_s(J)$.

Hasenfratz and Niedermayer[30, 31, 28] computed free energies for the systems in both eq. (2.2) and eq. (2.3) and thus found the connection between the coupling of the $O(3)$ model and the AFHM parameters to be[29]

$$\frac{1}{g(p)}\bigg|_{p=T/c} = \frac{\rho_s}{T} + \alpha + \beta \frac{T}{\rho_s}, \quad \alpha = 0, \beta = \frac{-3/4}{(2\pi)^2}, \tag{2.6}$$

where $g(\mu = p)$ is the renormalized coupling constant of the $O(3)$ model at momentum

$p = T/c$, and c is the spin-wave velocity which takes the role of the speed of light (which was set to unity in eq. (2.5)). Plugging this result into eq. (2.5), Hasenfratz and Niedermayer arrived at what we call the CH_2N_2 formula for the asymptotic, low-temperature behavior of the correlation length:

$$\xi_{AS} = \frac{e}{8} \frac{c}{2\pi\rho_s} \exp\left(\frac{2\pi\rho_s}{T}\right) \left[1 - \frac{T}{4\pi\rho_s} + \mathcal{O}\left(T^2\right)\right].\qquad(2.7)$$

The prefactor $e/8$ comes from the exact mass gap[46, 47] of the $O(3)$ model, eq. (2.4), while the $\mathcal{O}(T)$ correction requires the 3-loop β-function and the calculation in chiral perturbation theory to get the mapping eq. (2.6). When ξ_{AS} becomes valid for the AFHM, $\xi(T)$ "scales asymptotically" with the 3-loop β-function of the $O(3)$ model.

Chiral perturbation theory is just one of the possible techniques to obtain the mapping in eq. (2.6). Other possibilities would be to use simulation in both models, or to work directly with the Hamilton operator eq. (2.1) using spin-wave expansion, for example. Chiral perturbation theory also assumes that the higher derivative terms in the effective action, eq. (2.2), give controllable, small corrections. These higher order contributions enter eq. (2.7) on the four-loop level first[29, 30, 31] (included in $\mathcal{O}(T^2)$), and depend on additional, unknown low-energy constants.

Furthermore, note that the dimensionless parameter of the expansion in eq. (2.7) is $t \equiv T/2\pi\rho_s$, and it is required that the energy scale set by T is much smaller than the leading non-magnon scale ρ_s, that is, $T \ll 2\pi\rho_s$ ($t \ll 1$). If, in a comparison of CH_2N_2 with data for $\xi(T)$ in the AFHM, the higher-derivative contributions in fact turn out to be small compared to the leading $\mathcal{O}(T)$ correction, then it is reasonable to include them in a naive quadratic term αt^2, with α being a free fit parameter. Beard and Wiese took this approach[6] in their $S = 1/2$ QMC study, obtaining $\alpha = -0.75(5)$.

Finally, note that cutoff effects in the $O(3)$ model are $\sim \xi^{-2}$, and are always

neglected since we only consider $\xi \gg a$. The three conditions

$$\left.\begin{array}{rcl} t & \ll & 1, \\ \xi & \gg & a, \text{ and} \\ \xi & \gg & c/T \end{array}\right\} \tag{2.8}$$

are necessary prerequisites on the way to CH_2N_2.

The parameters ρ_s and c first appearing in eq. (2.2) are not fixed by CPT. They can be estimated, for instance, by fitting to QMC data[49, 41, 6, 50]. That, in fact, is the approach we took here. Alternatively, one could use spin-wave theory[51, 52, 53]. Spin-wave expansion (SWE) is an expansion in $1/S$ of interacting spin waves representing the Goldstone bosons of the broken symmetry. The lowest order reproduces a system of classical spins, and subsequent terms introduce the quantum corrections. The SWE predictions are[54, 53]:

$$\left.\begin{array}{rcl} \rho_s & = & S^2 - 0.1176282544S - 0.0102079873 - 0.00316(2)/S, \\ c & = & 2\sqrt{2}S\left(1 + 0.157347421/(2S) + 0.02152(2)/(2S)^2\right) \end{array}\right\} \tag{2.9}$$

2.3 Cutoff Correction

As mentioned previously, various approaches[34, 35, 36, 26, 37, 7] to the $S > 1/2$ AFHM at small correlation lengths showed a serious discrepancy with CH_2N_2 by as much as -75% at moderate $\xi/a \leq 200$. Our results confirm that a serious deviation persists at extremely large, macroscopic correlation lengths $\xi/a \gg 10^5$. At spin $S = 1$, for example, this means that one is forced to postulate in eq. (2.7) an $\mathcal{O}(T^2)$ correction that remains larger than the $\mathcal{O}(T)$ correction until $\xi/a \sim 10^6$, and which becomes less than one-half or one-tenth of the latter only at $\xi/a \sim 10^{12}$ or $\xi/a \sim 10^{61}$, respectively. For example, with[34] $a \approx 4$ Ångstroems for La_2NiO_4, these three ξ values correspond to 0.4 mm, 400 m, and 10^{35} light years, respectively. Things become worse for $S > 1$.

This situation is highly unsatisfactory on theoretical grounds since the mapping of the AFHM onto the $d = 2$ $O(3)$ model is valid much earlier due to $\xi(T) \gg c/T$. In a recent publication, Hasenfratz[38] argued that the serious discrepancy is due to cutoff

effects in the AFHM (not the $O(3)$ model). They arise from the fact that the typical non-Goldstone boson scales like $\xi_\rho \equiv c/\rho_s \sim 1/S$ never become much larger than the lattice spacing a even for small spins, as opposed to a critical system where ξ_ρ goes to infinity. Using the predictions of spin-wave expansion[51, 52, 53], we have $\xi_\rho \approx 10a$ for $S = 1/2$, $\xi_\rho \approx 2a$ for $S = 1$, and $\xi_\rho \approx a$ for $S = 5/2$. Cutoff effects enter the effective CPT description on the 4-loop level first[30, 31] and contribute to the $\mathcal{O}(T^2)$ correction in (2.7). Therefore, CH_2N_2 becomes correct for any S at sufficiently low temperatures (the "renormalized-classical scaling" regime[22, 23, 24, 25]) where the leading effective theory in eq. (2.2) correctly describes the magnon physics. However, for $S > 1/2$ this happens only at astronomically large correlation lengths.

The serious discrepancy at "reasonable" $\xi \gg c/T$ correlation lengths indicates a shortcoming in the technique to connect the coupling of the $O(3)$ model with the AFHM parameters $\rho_s(J)$ and T using CPT for large spin. When large, the AFHM cutoff effects can no longer be described with the effective approach of CPT: the systematic derivative expansion breaks down.

Hasenfratz[38] used bilinear spin-wave expansion (SWE) to calculate the cutoff effects. Since CPT is an exact low-energy expansion, if one replaces in any quantity calculated by CPT the parameters ρ_s and c by their SWE expansion, then the SWE expansion of this quantity is obtained. In particular, eq. (2.6) is an expansion of $1/g(p)$ in powers of $1/S$ since $\rho_s \sim S^2$, $c \sim S$, and $T/J = \mathcal{O}(S)$. This enabled Hasenfratz to incorporate the cutoff effects properly into the CPT mapping eq. (2.6). His result[38] is that the cutoff effects lead to an exponential correction factor: $\xi_{\text{ASC}} = \xi_{\text{AS}} \exp(-C(\gamma))$, where the parameter $\gamma \equiv 2JS/T$ brings in the explicit spin dependence.

In our analysis, we account for a minor refinement of the result by Hasenfratz: we explicitly keep the quadratic term in eq. (2.7). It seems unreasonable to keep this term since there are unknown corrections of the same $\mathcal{O}(T^2)$ order. However, it turns out from our data that this term is in fact a small but significant improvement at intermediate correlation lengths for all spins, implying that the remaining, unknown $\mathcal{O}(T^2)$ correction is small in comparison. Note that this coefficient comes from the

CPT mapping in eq. (2.6) alone, and has nothing to do with the cutoff effects in the AFHM.

In conclusion, we retain the quadratic term $(27/32)t^2$ in eq. (2.7) to quote the result by Hasenfratz, although this term is only a part of the $\mathcal{O}(T^2)$ correction. The resulting CH_3N_2B formula is

$$
\begin{aligned}
\xi_{\text{ASC}} &= \frac{e}{8} \frac{c}{2\pi\rho_s} \exp\left(\frac{1}{t}\right) \exp\left(-C(\gamma)\right) \\
&\quad \times \left[1 - \frac{1}{2}t + \frac{27}{32}t^2 + \mathcal{O}\left(T^2\right)\right] \\
\gamma &= 2JS/T
\end{aligned}
\tag{2.10}
$$

In Ref. [38], $C(\gamma)$ is expressed as an integral of familiar spin-wave quantities over the first Brillouin zone. Again, we note that $C(\gamma \to \infty) \sim \gamma^{-2}$, thus CH_2N_2, eq. (2.7), is recovered for $T \to 0$, and at low temperatures $\exp(-C(\gamma))$ merges into the $\mathcal{O}(T^2)$ correction.

Chapter 3

Monte Carlo Simulation

Strongly-coupled systems such as the AFHM are generally not amenable to either exact analytic or perturbative calculations, although in a few instances some exact results have been produced— for example, the Bethe ansatz solution for the one-dimensional Heisenberg model and the existence of symmetry breaking in the higher-spin 2-d AFHM.

In general, though, predictions as to the behavior of strongly-interacting systems must rely on numerical simulation techniques. The field of Monte Carlo simulation is a rich and varied one, allowing one to perform numerical "experiments" where exact results are unavailable. In this chapter, I will discuss the main principles of numerical simulations as they pertain to the AFHM. Indeed, the general principles, though not the specific implementation details, will be the same as for the classical spin systems discussed in the second half of this thesis.

3.1   Formulation for a Quantum System

In performing numerical simulations for a quantum-mechanical system described by the Hamiltonian $\mathbb{H}$, one is interested in the thermodynamic properties of the system at a given temperature $T \equiv 1/\beta$. These properties are determined by the partition function $Z = \mathbf{Tr}\left[e^{-\beta \mathbb{H}}\right]$ and the ensemble average of an observable $\mathbb{O}$,

$$\langle \mathbb{O} \rangle = \frac{1}{Z} \mathbf{Tr} \left[\mathbb{O} e^{-\beta \mathbb{H}} \right]. \tag{3.1}$$

In a basis $\{|\psi_i\rangle\}$ of energy eigenstates, the numerator in eq. (3.1) simplifies to

$$\sum_i O_{ii} e^{-\beta E_i},$$

with a similar expression for Z, where $O_{ii} \equiv \langle \psi_i |\mathbb{O}| \psi_i \rangle$. The number of states that must be enumerated in order to explicitly compute the trace is exponential in the size of the system, which is clearly impractical. Importance sampling, as described below, turns out to be a clever method to obtain an excellent approximation to eq. (3.1). First, though, the system must be reformulated in a manner more amenable to computer simulation.

The exponential in the expression for the partition function Z is analogous to the quantum time evolution operator $e^{-i\mathbb{H}t}$ in Euclidean time. Motivated by this analogy, one can break up the Euclidean time extent β into N_t time slices of "duration" $\beta\epsilon$, such that $N_t\epsilon = 1$ as the limit of infinitesimal time slices is approached $\epsilon \to 0$. The numerator in eq. (3.1) then takes the form

$$R[\mathbb{O}] = \lim_{N_t \to \infty} \mathbf{Tr} \left[\mathbb{O} e^{-\beta\epsilon\mathbb{H}} \right]_t^N = \lim_{N_t \to \infty} \int [D\psi] \langle \psi_1 |\mathbb{O}| \psi_{N_t} \rangle \prod_{t=1}^{N_t} \langle \psi_{t+\epsilon} \left| e^{-\beta\epsilon\mathbb{H}} \right| \psi_t \rangle, \tag{3.2}$$

where a complete set of states $|\psi_t\rangle$ has been inserted at each time slice t, and the path integral notation, as usual, means a summation over all possible values of the $\{|\psi_t\rangle\}_{t=1}^{N_t}$. This summation reduces the problem to a classical one, since carrying out the trace now means calculating the product in eq. (3.2) at every point in the "configuration space" $\{|\psi_t\rangle\}_{t=1}^{N}$. Note that the cyclicity of the trace implies periodic boundary conditions in the Euclidean time direction.

If the Hamiltonian is a sum of non-commuting terms, as eq. (2.1) is, there is an ambiguity in the evaluation of the individual transfer matrices $\langle \psi_{t+\epsilon} \left| e^{-\epsilon\mathbb{H}} \right| \psi_t \rangle$. This ambiguity is resolved by the "Trotter decomposition,"[55, 56] which involves writing the original Hamiltonian $\mathbb{H}$ as a sum of "sub-Hamiltonians" $\mathbb{H}_i$, each of which is
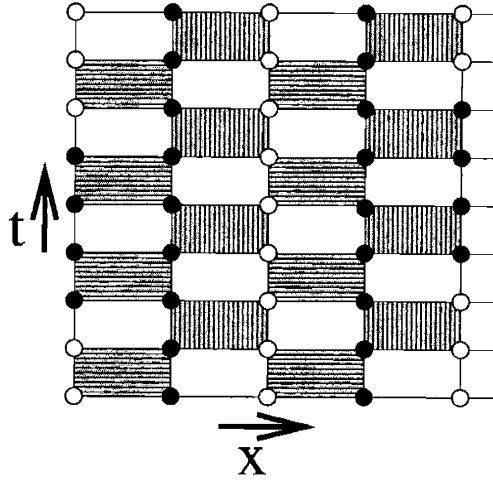
Figure 3-1: A typical configuration of the lattice after the Trokki-Suzuki decomposition. This example is an antiferromagnet in one spatial dimension x; t denotes Euclidean time. The Hamiltonian can be written as a sum of two interacting terms, which, upon Trotterization, induce interactions on the shaded plaquettes. The situation for the two-dimensional systems discussed in the text are entirely analogous, but harder to visualize.

comprised of mutually commuting terms. In the case of the 2-d AFHM, the sum takes the form

$$\mathbb{H} = \mathbb{H}_{\text{even},\hat{1}} + \mathbb{H}_{\text{even},\hat{2}} + \mathbb{H}_{\text{odd},\hat{1}} + \mathbb{H}_{\text{odd},\hat{2}}.$$

Here, "even" and "odd" refer to the staggered sites on the 3-d lattice (N_t copies of the original 2-d lattice), and $\hat{1}$ and $\hat{2}$ denote that the corresponding Hamiltonian contains the interactions in the corresponding (positive) coordinate direction.

It is conventional to visualize the action of each sub-Hamiltonian as a rectangular "plaquette," where one of the sides represents the two interacting spins at equal time $S_{x,t}$ and $S_{y,t}$ and the opposite side represents the same two spins at the next time slice, $S_{x,t+\epsilon}$ and $S_{y,t+\epsilon}$. This is illustrated in Fig. 3-1, where the checkerboard shading pattern denotes that each of the sub-Hamiltonians acts in adjacent time slices.

The ensemble average in eq. (3.2) then takes the form

$$R[\mathbb{O}] \quad = \quad \lim_{N_t \to \infty} \int [D\psi]\, \mathbb{O} \prod_{t=1}^{N_t} \left\langle \psi_{t+\epsilon} \left| e^{-\beta\epsilon \sum_{\mu=\hat{1},\hat{2}} \sum_{x=\text{even,odd}} \mathbb{H}_{x,\mu}} \right| \psi_t \right\rangle$$

$$\approx \int [D\psi] \mathbb{O} \prod_{t=1}^{N_t} \prod_{x=\text{even,odd}} \prod_{\mu=\hat{1},\hat{2}} \left\langle \psi_{t+\epsilon} \left| e^{-\beta\epsilon\mathbb{H}_{x,\mu}} \right| \psi_t \right\rangle. \tag{3.3}$$

This expression contains errors of order ϵ^2 which vanish as $N_t \to \infty$. The form of eq. (3.3) is the product of transition matrices

$$\mathbb{T}_{x,\mu,t} = \left\langle \psi_{t+\epsilon} \left| e^{-\beta\epsilon H_{x,\mu}} \right| \psi_t \right\rangle \tag{3.4}$$

which govern the local interaction between a pair of (space-like) neighboring spins as they propagate from time slice t to $t + \epsilon$. The path integral still signifies that we are to sum over all possible values of the $L^d N$ spins in the $(d + 1)$- dimensional system.

For the AFHM Hamiltonian, equation (2.1) yields the transfer matrix for each plaquette of spins interacting between time slices t and $t + 1$:

$$
\begin{aligned}
\mathbb{T}_{x,\mu,t} &= \left\langle \psi_{t+\epsilon} \left| e^{-\beta\epsilon H_{x,\mu}} \right| \psi_t \right\rangle \\
&= \exp\left(-\frac{1}{4}\epsilon\beta\right)
\begin{bmatrix}
1 & 0 & 0 & 0 \\
0 & \frac{1}{2}\left(1 + e^{\epsilon\beta J}\right) & \frac{1}{2}\left(1 - e^{\epsilon\beta J}\right) & 0 \\
0 & \frac{1}{2}\left(1 - e^{\epsilon\beta J}\right) & \frac{1}{2}\left(1 + e^{\epsilon\beta J}\right) & 0 \\
0 & 0 & 0 & 1
\end{bmatrix},
\end{aligned}
\tag{3.5}
$$

where, in the last step, the basis $\{|++\rangle, |+-\rangle, |-+\rangle, |--\rangle\}$ was chosen. In order to interpret the matrix elements as Boltzmann weights, a further change of basis is necessary to make the quantities appearing in eq. (3.5) positive. This can be accomplished by rotating every other spin in the lattice by π around the z axis. This then leads to the modified transfer matrix

$$
\mathbb{T}_{x,\mu,t} = \exp\left(-\frac{1}{4}\epsilon\beta\right)
\begin{bmatrix}
1 & 0 & 0 & 0 \\
0 & \frac{1}{2}\left(e^{\epsilon\beta J} + 1\right) & \frac{1}{2}\left(e^{\epsilon\beta J} - 1\right) & 0 \\
0 & \frac{1}{2}\left(e^{\epsilon\beta J} - 1\right) & \frac{1}{2}\left(e^{\epsilon\beta J} + 1\right) & 0 \\
0 & 0 & 0 & 1
\end{bmatrix}.
\tag{3.6}
$$

30

3.2 Importance Sampling

The thermodynamic averages thus reduce to sums over the configuration space formed by all possible combinations of up and down spins in each time slice of the $(d + 1)$-dimensional lattice. These sums are exponentially large in the spatial volume of the system (since each combination of plaquette eigenstates is itself an eigenstate of $\mathbb{H}_{x,\mu}$, barring non-allowed configurations) as well as in the number N_t of time slices. Importance sampling tackles the exponentially large number of states due to the spatial size of the system; the continuous-time technique, described in Section 3.5, eliminates the growth in the number of states due to $\epsilon \to 0$.

Importance sampling is based on the observation that, for quite general systems, only a fraction of the permissible configurations $[\phi]$ carry any substantial Boltzmann weight; the contributions from other regions in configuration space are negligible. To obtain good approximations to thermodynamic quantities, it suffices to sample only these important configurations. Since it is not clear how to determine *a priori* which states are relevant and whether their number is indeed manageable, importance sampling generates configurations stochastically. It does not guarantee that for any finite simulation all possible configurations are generated, but it does generate thermodynamic averages that, in general, approach true values as the length of the simulation increases.

Importance sampling relies on two principles:

- **Ergodicity:** Given one permissible configuration $[\phi]$ of the system (that is, one with non-zero Boltzmann weight $W[\phi]$), it must be possible to reach any other permissible configuration $[\phi']$ in a finite number of steps. This assures that the simulation *can* sample the whole configuration space.

- **Detailed balance:** The probability of going back and forth between configurations $[\phi]$ and $[\phi']$ must be proportional to the ratio of their Boltzmann weights:

$$\frac{p\left([\phi] \to [\phi']\right)}{p\left([\phi'] \to [\phi]\right)} = \frac{W[\phi']}{W[\phi]}. \tag{3.7}$$

31

This assures that each configuration generated, in the limit of a large run, appears with a frequency proportional to its Boltzmann weight.

Monte Carlo simulations thus become a guided random walk which generate a Markov chain of configurations, sampling the integrand of the partition function preferentially in the region where it is most sharply peaked. Where various Monte Carlo schemes differ is in the manner in which a new configuration $[\phi']$ is generated. Much effort has been expended in finding the right algorithm for a given problem in order to make the simulations efficient.

3.3   Metropolis Algorithm

The standard way to implement Monte Carlo simulations is by using variations of the algorithm first developed by Metropolis[57, 58]. Although these algorithms are often inefficient, they provide a simple standard by which to judge cleverer schemes such as the ones used here. Metropolis-type algorithms proceed by proposing (usually at random) a local change in the configuration space $[\tilde{\phi}]$, and using a probabilistic rule to accept or reject the suggestion depending on detailed balance. The probability that the new configuration $[\phi']$ is $[\tilde{\phi}]$ rather than $[\phi]$ is then given by

$$
\begin{aligned}
p\left([\phi]\to[\phi']\right) &= \begin{cases} 1 & \text{if } W[\phi'] > W[\phi] \\ W[\phi']/W[\phi] & \text{otherwise} \end{cases} \\
&= \min\left(1, \frac{W[\phi']}{W[\phi]}\right).
\end{aligned} \tag{3.8}
$$

This rule obviously satisfies detailed balance, eq. (3.7), but it may be quite inefficient. In particular, in the neighborhood of critical phenomena, where vast expanses of the system are correlated, small local changes may be rejected an overwhelming fraction of the time, a phenomenon known as "critical slowing down." Nevertheless, this is a simple algorithm to implement when more clever schemes are not apparent. Furthermore, it can be combined with other more efficient algorithms to help provide

for ergodicity. This is in fact done in the simulations of $SO(M) \otimes SO(N)$ models discussed in the second part of this thesis.

3.4   The Quantum Cluster Algorithm

Cluster algorithms address critical slowing down by proposing large-scale changes that are automatically accepted. Suppose one has a Hamiltonian (classical or quantum) comprised of local interactions between sites on a lattice. One begins at a random site, and applies *cluster rules* to group it with a neighboring site, using detailed balance. One continues applying the cluster rule at each new site until the cluster closes. The cluster can then be "flipped" at random (but without further regard to detailed balance) to generate a new configuration.

There are two main variants of these algorithms. The multi-cluster version fills the lattice with clusters, so that each site is in exactly one cluster. The clusters are then flipped randomly to generate a new configuration. The single-cluster version creates only one cluster and flips it with probability one. The latter is the version that has been used for all the simulations in this thesis.

The first step in crafting the cluster algorithm is to choose the breakups, that is, how to group lattice spins so that they may be updated simultaneously. It suffices to consider breakups locally: if these satisfy detailed balance, so will the breakups of the whole lattice. There are six non-zero elements in the transfer matrix, eq. (3.6), hence six legal plaquette configurations. Because of up/down symmetry, however, it suffices to consider just three plaquette patterns; the other three can be obtained by switching up and down spins.

The three Boltzmann weights are shown in Table 3.1, together with the breakup patterns that satisfy detailed balance. The rules may be summarized as follows: a spin may be joined with its time-like replica only if they both have the same spin, and with its space-like neighbor only if they have opposite spins. In the one situation where both of these possibilities are allowed, a probability of joining the time-like rather than the space-like spins is $p = \frac{2}{1+\exp(\epsilon\beta J)}$.
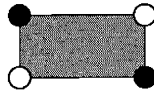
weight	configuration	break-ups
$e^{-\frac{1}{4}\epsilon\beta J}$		1
$\frac{1}{2}e^{-\frac{1}{4}\epsilon\beta J}\left(e^{\epsilon\beta J}-1\right)$		1
$\frac{1}{2}e^{-\frac{1}{4}\epsilon\beta J}\left(e^{\epsilon\beta J}+1\right)$		p $\quad$ $1-p$

Table 3.1: The non-trivial plaquette weights and breakups for the AFHM in discrete time. Time (space) is in the vertical (horizontal) direction. Black (white) circles denote spin up (down). The indicated breakups, where $p = \frac{2}{1+\exp(\epsilon\beta J)}$, satisfy detailed balance, eq. (3.7), and admit a continuous-time limit, as explained in Sec. 3.5.

These cluster rules lead to two corollaries. A time-like cluster segment always includes spins that are of the same orientation (up or down), and the orientation changes exactly when the the cluster jumps to a neighboring site. Thus, if sites x and y are in the cluster, they must satisfy

$$(-1)^{|x-y|}S_x^z \cdot S_y^z = 1, \tag{3.9}$$

where $(-1)^{|x-y|}$ is the "stagger factor" that counts how many spatial links separate x and y. As a result of these rules and the geometry of the Trotter-Suzuki decomposition, the cluster grows in opposite time directions every time it jumps to a neighboring site; this is illustrated in Fig. 3-2.

Figure 3-2: A typical cluster flip in the discrete-time algorithm, starting from the configuration in Fig. 3-1. The dark (light) circles are spin up (down). The thick gray line denotes a cluster which is then flipped. Note that adjacent spins in the cluster are oppositely oriented exactly when they're spatial neighbors, and that the cluster reverses time direction at each of those jumps.
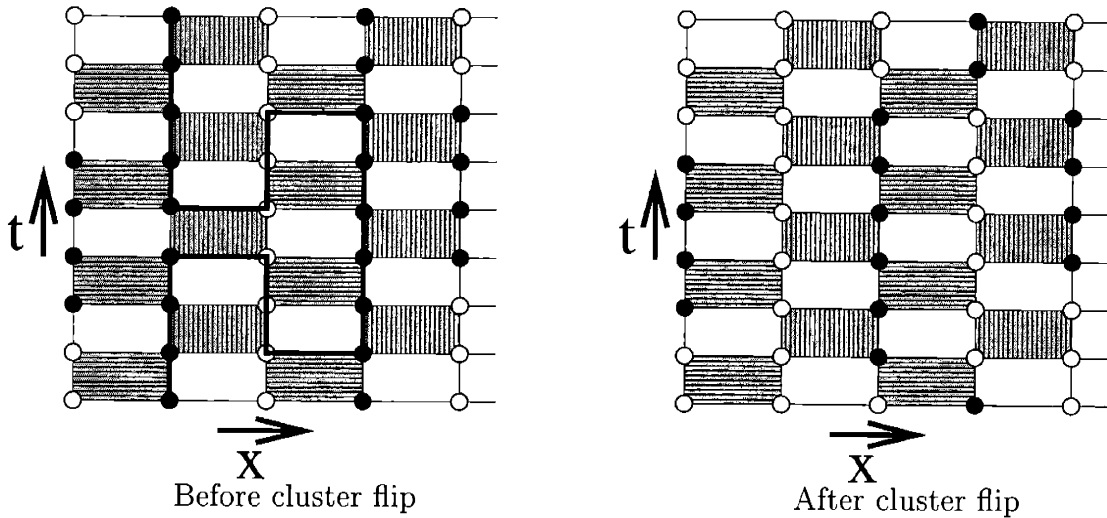
3.5 Generalization to Continuous Time

Beard and Wiese[6] noted that these cluster rules can be generalized to the time continuum limit. The crucial observation is that the probability for continuation in time (*i.e.*, following a time line of constant spin) is of order 1, whereas the probability to jump ("decay") to an available (*i.e.* oppositely-oriented) neighboring spin is of order ϵ. Considering the limit of a large number $N_t \rightarrow \infty$ of time slices, the decay probability per unit time becomes $\lambda = \lim_{\epsilon \rightarrow 0}(1 - P)/\epsilon\beta = J/2$. Whereas the discrete-time algorithm alternates plaquettes that connect a given spin with each of its neighbors, as $\epsilon \rightarrow 0$ each spin can interact with its neighbors simultaneously. Thus, at any given instant in Euclidean time, there is a decay probability λ for a cluster to jump from its current spin to *each* of the available neighboring spins; this is the continuum version of the probabilistic choice depicted in the third row of Table 3.1. The total probability per unit time that the cluster will jump sites is proportional to the number of available neighboring spins at any given instant. By construction, the cluster rules are memory-less (i.e., the probability of a decay in a given "optional"

plaquette is independent of what the cluster did before). In this continuous-time version, then, the decays from a given spin during a finite period of time are given by a Poisson distribution, and the length of time from any arbitrary instant to the next decay at that spin is given by the first order interarrival time probability density function for the Poisson distribution— the exponential function with decay constant $\lambda = \beta J/2$ per available neighboring spin. Figure 3-3 shows an example of a cluster flip in continuous time.
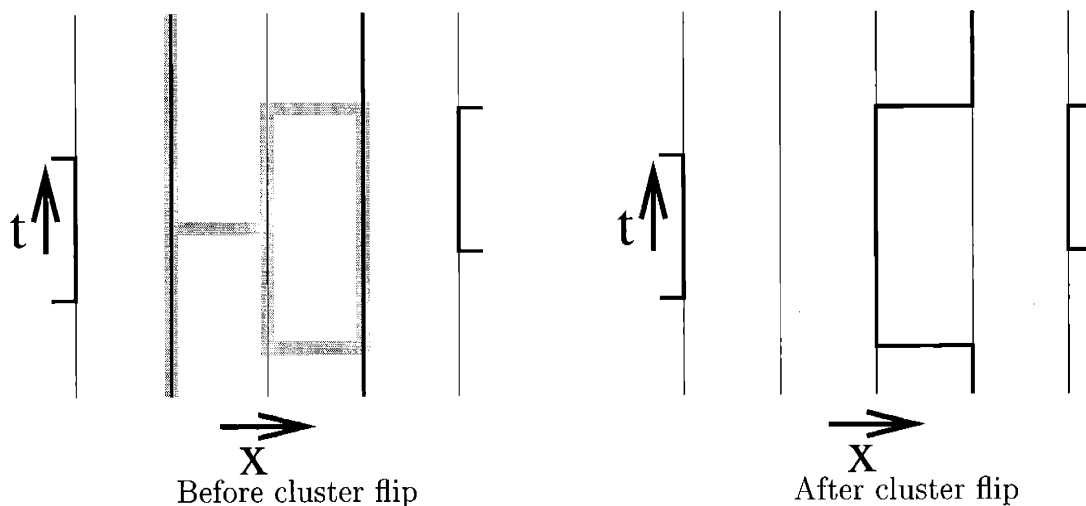
Figure 3-3: A typical cluster flip in the continuous-time algorithm. The dark (light) lines are spin up (down). The thick gray line denotes a cluster which is then flipped. This is the continuous-time version of the example in Fig. 3-2.

There are two main advantages to the continuous-time formulation of the AFHM simulations. The first is that there is no need to repeat the simulations at larger and larger Trotter number in order to approach the time continuum limit. One works directly in the continuum instead. The second advantage is that it is much more efficient (if complicated) to store the continuous-time simulation on the computer than the discrete-time. For the discrete-time formulation, one needs to keep track of the state of the system at VN_t sites, as $N_t \rightarrow \infty$. In the continuous-time formulation, one only needs to store the V initial spin states, and the transition times at each site. This is a monumental savings in memory requirements— one does not store

redundant information about spin states that are constant in time.

3.6   Higher Spin Code

The above algorithms, both for discrete and continuous time, may be generalized to higher-spin representations S. *A priori*, it is not obvious how to do this: after all, what does it mean to "flip" a spin whose third component vanishes? The fundamental idea, however, is to couple together $2S$ spin-$\frac{1}{2}$ "subspins" at each lattice site. The resulting reducible representation will include the spin S representation. One then includes a projector to make sure that only this irreducible representation is sampled, rather than any of the others present in the tensor product.

Thus, the spin $\mathbb{S}_x$ at site x becomes the sum of $2S$ spins-$\frac{1}{2}$. In terms of Pauli matrices at each site,

$$
\begin{aligned}
\mathbb{S}_x \cdot \mathbb{S}_y \;=\; & \frac{1}{2}\left(\sigma_{x,1} + \cdots + \sigma_{x,2S}\right) \\
& \cdot \frac{1}{2}\left(\sigma_{y,1} + \cdots + \sigma_{y,2S}\right).
\end{aligned} \tag{3.10}
$$

The spin-S Hamiltonian then has a similar form as before,

$$
\begin{aligned}
\mathbb{H} \;=\;& J \sum_{<xy>} \mathbb{S}_x \cdot \mathbb{S}_y \\
=\;& \frac{J}{4} \sum_{<xy>} \left[\sigma_{x,1} + \ldots + \sigma_{x,2S}\right] \cdot \left[\sigma_{y,1} + \ldots + \sigma_{y,2S}\right] \\
=\;& \frac{J}{4} \big[\quad \sigma_{x,1} \cdot \sigma_{y,1} + \sigma_{x,1} \cdot \sigma_{y,2} + \ldots \\
& \quad + \;\sigma_{x,2} \cdot \sigma_{y,1} + \sigma_{x,2} \cdot \sigma_{y,2} + \ldots \\
& \quad + \;\ldots \qquad\qquad\qquad\qquad\quad \big],
\end{aligned} \tag{3.11}
$$

which is nothing other than a sum of spin-1/2 interactions. Thus, each of the "subspins" or "layers" at each lattice site has the same basic $S = 1/2$ antiferromagnetic interaction with every single subspin at each neighboring site (but not at its own site).

Hence, upon Trotterization, the transfer matrices will have the same form as for the $S = 1/2$ Hamiltonian and one may use the same cluster rules as for spin-1/2. Note that since the subspins still interact between *different* lattice sites, the arguments based on the stagger factor on the lattice are still valid: we can still rotate every other site by π around the z axis to obtain a non-negative transfer matrix among the subspins, and eq. (3.9) still holds for any pair of spins in the cluster. In essence, the only difference caused by the introduction of the subspins is to make the topology of the cluster more complicated, while the microscopic rules remain the same.

Since the spin-S Hamiltonian commutes with the spin-S projection operators $\mathbb{P}_S(x)$ at each site x, one can insert a lattice projector $\mathbb{P}_S = \prod_x \mathbb{P}_S(x)$ at some fixed time slice in the path integral to ensure that the coupling among the spin-$\frac{1}{2}$ objects does not take the system out of the spin-S sector. The complete partition function can then be written as $Z = \mathbf{Tr}[e^{-\beta \mathbb{H}} \mathbb{P}_S]$.

The projection operator $\mathbb{P}_x$ at a single site x is a $2^{2S} \times 2^{2S}$ matrix. The transfer matrix elements depend on the states of the $4S$ spins 1/2 involved:

$$\langle S_i(t = 0^-)|\mathbb{P}|S_i(t = 0^+)\rangle = \prod_x \mathbb{P}_x[\sigma_1(x, 0^-), \ldots, \sigma_{2S}(x, 0^-), \sigma_1(x, 0^+), \ldots, \sigma_{2S}(x, 0^+)]..$$

$$(3.12)$$

It turns out that the elements of the projection operator only depend on the total spin S and the projection of spin onto the 3-axis, *i.e.* on $M \equiv \sum_i m_i$. In terms of the $l = 2S$ subspins, the state with highest projection can be written

$$\left| S = \frac{l}{2}, M = \frac{l}{2} \right\rangle = |+_1 \cdots +_{2S}\rangle$$

Using the lowering operator repeatedly, we obtain, on the left,

$$(\mathbb{S}^-)^k \left| S = \frac{l}{2}, M = \frac{l}{2} \right\rangle = \sqrt{\frac{l! k!}{(l - k)!}} \left| S = \frac{l}{2}, M = \frac{l}{2} - k \right\rangle$$

and on the right,

$$\left(\mathbb{S}^-\right)^k |+_1 \cdots +_{2S}\rangle = \sum_{\mathcal{P}} k! |\mathcal{P} \{-_1 \cdots -_k +_{k+1} \cdots +_{2S}\}\rangle$$

where the sum is over every permutation $\mathcal{P}$ of kets with exactly k down spins. The $k!$ prefactor comes from all the possible sequences in which any particular set of k spins can be lowered. It then follows that

$$\left| S = \frac{l}{2}, M = \frac{l}{2} - k \right\rangle = \left[\frac{(l-k)!k!}{l!} \right]^{\frac{1}{2}} \sum_{\mathcal{P}} |\mathcal{P} \{-_1 \cdots -_k +_{k+1} \cdots +_{2S}\}\rangle$$

whence the projector is given by

$$\langle \mathcal{P}_{t=0^-} \{-_1 \cdots -_k +_{k+1} \cdots +_{2S}\} | \mathbb{P}_S | \mathcal{P}_{t=0^+} \{-_1 \cdots -_k +_{k+1} \cdots +_{2S}\}\rangle =$$

$$\langle \mathcal{P}_{t=0^-} \{-_1 \cdots -_k +_{k+1} \cdots +_{2S}\} | S = l/2, M = l/2 - k \rangle \cdot$$

$$\langle S = l/2, M = l/2 - k | \mathcal{P}_{t=0^+} \{-_1 \cdots -_k +_{k+1} \cdots +_{2S}\}\rangle =$$

$$\frac{(l-k)!k!}{l!},$$

that is,

$$\langle M' | \mathbb{P}_x | M \rangle = \frac{\delta_{MM'}}{\binom{2S}{S-M}}. \tag{3.13}$$

The projection-operator plaquettes in discrete time couple $2S$ subspins at time $t = 0^-$ at site x with $2S$ subspins at time $t = 0^+$ at the same site x. Because of the presence of $\delta_{MM'}$ in the projection operator, non-zero-weight configurations must have the same number of "up" subspins at $t = 0^-$ and $t = 0^+$. Let N_U ($= 2S - k$) be the number of "up" subspins at either time, and N_D ($= k$) be the number of "down" subspins. Since $N_U + N_D = 2S$ and $(N_U - N_D)/2 = M$, we have $N_U = S + M$ and $N_D = S - M$.

A simple flow rule that satisfies detailed balance is this: if the flow enters at an "up" subspin at $t = 0^-$, then it must exit at one of the N_U "up" subspins at $t = 0^+$, selected randomly with equal probabilities $1/N_U$. Similarly, if the flow enters at a
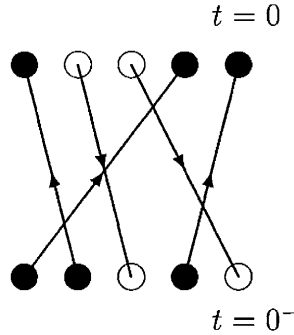
Figure 3-4: A typical mapping for a projection operator plaquette for an $S = 5/2$ system. Here three up subspins are depicted with solid circles, and two down subspins by open circles. Flow rules combine like subspins with equal weight ($1/N_U$ for up and $1/N_D$ for down). This particular wiring has the same probability as each of the $3!2! = 12$ similar wirings.

"down" subspin at $t = 0$, then it must exit at one of the N_D "down" subspins at $t = 0^-$, selected randomly with equal probability $1/N_D$. By pairing "up" subspins with "up" subspins and "down" with "down", flipping a cluster always results in another legal plaquette configuration. If a cluster visits the same projector plaquette multiple times, say by returning to a second "up" site at $t = 0^-$, then we demand the path be self-avoiding and the random pick must be among the remaining $N_U - 1$ "up" subspins at $t = 0$. Note that we are thus able to preserve compatibility with the rule that the cluster grows in opposite time directions at "up" and "down" sites. To save a small amount of computational overhead, we can choose the "wiring" of the plaquette all at once on the first visit by selecting at random from among the $N_U!N_D!$ different ways of mapping "up" to "up" and "down" to "down". Fig. 3-4 shows such a wiring choice for an $S = 5/2$ projector with $N_U = 3$ and $N_D = 2$.

To demonstrate detailed balance for these flow rules, we need to establish

$$W([\phi])p([\phi] \rightarrow [\phi']) = W([\phi'])p([\phi'] \rightarrow [\phi]), \qquad (3.14)$$

where the $[\phi]$ are the various cases of $4S$-spin arrangements. Consider some arrangement A with N_U "up" subspins. According to eq. (3.13), this arrangement has Boltzmann weight

$$W(A) = \frac{1}{\binom{2S}{S-M}} = \frac{1}{\binom{2S}{N_D}} = \frac{N_U! N_D!}{(2S)!},$$

(where the last equality trivially follows from $N_U + N_D = 2S$). Assume the cluster enters at $t = 0^-$ on an "up" subspin. The probability of selecting a particular "up" spin at $t = 0^+$ is $p(A \to B) = 1/N_U$. Flipping this loop will result in a particular configuration B with one fewer "up" spin and one more "down" spin,

$$N_U' = N_U - 1, N_D{}' = N_D + 1. \tag{3.15}$$

This configuration will have weight

$$W(B) = \frac{N_U{}'! N_D{}'!}{(2S)!}$$

The probability for the reverse transformation, given that the flow enters at the appropriate "down" subspin at $t = 0$, is $p(B \to A) = 1/N_D{}'$. Hence we need merely verify

$$\left(\frac{N_U! N_D!}{(2S)!} \right) \left(\frac{1}{N_U} \right) = \left(\frac{N_U{}'! N_D{}'!}{(2S)!} \right) \left(\frac{1}{N_D{}'} \right)$$

Cancellations give

$$(N_U - 1)! N_D! = N_U{}'! (N_D{}' - 1)!$$

But this is automatically true by virtue of the equalities in eq. (3.15). By this and identical arguments for other cases we thus show that these rules satisfy detailed balance.

In summary, then, the cluster rules for the higher spin AFHM are the same as for the spin-$\frac{1}{2}$ model, with two modifications:

- **The topology** is more complicated, since all the spin-1/2 objects at one site interact with all of their counterparts at neighboring sites.

- **The projector** inserts an additional interaction, which for convenience we implement at time $t = 0^-$.

The continuous time generalization of the spin-1/2 rules still applies, and the projector, which in the discrete-time case acts only during one time slice, now induces an "instantaneous" interaction at an arbitrary point in the time continuum (which we choose to be $t = 0^-$).

3.7 Improved Estimators

Cluster algorithms often permit the use of *improved estimators*, expressions that can yield thermodynamic averages with a smaller variance than naive measurements would suggest. An improved estimator $\mathcal{O}_{\mathrm{impr}}$ is a weighed average of an observable $\mathcal{O}$ over all the configurations $[\phi']$ reachable from the current configuration $[\phi]$ by means of cluster flips:

$$\mathcal{O}_{\mathrm{impr}} = \sum_{[\phi']} p\left([\phi] \rightarrow [\phi']\right) \mathcal{O}[\phi']. \tag{3.16}$$

In the case of a multi-cluster algorithm, where each of the n_c clusters is flipped with probability 1/2, this simplifies to

$$\mathcal{O}_{\mathrm{impr}} = 2^{-n_c} \sum_{[\phi']} \mathcal{O}[\phi']. \tag{3.17}$$

As an example of improved estimators[59], consider the staggered spin correlation function $(-1)^{|x-y|} \left\langle S_x^z \cdot S_y^z \right\rangle$ between sites x and y on the lattice, from which function one can extract the correlation length ξ used for the data analysis in Chapter 4. If the two spins are in the same cluster, in any of the configurations $[\phi']$, $\left(S_x^z \cdot S_y^z\right)_{\mathrm{impr}} = S_x^z \cdot S_y^z$. If the two spins are in different clusters, they give a contribution of $-S_x^z \cdot S_y^z$ if exactly one of two clusters is flipped, and $+S_x^z \cdot S_y^z$ otherwise. In a multi-cluster algorithm where each cluster is flipped with probability 1/2, this directly leads to the improved estimator

$$\mathcal{O}_{\text{impr}} = \begin{cases} S_x^z \cdot S_y^z & \text{if } x \text{ and } y \text{ in the same cluster} \\ 0 & \text{otherwise.} \end{cases} \qquad (3.18)$$

[Recall that the cluster rules in Table 3.1 lead to the stagger relation, eq. (3.9)] The advantage of using an improved estimator is then obvious: suppose $\left\langle S_x^z \cdot S_y^z \right\rangle \ll 1$, as in the exponential tail of a correlation function. Then the variance in the naive estimator is $\left\langle (S_x^z \cdot S_y^z)^2 \right\rangle - \left\langle S_x^z \cdot S_y^z \right\rangle^2 = 1 - \left\langle S_x^z \cdot S_y^z \right\rangle^2 \approx 1$, whereas the variance of the improved estimator is

$$\begin{aligned} \left\langle (S_x^z \cdot S_y^z)^2 \right\rangle_{\text{impr}} - \left\langle S_x^z \cdot S_y^z \right\rangle^2_{\text{impr}} &= \left\langle S_x^z \cdot S_y^z \right\rangle_{\text{impr}} - \left\langle S_x^z \cdot S_y^z \right\rangle^2_{\text{impr}} \\ &\approx \left\langle S_x^z \cdot S_y^z \right\rangle_{\text{impr}} \equiv \left\langle S_x^z \cdot S_y^z \right\rangle \ll 1. \qquad (3.19) \end{aligned}$$

Chapter 4

Results: Fits Compared with Experiment and Theory

We have obtained simulation data for the full range of spins $S \leq 5/2$. The $S = 1/2$ data were obtained by Beard and Wiese[6] using the quantum cluster algorithm, while higher spin data were obtained using both the continuous-time, higher spin cluster algorithm ("LATTHS") described in the previous chapter and the "VLC" algorithm, a higher-spin, discrete time loop cluster algorithm based on a method proposed by Kawashima and Gubernatis[60, 61] and implemented by P. Keller-Marxer. Details of the VLC algorithm may be found in [17, 62]. Results from these two independent codes were cross-checked and agree for all spins within statistical errors, giving a high degree of confidence to our calculations.

Figure 4-1 shows the QMC data for the full range of spins $S \leq 5/2$, plotted on a "Memphis chart," with $\xi(t)$ normalized by the leading (2-loop) term $(e/8)(c/2\pi\rho_s)\cdot$ $\exp(1/t)$ and plotted against the dimensionless CPT expansion parameter $t \equiv T/2\pi\rho_s$. The QMC data[63] in the figure cover the ranges $\xi/a \sim 3$ up to a maximum ξ/a of 350,000 for $S = 1/2$; 160,000 for $S = 1$; 600,000 for $S = 3/2$; 190,000 for $S = 2$; and 135,000 for $S = 5/2$. Additional data for extremely large $\xi/a = 10^6 - 10^{30}$ and extremely small $\xi/a = 0.1 - 3$ are discussed in Sec. 4.2.2.

In Figure 4-1, the predictions CH_3N_2B, eq. (2.10), are the solid curves $y = \exp(-C(\gamma))[1 - t/2 + (27/32)t^2]$, plotted for $\xi/a > 3$ which satisfies the validity
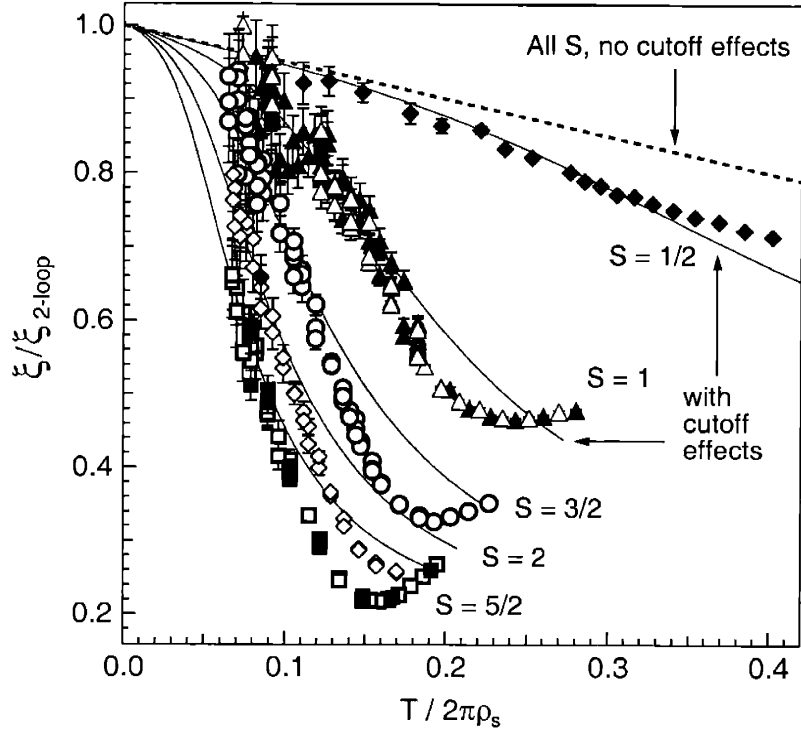
Figure 4-1: Memphis chart for the AFHM. Correlation length QMC data and theoretical predictions are normalized by the leading (2-loop) prediction $(e/8)(c/2\pi\rho_s)\exp(1/t)$. Solid lines are the CH_3N_2B predictions, eq. (2.10). The dashed line is the spin-independent "no cutoff effects" prediction CH_2N_2, eq. (2.7). Filled (open) symbols are from the LATTHS (VLC) algorithm. The QMC data smoothly merge into CH_3N_2B at low temperatures.

criteria, eqs. 2.8. The "no cutoff effects" prediction CH_2N_2, eq. (2.7), is the dashed line $y = 1 - t/2$, and does not depend on spin. The regimes where the QMC data approach the cutoff corrected prediction CH_3N_2B are $\xi/a \approx 10$ for $S = 1/2$, and $\xi/a = \mathcal{O}(100)$ for all $S > 1/2$.

Asymptotic scaling (with the 3-loop β-function of the 2-d $O(3)$ model) sets in when the next-to-leading $\mathcal{O}(T^2)$ correction in eq. (2.7) becomes much smaller than the $\mathcal{O}(T)$ correction $t/2$. As mentioned previously, the factor $\exp(-C(\gamma))$ for $T \to 0$ merges with the $\mathcal{O}(T^2)$ correction (due to $C(\gamma \to \infty) \sim \gamma^{-2}$). Therefore, roughly speaking, asymptotic scaling sets in at a temperature t_{AS} where the vertical distance between CH_2N_2 and CH_3N_2B (in the Memphis chart) becomes much smaller than

the vertical distance between CH_2N_2 and the line of unity. If "much smaller" is taken to mean "by at least one order", then this happens for $S = 1/2$ at $\xi/a \approx 10^5$ ($t_{AS} \approx 0.08$). However, the deviations from CH_2N_2 are always rather small compared to the 3-loop correction itself, even at $\xi/a \approx 100$ ($t_{AS} \approx 0.18$), for example.

The situation appears drastically different for $S > 1/2$. One can easily estimate t_{AS} from CH_3N_2B. The $\mathcal{O}(T^2)$ corrections for $T \to 0$ are still half of the leading-order correction $t/2$ at $\xi/a \approx 10^{12}$ ($t \approx 0.035$) for $S = 1$, or $\xi/a \approx 10^{32}$ ($t \approx 0.013$) for $S = 3/2$; for a typical atomic scale a, these values are macroscopic lengths of meters and light years. Asymptotic scaling would set in only at much larger correlation lengths. But even the above t values correspond to absolute temperatures much below the Néel-temperatures $T_N > 0$ at which long-range order occurs in real antiferromagnets due to small but nonzero couplings in the third direction. In consequence, real quasi-two-dimensional $S > 1/2$ antiferromagnets like La_2NiO_4 ($S = 1$) are never in the regime of renormalized classical scaling. On the other hand, our results definitively confirm that chiral perturbation theory, corrected for cutoff effects, yields a correct mapping of the AFHM onto the 2-d $O(3)$ model, and that this description of the AFHM correlation length holds down to moderate $\xi/a \approx 100 - 500$ for all spins. This comes pretty close to the regime $\xi/a \lesssim 100$ accessible in experiments.

Low Energy parameters

To compare $\xi(T)$ with the field-theoretical predictions, one has to choose values for the spin stiffness ρ_s and spin-wave velocity c. Because CH_2N_2, eq. (2.7), is an exact result for $T \to 0$, any candidates for the values of ρ_s and c are disqualified if they preclude asymptotic scaling of $\xi(T \to 0)$. The $S = 1/2$ study in Ref. [33] showed that the third-order spin-wave expansion (SW3) prediction for ρ_s definitely is about 3% too small, and precludes asymptotic scaling. On the other hand, SWE is an expansion in powers of $1/S$, and should become more accurate rapidly as spin increases. Indeed, our data recover the SW3 results for ρ_s and c rapidly as the spin S increases. Here are the results for various spins:

- For the $S = 1/2$ QMC data, the Memphis chart Fig. 4-1 uses $\rho_s = 0.1800(5)J$

and $c = 1.657(2)Ja$ from the QMC study in Ref. [33]. We find that fitting the data to CH$_3$N$_2$B for $S = 1/2$ does not change these values. (The SW3 predictions[51, 52, 53] are $\rho_s^{\text{SW3}} = 0.1746J$ and $c^{\text{SW3}} = 1.6680Ja$.) Ref. [33] fitted to the "no cutoff effects" prediction CH$_2$N$_2$, and required an αt^2 correction with a free fit parameter $\alpha = -0.75(5)$ to extend the range of validity from $\xi/a \approx 10^5$ down to $\xi/a \approx 100$. In contrast, the cutoff-corrected prediction CH$_3$N$_2$B has no such ambiguity, and its agreement with QMC down to $\xi/a \approx 10$ ($t \approx 0.3$) is striking. (This lower bound of agreement corresponds to $T/J \approx 6$ or an absolute temperature ≈ 600 K for Sr$_2$CuO$_2$Cl$_2$.)

- For $S = 1$, the QMC data in Fig. 4-1 smoothly merge into the CH$_3$N$_2$B prediction for $\xi/a > 50$ ($t < 0.17$) where $c/T > 3.3a$. We find that $\rho_s^{\text{SW3}} = 0.869$ and $c^{\text{SW3}} = 3.067$ are nearly correct. Figure 4-1 uses our result from a two-parameter fit, namely $\rho_s/\rho_s^{\text{SW3}} = 1.005(3)$ and $c/c^{\text{SW3}} = 0.98(2)$. These ratios correspond to $\rho_s = 0.8733(23)J$ and $c = 3.01(6)Ja$. The fit includes all data with $\xi/a > 100$ ($t < 0.15$) in Figure 4-1, and has an excellent $\chi^2/\text{d.o.f.} = 1.085$ with 58 degrees of freedom (which corresponds to a confidence level $P = 69.5\%$). The relative deviations of these fit results from SW3 are small, namely $0.5(3)\%$ for ρ_s and $-2(2)\%$ for c. However, this near overlap is deceptive, and in fact is seriously significant due to the high correlation between the fit parameters: compared to the two-parameter fit, SW3 values yield an unacceptable $\Delta\chi^2 = +20.2$. This situation is described in Section 4.1 below.

- For the $S > 1$ data, we could not identify any deviation from the SW3 values, and these were used in Figure 4-1. Agreement of QMC with CH$_3$N$_2$B with good $P \lesssim 80\%$ starts at $\xi/a > 200$ ($t < 0.17$) for $S = 3/2$, $\xi/a \gtrsim 400$ ($t < 0.1$) for $S = 2$, and $\xi/a \gtrsim 600$ ($t < 0.1$) for 5/2. We could also perform a two-parameter fit for $S = 3/2$ which is in agreement with the SW3 values. For $S = 2$ and 5/2, however, we have not generated enough data points for stable two-parameter fits to fix the lower bound of agreement with CH$_3$N$_2$B more accurately. (In these fits, the correlation coefficient for ρ_s and c is $r \approx -0.997$.)

The ranges of agreement and the corresponding $\chi^2/$d.o.f. values are summarized for all spins in Table 4.1.

Table 4.1: The QMC ξ/a data fit well to the prediction CH_3N_2B, eq. (2.10). For all $S > 1$, third-order spin-wave expansion [SW3, eq. (2.9)] connects CH_3N_2B with the QMC data consistently. The subscript "min" ("max") denotes the smallest (largest) values included in the fit and χ^2 statistics. $t = T/2\pi\rho_s$, $\theta \equiv \rho_s/c^2$, ν is the number of degrees of freedom. P is the confidence level.

	t_{max}	t_{min}	ξ_{min}/a	ξ_{max}/a	ρ_s/J	$c/(Ja)$	$\theta/(Ja^2)$	ν	χ^2/ν	$P[\%]$
S = 1/2										
Third-order spin-wave theory	0.22	0.074	39.4(3)	399 000(12 600)	0.1746	1.6680	0.0627	8	1.4	81
With ρ_s and c from Ref. [33] [a]	0.22	0.074	39.4(3)	399 000(12 600)	0.1800(5)	1.657(2)	0.09376(5)	8	1.03	59
S = 1										
Third-order spin-wave theory	0.152	0.15	100(2)	171 000(7100)	0.8690	3.0670	0.09238	60	1.390	97.5
This work, free two-parameter fit	0.152	0.15	100(2)	171 000(7100)	0.8733(23)	3.01(6)	0.096(4)	58	1.085	69.5
This work, constrained fit [b]	0.152	0.15	100(2)	171 000(7100)	0.8711(24)	3.07(6)	0.092(4)	59	1.083	69.2
S = 3/2										
Third-order spin-wave theory	0.119	0.064	306(8)	614 000(38000)	2.0612	4.4761	0.10287	34	1.14	73.7
This work, free two-parameter fit	0.110	0.064	656(21)	614 000(38000)	2.074(8)	4.3(2)	0.115(10)	29	0.54	4
S = 2										
Third-order spin-wave theory	0.106	0.067	529(15)	191 000(12000)	3.7529	5.8878	0.10825	19	1.01	55.6
S = 5/2										
Third-order spin-wave theory	0.096	0.067	923(41)	135 000(9700)	5.9444	7.3005	0.11153	22	1.44	91.5
Third-order spin-wave theory	0.089	0.067	2300(94)	135 000(9700)	5.9444	7.3005	0.11153	20	1.00	54.0

[a] Not a fit to CH_3N_2B. These ρ_s and c values were obtained in Ref. [33] by fitting to the "no cutoff effects" prediction CH_2N_2, eq. (2.7). Here, we use these results to calculate the χ^2 statistics for the QMC data compared to CH_3N_2B.

[b] Fit constrained to $\rho_s/c^2 = \theta^{SW_3}$. Details are described in the Section 4.1.

49

Significance of the Cutoff Correction

The agreement with CH_3N_2B in each case degrades above some temperature. This is to be expected because CH_3N_2B leaves out higher-order terms from the CPT and spin-wave expansions. In addition, as explained in the previous section, at high temperatures the field-theoretical requirements, eqs.(2.8), are no longer satisfied. The regimes where the residual discrepancies between $S > 1/2$ QMC and CH_3N_2B appear is rather close to these limitations.

However, the calculation of the cutoff correction $\exp(-C(\gamma))$ by Hasenfratz[38] was performed only in bilinear (first-order) spin-wave expansion. It is interesting to ask whether the description in the regime of degradation could be improved by higher-order corrections in the SWE calculation and in the CPT expansion. (The latter will introduce new, unknown coupling parameters.)

From our $S = 5/2$ data we can make a statement about this question. In Figure 4-2 we plot the ratio of ξ/a to CH_3N_2B versus $1/\log_{10}(\xi/a)$ for $S = 1/2, 1, 5/2$, and ∞. For $S \to \infty$, the AFHM becomes the standard lattice-regularized 2-d nearest-neighbor $O(3)$ model with bare coupling $g_0 = JS^2/T$. The asymptotics of $C(\gamma)$ for large spin and $\rho_s \gg T \gg c/a$ ("classical scaling regime") follows from $\gamma \equiv 2JS/T \sim (c/a)(1 + \mathcal{O}(1/S))/T$, and is found[38] to be $C(\gamma \to 0) \sim \pi/2 + \ln 8 + \mathcal{O}(\gamma)$. Plugging this into the CH_3N_2B formula, eq. (2.10), yields the known[64, 65] result for the lattice $O(3)$ model,

$$
\frac{1}{a} \xi_{\text{classical}} = \frac{\exp(-\pi/2)}{\sqrt{32}} \frac{e}{8} t \exp\left(\frac{1}{t}\right)
$$
$$
\times \left[1 - \frac{t}{2} + \frac{27}{32} t^2 + \mathcal{O}\left(\frac{c/a}{T}\right)\right], \tag{4.1}
$$

where $\rho_s \sim JS^2 \sim \rho_{\text{class}}$. Thus, CH_3N_2B smoothly connects the regimes of classical scaling and renormalized classical scaling ($T \ll \rho_s$). The fact that the correct prefactor $\exp(-\pi/2)/\sqrt{32}$ comes out of $\exp(-C(\gamma))$ is a non-trivial check on the cutoff calculation by Hasenfratz.

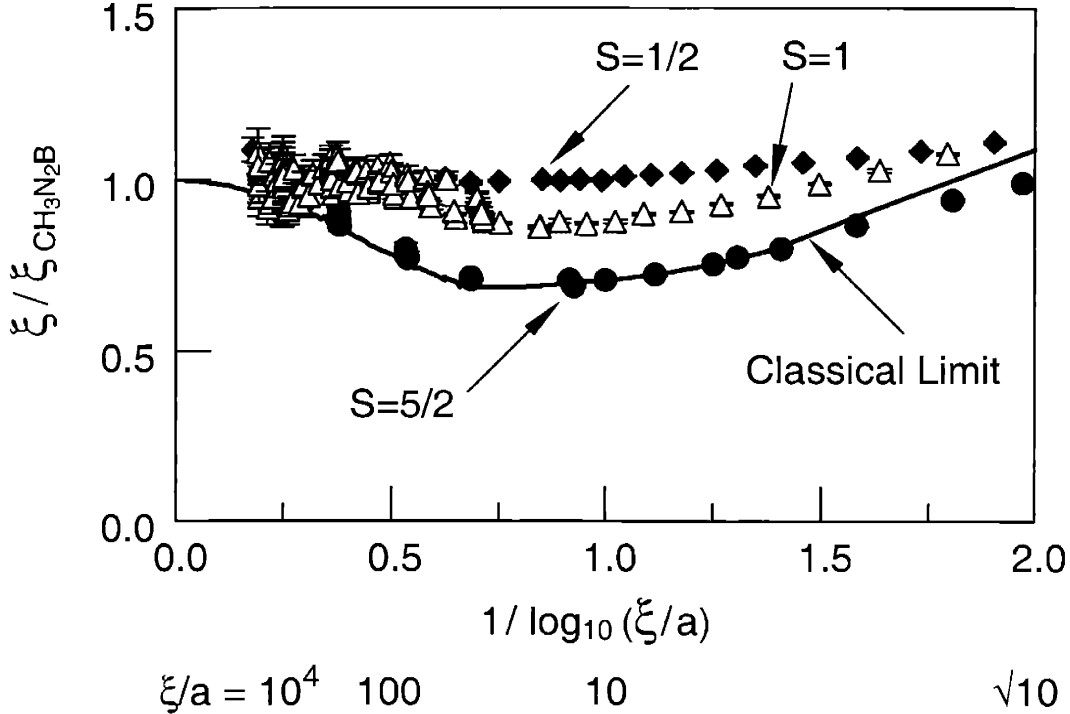Equation (4.1) was used to normalize the $S = \infty$ data. These are available from

Figure 4-2: Ratio of correlation length ξ to CH_3N_2B prediction vs. ξ, for $S = 1/2, 1, 5/2, \infty$. By $S = 5/2$ the residual deviation essentially reaches the classical $S = \infty$ limit.

analytical calculations[66, 67] ($\xi/a \geq 10^5$), Monte Carlo simulation[68, 69] ($10 \leq \xi/a \leq 10^5$), and series expansion[26] ($\xi/a \leq 10$) for the $O(3)$ model.

We find that by $S = 5/2$ the discrepancy between the QMC data and CH_3N_2B has already essentially reached the classical limit $S \to \infty$. This gives significance to the assumption that a higher-order calculation of the cutoff effects would not significantly contribute to an improvement. Furthermore, it shows that the reasons for the residual discrepancy can be investigated in the $O(3)$ model and are not unique to the quantum AFHM.

4.1 Fit Details and Constrained Fit for $S = 1$

The fit parameters ρ_s and c are strongly anticorrelated, with correlation coefficient $r = -0.977$, and thus have large uncertainties with nearly degenerate confidence

ellipses. The $S = 1/2$ QMC study by Beard and Wiese [33] combined the correlation length data fit to the "no cutoff effects" prediction CH_2N_2, eq. (2.7), with a fit of finite-volume magnetic susceptibilities[41, 6] to the predictions of CPT for the finite-size and temperature effects in the AFHM[30, 31]. The specific appearance of ρ_s and c in the susceptibilities leads to a strong *positive* correlation in the fits, so that a combination of both data fits yields a very high precision. This is much more efficient than calculating a lot of correlation length data for a single fit.

For the present analysis, we have chosen a different approach which involves only the correlation length. Rather than achieving a high fit precision, we merely want to show that for $S > 1$ one can directly rely on the SW3 predictions[51, 52, 53] to see a consistent connection between the QMC data and CH_3N_2B, that is, an agreement with good confidence levels from the $\chi^2/$d.o.f. values when using SW3 predictions. This is indeed the case for $S > 1$ as our results in Table 4.1 show.

The $S = 1$ case remains somewhat subtle. The results of the free two-parameter fit quoted above yield a near overlap with the SW3 results, namely $\rho_s/\rho_s^{SW3} = 1.005(3)$ and $c/c^{SW3} = 0.98(2)$. But this is deceptive since the SW3 values yield $\chi^2/60 = 1.39$, that is, a poor fit with $P = 97.5\%$. Furthermore, SW3 values yield $\Delta\chi^2 = +20.2$ compared to the two-parameter fit, which is outside the 99.99% confidence region. The situation is shown in Figure 4-3, where we plot the deviations $\Delta\rho_s/\rho_s^{SW3}$ and $\Delta c/c^{SW3}$ on the x- and y-axis, respectively, with $\Delta\rho_s \equiv (\rho_s - \rho_s^{SW3})$ and $\Delta c \equiv (c - c^{SW3})$. The result of the two-parameter fit (with one standard deviation error bars) is shown together with its P=68.3% joint probability distribution confidence ellipse which has $\Delta\chi^2 = +2.30$. (The SW3 result has $\Delta\chi^2 = +20.2$.)

Interestingly, the major axis of the nearly degenerate confidence ellipse is almost orthogonal to the curves of constant ratio $\theta \equiv \rho_s/c^2$. In particular, the specific curve $\rho_s/c^2 = \theta^{SW3}$ intersects this confidence ellipse. In other words, this 68.3% confidence region contains (ρ_s, c) values which are consistent with $\theta = \theta^{SW3}$. We are thus motivated to check how close to ρ_s^{SW3} and c^{SW3} the corresponding single-parameter-fit values could in fact be.

To do this, we set $\theta_{S=1} \equiv \theta_{S=1}^{SW3} = 0.09238$ and performed a fit with the same set of
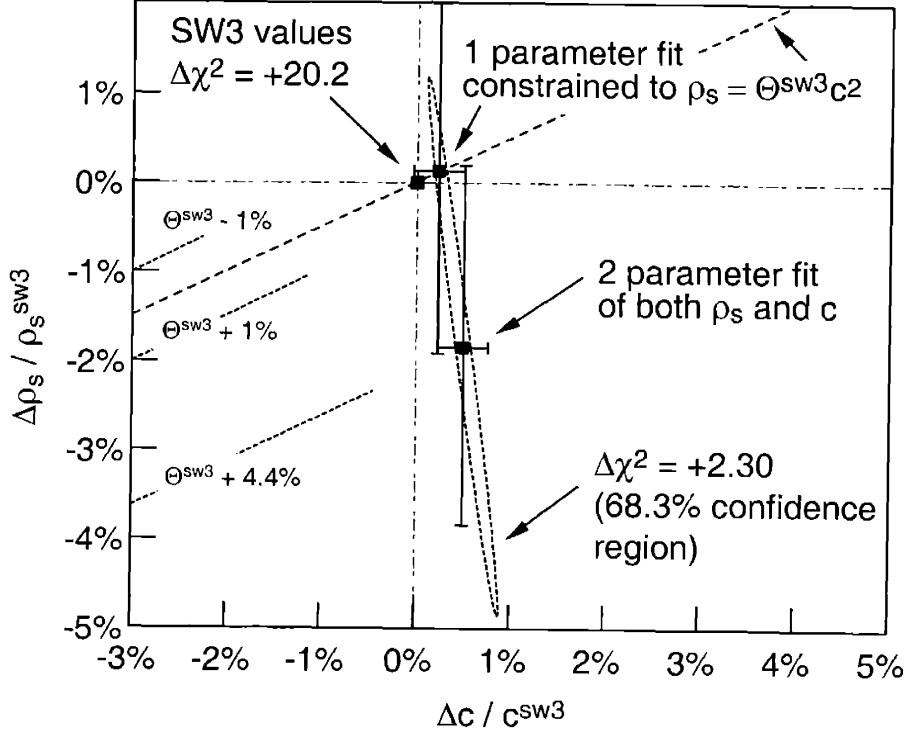
Figure 4-3: Two- and one-parameter fits for $S = 1$. The 68.3% confidence ellipse of the joint probability distribution of the free fit intersects the curve $\theta = \theta^{\text{sw3}}$. The result of 3rd order spin-wave expansion (SW3) has $\Delta\chi^2 \approx +20$ compared to fits.

$S = 1$ QMC data, but constrained it to the one-dimensional parameter subspace $\rho_s = \theta^{\text{sw3}}c^2$. As an upper bound for the error associated with the hypothesis $\theta_{S=1} = \theta^{\text{sw3}}_{S=1}$, we took from Ref. [33] the 4.4% deviation between $\theta^{\text{sw3}}_{S=1/2} = 0.06277$ and that study's result $\theta_{S=1/2} = 0.06556$. This choice is conservative since SWE is an expansion in powers of $1/S$, and is expected to become more accurate as spin increases.

Upon refitting, we found $\rho_s/\rho_s^{\text{sw3}} = 1.0024(27)$, $c/c^{\text{sw3}} = 1.001(21)$, and $\chi^2/59 = 1.083$ ($P = 69.2\%$). These ratios correspond to $\rho_s = 0.8711(24)$ and $c = 3.07(6)$. (The difference between the one- and two-parameter fits would not be visible in the Memphis chart, Fig. 4-1.) By definition, this point lies on the curve $\Delta c/c^{\text{sw3}} = (\Delta\rho_s/\rho_s^{\text{sw3}} + 1)^{1/2} - 1$ which goes through the origin $\Delta c = \Delta\rho_s = 0$.

Note that this is a *methodological* issue. In principle, the results of the constrained one-parameter and the free two-parameter fits cannot be distinguished statistically since the former has $\chi^2/58 = 1.085$ ($P = 69.5\%$), while the latter has $\chi^2/59 =$

1.083 ($P = 69.2\%$). The difference is only $\Delta\chi^2 = +0.97 \ll +2.30$. Also note that in the constrained fit the assumed (systematic) 4.4% uncertainty in $\theta_{S=1}$ is a conservative upper bound. It does not influence the fit results for ρ_s and c but completely dominates their errors. But the actual errors are supposed to be much smaller, thus the result $\rho_s/\rho_s^{\mathrm{SW3}} = 1.0024(27)$ is not superior to the free fit result 1.005(3). However, the methodical significance of the constrained fit is that one can use a result from SW3 for $S = 1$ too, namely the ratio θ^{SW3}, yielding a best fit result (ρ_s, c) very close to the SW3 results for the single parameters. This is not obvious, and it is not possible for $S = 1/2$. The result reflects that nothing stands against the hypothesis that the true ρ_s is indeed very close to ρ_s^{SW3}. This can be pinned down only by using an independent fit result for θ to break the strong anticorrelation of the fit parameter in the correlation length fit; the finite-volume susceptibility data fit to CPT predictions is a good method[62] to obtain an independent estimate for θ.

4.2   Finite-Size Scaling of the Correlation Length

The asymptotic field-theoretical prediction CH_2N_2, eq. (2.7), refers to infinite volume. Even with very efficient Monte Carlo algorithms, however, lattices larger than $L/a = \mathcal{O}(100)$ are computationally prohibitive. In order to extrapolate the finite-L correlation length to infinite volume, we used finite-size scaling techniques on our raw QMC data to obtain the results quoted above.

Finite-size scaling is based on the observation that $\xi(L)$ of a system with periodic boundary conditions and spatial size $L \times L$ is a universal function f_ξ of $\xi(\infty)/L$,

$$\frac{\xi(L)}{\xi(\infty)} = f_\xi \left(\frac{\xi(\infty)}{L} \right) . \tag{4.2}$$

Similar finite-size scaling methods based on (4.2) where used by Kim[70] and Caracciolo et al.[68] to test asymptotic scaling of the correlation length with the bare coupling constant in the 2-d nearest-neighbor lattice $O(3)$ model. Caracciolo et al.[68] used

the ansatz

$$\frac{\xi(2L)}{\xi(L)} = F_\xi \left(\frac{\xi(L)}{L} \right) , \tag{4.3}$$

The universal function F_ξ was determined by Caracciolo *et al.*[68] numerically very precisely from their $O(3)$ model Monte Carlo data. Finite-volume $\xi(L)$ can then be extrapolated to infinite volume by iteration of (4.3), causing an extrapolation error of only a few percent even if $\xi(\infty)$ is 1000 times larger than the lattice size L. We will use the mnemonic "CEFPS" to refer to this method.

As explained in Sec. 2.1, the $d = 2+1$ AFHM at low temperatures becomes the $d = 2$ $O(3)$ model due to dimensional reduction $\xi \gg c\beta$. Both models are assumed to be in the same universality class, and one may utilize the CEFPS technique for AFHM finite-size scaling too. This was first done in Ref. [33] for the $S = 1/2$ case, and we use exactly the same technique in the present paper. We emphasize that F_ξ assumes universal behavior, that is scaling, not asymptotic scaling, and thus yields $\xi(L \to \infty)$ without bias.

We verified the validity of the $O(3)$ model scaling (4.3) for the AFHM for all $S \le 5/2$. Our results[63] are shown in Figure 4-4, where the ratio $\xi(2L, T, S)/\xi(L, T, S)$ and CEFPS F_ξ are plotted versus $\xi(L)/L$ for a broad range of $L/a \ge 10$ and T/J values. Even for lattice sizes as small as $L/a \approx 10$ we could not observe any scaling violations on our level of precision, which is $\sim 0.2\%$ for $\xi(L)$, including the auto-correlation error induced by the Markov chain of the Monte-Carlo simulation (see Sec. 4.3). Also shown in Figure 4-4 is the perturbative prediction[68]

$$F_\xi^{\mathrm{PT}} = 2 - \frac{\ln 2}{4\pi x^2} - \left(\frac{4\ln 2 + 16}{64\ln 2} \right) \left(\frac{\ln 2}{2\pi x^2} \right)^2 + \mathcal{O}(x^{-6}) , \tag{4.4}$$

which is valid for $x = \xi(L)/L \gg 1$.

However, recovering the $O(3)$ model scaling in the AFHM is not as straightforward as Figure 4-4 implies. As mentioned, dimensional reduction is the key observation for both the mapping of the AFHM onto the 2-d $O(3)$ model and the application of CEFPS scaling for the AFHM. In simulation practice one has the limitation $\xi(L) = \mathcal{O}(L)$, and therefore encounters the situation $\xi(L) \approx k_\xi c\beta$ where k_ξ is a $\mathcal{O}(1)$ or $\mathcal{O}(10)$
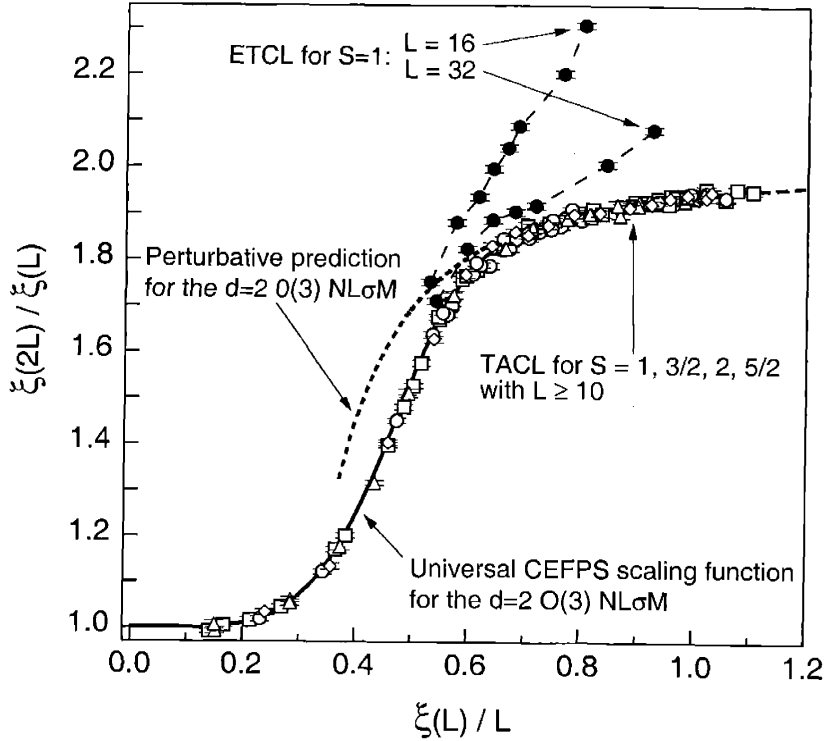
Figure 4-4: Universal scaling in the AFHM. The time-averaged correlation length (TACL) for $S = 1$ (open circles), 3/2 (squares), 2 (diamonds), and 5/2 (triangles) for various lattice sizes $10 \leq L \leq 180$ and temperatures (not distinguished) agrees well with the universal scaling function (CEFPS, solid line) of the $O(3)$ model, while the equal-time correlation length (ETCL, solid circles, only $S = 1$ shown) has large scaling violations. The figure contains 119 TACL points (94 from the discrete-time, 25 from the continuous-time algorithm).

number, even though $\xi(\infty) \gg c/T$ is exponentially large. It seems unjustified to use CEFPS scaling then. In fact, our results show that $\xi(L) \gg c\beta$ (with $\xi(\infty) \gg c\beta$) is not a controllable criterion which allows us to recover CEFPS scaling with a usual correlation length definition based on the equal-time two-point correlator.

4.2.1 Time-averaged vs. equal-time correlation length

To obtain correlation lengths, it is conventional to use the spatial static structure factor function $S(\mathbf{q})$, which is nothing other than the Fourier transform of the equal-

time two-point correlator $C(\mathbf{r}) \equiv \langle \mathbb{S}_0 \mathbb{S}_\mathbf{r} \rangle$ On the lattice, this function takes the form

$$S(\mathbf{q}) = \sum_\mathbf{r} \exp(i\mathbf{qr})C(\mathbf{r}),$$

at lattice Brillouin zone wave vector $\mathbf{q}$. If the structure factor peak $S(\mathbf{Q})$ occurs at the vector $\mathbf{Q}$ of total ordering, the second-moment correlation length is

$$\xi_E^{(2)}(L) \equiv \frac{L}{2\pi} \sqrt{\frac{S(\mathbf{Q})}{S\left(\mathbf{Q} + (\frac{2\pi}{L}, 0)\right)} - 1} + \mathcal{O}\left(\frac{2\pi}{L}\right)^2, \tag{4.5}$$

When the correlation function contains only one mode, $C(\mathbf{r}) = A \cosh(\frac{x - L/2}{\xi})$ around $\mathbf{Q} = \mathbf{0}$, this second moment formula returns ξ exactly. This is the definition used by Caracciolo et al.[71] for the 2-d $O(3)$ model (where $\mathbf{Q} = (0,0)$).

Definition eq. (4.5) is directly applicable for the quantum AFHM where $\mathbf{Q} = (\pi, \pi)/a$, and $S(\mathbf{0})$ and $S(\mathbf{Q})$ are the averages of the squared total uniform and staggered magnetization operators, respectively. We use the names "equal-time correlation function" (ETCF) and "equal-time correlation length" (ETCL) to refer to the static quantities $C(\mathbf{r})$ and $\xi_E^{(2)}(L)$ defined according to (4.5) in the quantum model.

Previous QMC studies by, for example, Makivić and Ding[72] ($S = 1/2$), Kim and Troyer[50] ($S = 1/2$), and Harada et al.[7] ($S = 1$) used a second-moment correlation length defined similar to (4.5). These authors did not use finite-size scaling but instead increased the lattice size until $L > 6\,\xi(L)$ to force finite-size effects into the statistical error. Their $\xi/a < 120$ results are in excellent agreement with our ETCL results. For $S = 1/2$ and 1 one has $c/T \approx 2J/T$ and $\approx 3J/T$, respectively. The temperatures for $\xi/a < 120$ are $T/J \leq 1$, thus $k_\xi \lesssim 3 - 60$. This may or may not be a sufficient fulfillment of $\xi \gg c/T$ for comparison with the field-theoretical prediction $\xi_{\text{AS}} = CH_2N_2$ and its successors.

However, for lower temperatures where $\xi/a \gg 100$, the direct measurement on $L > 6\,\xi(L)$ lattices is not possible, and one has to obtain large $\xi(\infty)$ from small $\xi(L) \ll \xi(\infty)$ using finite-size scaling. The iteration of the universal CEFPS scaling function F_ξ is extremely sensitive to small variations of $\xi(L)$. Our results clearly show

that finite-volume ETCL in the AFHM is not the length which scales according to the universal function F_ξ. As a matter of fact, there occur large scaling violations even though $\xi(L = \infty) \gg c/T$ and $\xi(L) \gg c/T$ ($c/T \ll L$).

Our solution to this problem is the observation that it is not the static structure factor function $S(\mathbf{q})$ but the magnetic susceptibility function $\chi(\mathbf{q})$ which enables universal correlation length scaling in the quantum model. We introduce the parallel magnetic susceptibility function $\chi^\parallel(\mathbf{q}) \equiv \chi(\mathbf{q})/3$ as usually defined in the AFHM from the Gibbs free energy $G(T, h)$ and an external magnetic field $h \to 0$ parallel to the direction of quantization:

$$G(T, h) \equiv -T \ln \mathrm{Tr}\left[\exp\left(-\frac{1}{T}(\mathbb{H} - h\,\mathbb{M}_z(\mathbf{q})) \right) \right] \tag{4.6}$$

$$\chi^\parallel(\mathbf{q}) \equiv \left. \frac{\partial^2}{\partial h_s^2} G(T, h) \right|_{h=0} \tag{4.7}$$

$$= \int_0^{1/T} d\tau \left\langle \mathbb{M}_z(\mathbf{q}, 0)\mathbb{M}_z(\mathbf{q}, \tau) \right\rangle - \frac{1}{T}\left\langle \mathbb{M}_z(\mathbf{q}) \right\rangle^2$$

$$\mathbb{M}_z(\mathbf{q}, \tau) \equiv e^{\tau \mathbb{H}} \mathbb{M}_z(\mathbf{q})\, e^{-\tau \mathbb{H}} \tag{4.8}$$

$$\mathbb{M}_z(\mathbf{q}) \equiv \sum_{\mathbf{r}} \exp(i\mathbf{q}\mathbf{r})\mathbb{S}_{\mathbf{r}}^z\,, \tag{4.9}$$

with $\mathbb{S}_{\mathbf{r}}^z$ the third component of the spin operator, and $\mathbb{H}$ the AFHM Hamilton operator, eq. (2.1). $\mathbb{M}_z^s \equiv \mathbb{M}_z(\mathbf{Q})$ is the total staggered magnetization operator, and $\chi_s^\parallel \equiv \chi(\mathbf{Q})$ is the parallel staggered susceptibility. The zero-field average of the total staggered magnetization is zero in finite volume due to the $O(3)$ symmetry, and it is zero in infinite volume due to the Mermin-Wagner-Coleman theorem[44, 45] which rules out spontaneous ordering magnetization at $T > 0$ in two dimensions.

Therefore, after replacing $S(\mathbf{q})$ in definition (4.5) by $\chi^\parallel(\mathbf{q})$, we get what we call the second-moment "time-averaged correlation length" (TACL):

$$\xi_T^{(2)}(L) \equiv \frac{L}{2\pi} \sqrt{\frac{\chi^\parallel(\mathbf{Q})}{\chi^\parallel\left(\mathbf{Q} + (\frac{2\pi}{L}, 0)\right)} - 1} + \mathcal{O}\left(\frac{2\pi}{L}\right)^2 \tag{4.10}$$

$$\chi^\parallel(\mathbf{q}) \equiv \int_0^{1/T} d\tau \left\langle M_z(\mathbf{q}, 0)\, M_z(\mathbf{q}, \tau) \right\rangle\,, \tag{4.11}$$

where $\mathbb{M}_z(\mathbf{q}, \tau)$ is given by eq. (4.8).

As examples, some $S = 1$ ETCL $\xi_E^{(2)}(L)$ results are contained in Fig. 4-4. The scaling violations are serious, they become larger for lower temperatures, and they do not allow for finite size scaling at all. Note that the violations become smaller for larger lattice sizes (at fixed T) since $\xi_E^{(2)}(L)$ can grow compared to the fixed c/T extent. However, this 'improvement' for larger L is not controllable. In contrast, TACL ($\xi_T^{(2)}(L)$) scales in excellent agreement with F_ξ even for small lattices $L = 10$, and for all temperatures involved in scaling to $\xi/a = 20 - 10^5$. In our analysis, we used various lattice sizes $L = 10$, 16, 20, 32, 40, 64, 128, and 180 to iterate $\xi_T^{(2)}(T, L \to \infty)$ for a fixed temperature T. Within statistical errors, the data points in such a multiplet are generally consistent.

In conclusion, our observation is that the static susceptibility function $\chi(\mathbf{q})$ enables universal second-moment correlation length scaling in the AFHM, while the equal-time structure factor function $S(\mathbf{q})$ does not. This agrees qualitatively with analytical considerations[73, 74] which imply that $S(\mathbf{q})$ in the AFHM cannot exhibit universal scaling behavior. Note that our result shown in Fig. 4-4 is a non-trivial support of the common assumption that the 2-d $O(3)$ model and the AFHM are in the same universality class.

We mention an intuitive argument for using the susceptibility function rather than the static structure function in the definition of the second-moment correlation length. Equation (4.11) can be easily translated back into the corresponding two-point correlator, namely $G(\mathbf{r}, \tau) \equiv \langle \mathbb{S}(0, 0)\mathbb{S}(\mathbf{r}, \tau) \rangle$. The TACL second-moment definition, eq. (4.10), is nothing else than the standard ETCL definition, eq. (4.5), but with another two-point correlator which is averaged over the Euclidean-time direction (with $\mathbf{r}$ fixed), namely $\bar{C}(\mathbf{r}) \equiv T \int_0^{1/T} d\tau\, G(\mathbf{r}, \tau)$ instead of the equal-time $C(\mathbf{r})$. This is the origin of the term "time-averaged." Even for infinite volume, the equal-time two-point correlator $C(\mathbf{r})$ contains higher "mass" modes in the Euclidean-time direction. However, after dimensional reduction, these modes are exponentially suppressed in infinite volume since $\xi(\infty)$ is exponentially large compared to the Euclidean-"time" extent of the slab, $\xi \gg c\beta$.

In finite and small volumes at all temperatures, however, we have $\xi(L) \sim c/T$, and the higher-mass modes give significant contributions not much above the lowest mass mode. In fact, it turns out that strictly $\xi_T^{(2)}(L) > \xi_E^{(2)}(L)$. In a finite-size scaling of $\xi_E^{(2)}(L)$, these higher-mass modes are scaled too, though we know that they cannot play a role in infinite volume. It is therefore reasonable to "wipe" them out of the correlation function before going into finite size scaling with $\xi(L)$. Since the system is periodic in the Euclidean-time direction, a perfect way to keep only the zero mode of $C(\mathbf{r}) \equiv G(\mathbf{r}, 0)$ is to average over this direction, thus using $\bar{C}(\mathbf{r})$ rather than $C(\mathbf{r})$. This is exactly the same as the replacement of $S(\mathbf{q})$ by $\chi^\parallel(\mathbf{q})$ in the ETCL definition eq. (4.5).

We naturally identify $\xi^{(2)}(\infty)$ with the physical length scale ξ_{exp} (the inverse mass gap), which enables us to compare our QMC results directly with the field-theoretical prediction CH_2N_2 and its successors. However, this identification is not at all obvious. We merely point out that several results exist for the ratio of both lengths in the 2-d $O(N)$ model. The large-N expansion[75, 76, 77, 68] gives $\xi_{\text{exp}}/\xi^{(2)} \approx 1.0032$. An analytical calculation[78] for the AFHM at low temperatures predicts 1.0035. Recently[79], the ratio for the $O(3)$ model was calculated numerically very precisely, $\xi_{\text{exp}}/\xi^{(2)} = 1.000826(1)$. All these results are fully close enough to unity to be completely irrelevant for the purpose of comparing our QMC data with the field-theoretical predictions derived from the $O(3)$ model.

4.2.2 Extreme correlation lengths

We have also obtained data for extremely large and extremely small correlation lengths in order to clarify the distinction between TACL and CEFPS further.

In eq. (4.4) we have quoted the perturbative prediction F_ξ^{PT} for the scaling of $\xi(L)$. Although this result is valid for $x \equiv \xi(L)/L \gg 1$, it is extremely close to the CEFPS function F_ξ already for $x = \mathcal{O}(1)$. For $x \geq 0.8$, the discrepancy between both is smaller than 0.1%, and becomes smaller than 0.04% for $x \geq 0.9$. Therefore, we used F_ξ^{PT} to continue the CEFPS prediction to values $x \leq 2.5$, and calculated ξ/a up to extreme values on the order of 10^{33} — this corresponds to 10^{23} meters for "real"

60

materials. We did *not* include these extreme data into the fits discussed above (which used $\xi/a \lesssim 10^6$). The results are shown in Figure 4-5, where we plot QMC $\xi(\infty)/a$ and CH_3N_2B versus T/J, using the values for spin stiffness ρ_s and spin-wave velocity c obtained in our fit for $S = 1$, and the predictions of third-order spin-wave theory for $S > 1$. The lattice sizes for the QMC measurements of $\xi(L)$ were $L/a = 16 - 32$. The excellent agreement up to such extreme $\xi(\infty)$ is astonishing, and gives further reliability to our approach of using TACL for scaling. We point out that a systematic study of the agreement between QMC and F_ξ^{PT} could enable determination of ρ_s and c with a much higher accuracy than we achieved for $\xi/a \sim 10^5$ with CEFPS scaling alone.
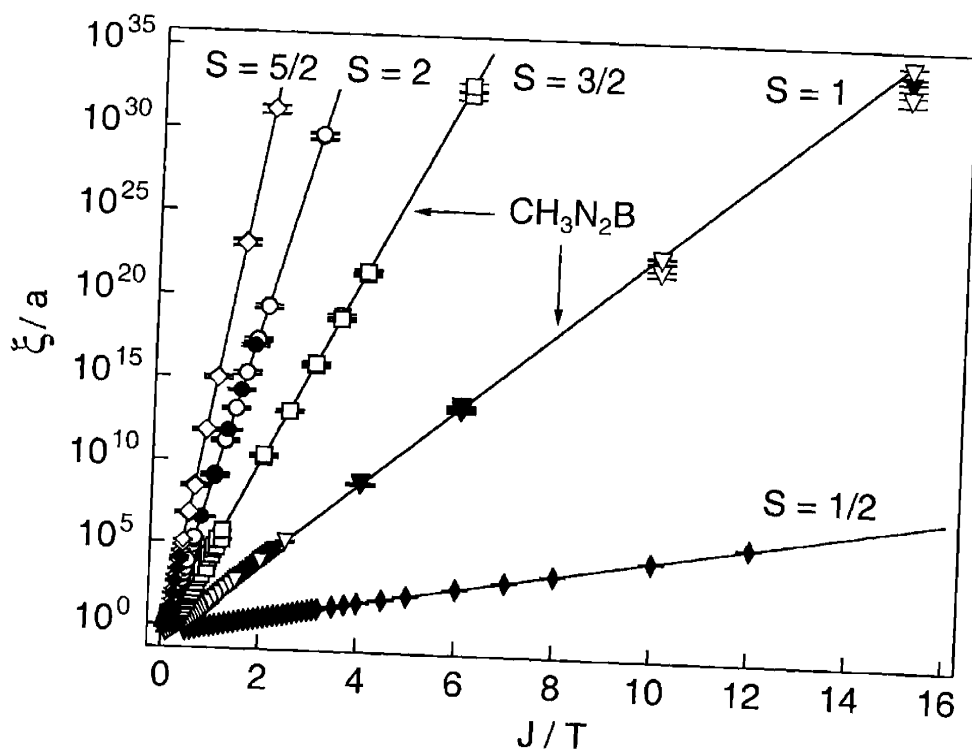
Figure 4-5: Finite-size scaling to extreme values. The $\xi/a > 10^6$ results are from continuation of CEFPS with the perturbative prediction eq. (4.4) for $1 < \xi(L)/L < 2.5$ with $L/a = 16$, 32 for $S > 1$, and $L = 16$, 20, 32 for $S = 1$. The CH_3N_2B predictions (solid lines) use SW3 values ρ_s and c for $S > 1$, and the fit result from $\xi/a < 10^6$ for $S = 1$. Open (filled) symbols are from the discrete (continuous) Euclidean-time algorithm. Good agreement with CH_3N_2B at these extreme values implies reliability for the usage of TACL.

For very small correlation lengths $\xi/a \approx 0.1 - 2$, we compared our TACL and ETCL with high-temperature series expansion[26] (HTE). This, too, is a second-moment result, and it provides both ETCL and TACL through the series expansion results for $S(\mathbf{q})$ and $\chi(\mathbf{q})$. Figure 4-6 shows the results for $S = 1$ with $1 \leq T/J < 4$ and $10 \lesssim \xi/a \leq 0.5$. (Note that we used $L > 10\,\xi(L)$, thus these $\xi(L)$ are infinite-volume results within the statistical error.) The agreement between HTE and QMC results is excellent for both TACL and ETCL with $T/J \gtrsim 2$ ($\xi/a \lesssim 2$). Note that $c/T \approx 3a$ for $S = 1$, which means that $\xi/a \lesssim c/T$ in this regime of Fig. 4-6, thus ETCL and TACL cannot be equal even in infinite volume. For only slightly smaller temperatures in Fig. 4-6, however, they get close (in *infinite* volume) due to $\xi/a \gg c/T$.
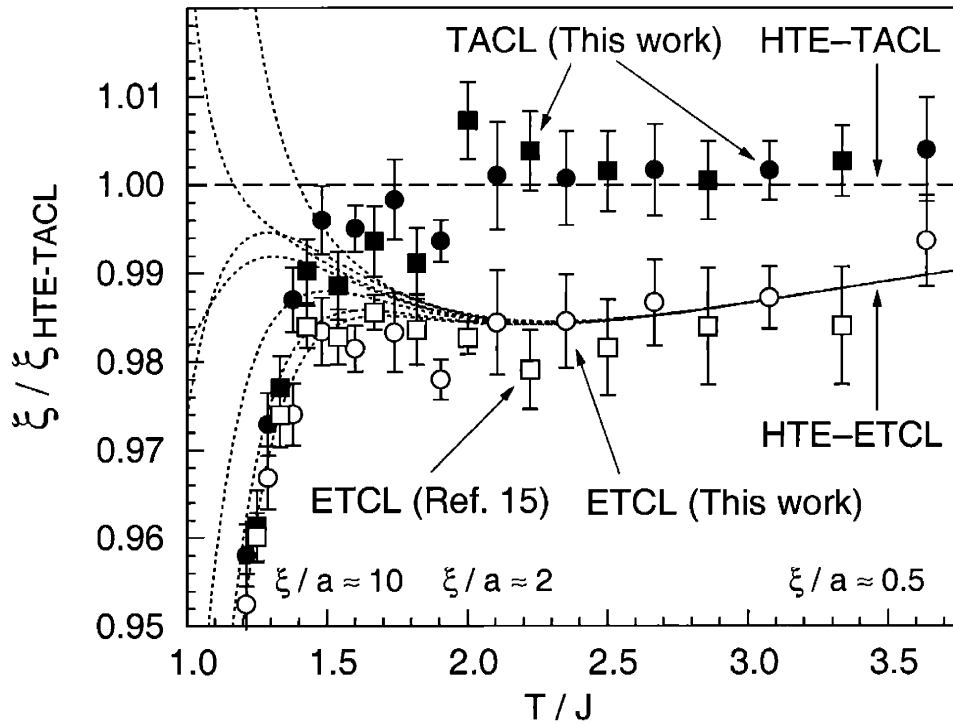
Figure 4-6: Equal-time (ETCL) and time-averaged (TACL) correlation lengths for $S = 1$ at $\xi/a < 10$, compared with high-temperature series expansion[26] (HTE). The agreement of QMC-TACL (filled symbols) and QMC-ETCL (open symbols) with HTE-TACL (dashed line) and HTE-ETCL (dotted line), respectively, is excellent for $T/J > 2$ ($\xi/a < 2$). Circles (filled squares) are from the discrete (continuous) time algorithm. Open squares are the QMC-ETCL data from Ref. [7]. HTE-ETCL is plotted for various Padé approximants.

62

4.3 Autocorrelation Errors and Times

The QMC results in this work are from simulation runs with measurement on 10^5 successive loop-cluster updates ("configurations"), after discarding 10^4 transient states for thermalization. The lattice sizes were $L/a \le 180$.

All our QMC results have true errors; that is, they include the autocorrelation error induced by the finite Markov chain of the Monte-Carlo simulation. The integrated autocorrelation times for the observables were determined for both algorithms to be $\tau_{\mathcal{A}} \approx 1.18(5)$ measurements, where $\mathcal{A}$ stands for $\xi_E(L)$, $\xi_T(L)$, $S(\mathbf{q})$, and $\chi(\mathbf{q})$. ($\tau_{\mathcal{A}} = 1$ means no autocorrelation.) The $\tau_{\mathcal{A}}$ turned out to be essentially independent of temperature, lattice size, and spin magnitude.

The VLC data include the individual autocorrelation errors for each data point, while the LATTHS data use an overall estimate $\tau_\xi = 1.15$, by which the naive variance $\sigma^2_{\text{naive}} = \langle \mathcal{A}^2 \rangle - \langle \mathcal{A} \rangle^2$ is increased, and the true error is calculated as $\sigma_{\text{true}} = \sqrt{\tau_{ac}}\, \sigma_{\text{naive}}$.

We use the standard techniques and definitions of time-series analysis[80, 81, 82, 83, 84, 85, 86] to estimate the true variance $\text{Var}[\bar{\mathcal{A}}_N]$ of the unbiased average $\bar{\mathcal{A}}_N$ and the integrated autocorrelation time $\tau_{\mathcal{A}}$ of the observable $\mathcal{A}$ from a sequence of N successive measurements $\mathcal{A}_n$, $n = 0, 1, \ldots, N-1$. A Monte Carlo simulation of our type is (after equilibration) an ergodic, irreducible, homogeneous Markov chain, that is, a covariance-stationary stochastic process with

$$\text{Var}[\bar{\mathcal{A}}_N] = \frac{1}{N}\left[\gamma_{\mathcal{A}}(0) + 2\sum_{n=1}^{N-1}\left(1 - \frac{n}{N}\right)\gamma_{\mathcal{A}}(n)\right] \tag{4.12}$$

where $\gamma_{\mathcal{A}}(n) \equiv \langle \mathcal{A}_0 \mathcal{A}_n \rangle - \langle \mathcal{A} \rangle^2$ is the autocovariance function of the observable. Introducing the autocorrelation function $\rho_{\mathcal{A}}(n) \equiv \gamma_{\mathcal{A}}(n)/\gamma_{\mathcal{A}}(0)$, we have

$$\tau_{\mathcal{A},N} \equiv N\frac{\text{Var}[\bar{\mathcal{A}}_N]}{\text{Var}[\mathcal{A}]} = 1 + 2\sum_{n=1}^{N-1}\left(1 - \frac{n}{N}\right)\rho_{\mathcal{A}}(n). \tag{4.13}$$

$\tau_{\mathcal{A},N}$ is the correct statistical measure of the autocorrelation error in the finite time-series. (Note that $\rho_{\mathcal{A}}(n) \ge 0$ in a stationary ergodic Markov chain[86].) For $N \to \infty$,

the Cesàro sum in eq. (4.13) reduces to a normal sum, and $\tau_{A,N}$ becomes the exact integrated autocorrelation time, $\tau_A = \lim_{N\to\infty} \tau_{A,N}$. For finite $N \gg 1$ (and $N \gg \tau_A$), one has the good approximation $\tau_A = \tau_{A,N} + \mathcal{O}(1/N)$.

We have used these formulas together with the well-known "blocking" method[87] to cross-check our estimates for $\text{Var}[\bar{A}_N]$ to calculate the true variances and autocorrelation times in our QMC simulation with a precision ("error of error") better than 2%. Both of our algorithms eliminate critical slowing down, and have $\tau_A \leq 2$ for all single loop-cluster improved estimators, independent of temperature, lattice size, and spin magnitude.

4.4 Comparison with Other Approaches

Figure 4-7 compares the $S = 1$ and 5/2 QMC ξ/a data from Figure 4-1 with experimental measurements, high-temperature series expansion[26] (HTE), and the semiclassical "pure-quantum self-consistent harmonic approximation" (PQSCHA)[37]. The experimental data is from neutron scattering[34, 36] on La_2NiO_4 ($S = 1$, $\xi/a \approx 2-30$) and Rb_2MnF_4 ($S = 5/2$, $\xi/a \approx 2 - 100$).

For both spins there exist intermediate regimes between moderate $\xi/a \sim 100$, where CH_3N_2B starts to deviate, and $\xi/a \approx 10$ where HTE starts to fail. These regimes are $4 \lesssim \xi/a \lesssim 100$ ($0.10 \lesssim t \lesssim 0.15$) for $S = 1$, and $12 \lesssim \xi/a \lesssim 500$ ($0.10 \lesssim t \lesssim 0.15$) for $S = 5/2$. Most of the experimental data fall into these "gaps". At least for large spin $S = 5/2$, this intermediate regime is correctly described by PQSCHA. (For $S = 1$, PQSCHA is less satisfying but still catches the correct order.) The diverse approaches collectively describe the $S > 1/2$ correlation length from extremely small to extremely large values. Our QMC data connects the regimes where the diverse approaches are valid. They are seen to be complementary, and are thereby reconciled.
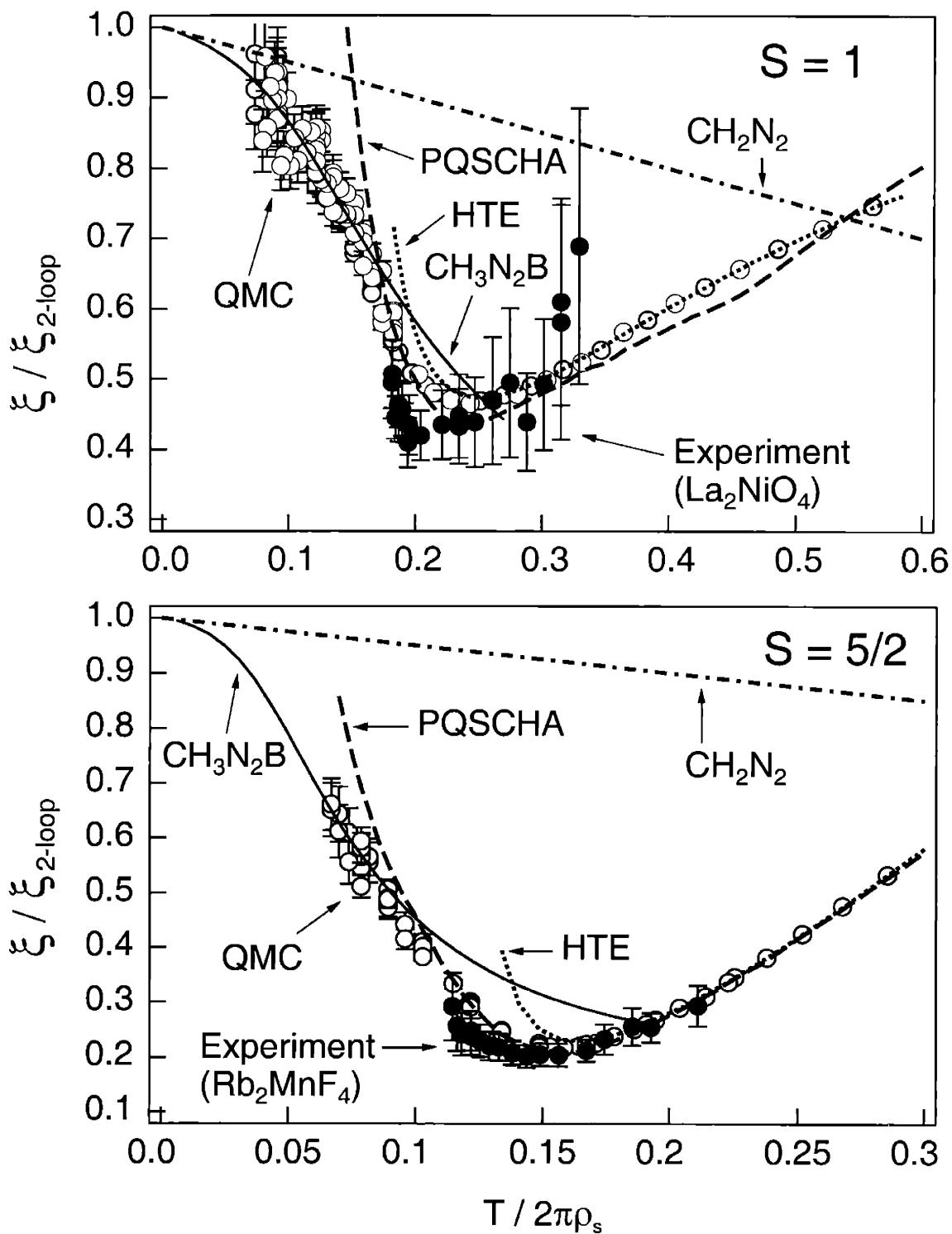
Figure 4-7: Memphis chart for $S = 1$ and $5/2$. The QMC data (open circles) connect the regimes where the various methods apply: CH_3N_2B (solid line); PQSCHA (dashed line); high-temperature expansion (dotted line); and experiment (solid circles).

Chapter 5

Unified Models for Superconductors

Understanding QCD at non-zero baryon chemical potential μ is very important in the context of both heavy ion and neutron star physics. While asymptotically large values of μ are accessible in perturbative QCD calculations, such values are not realized in actual physical systems. Investigations of the phenomenologically relevant regime at intermediate μ require the use of nonperturbative methods. Unfortunately, first-principles lattice calculations in this regime are presently prevented by the notorious complex action problem. Conjectures for the QCD phase diagram at non-zero μ are thus based on model calculations. These calculations reveal interesting phenomena such as color superconductivity [88, 89, 90] but one cannot expect the results to be quantitatively correct.

While it is very important to develop quantitative methods to understand QCD at non-zero μ, the purpose of this project is to gain further insight through analogies with related condensed matter systems. In particular, the phase diagram of high-temperature cuprate superconductors is qualitatively similar to the one conjectured for two flavor QCD. The ordinary hadronic phase of QCD at small μ in which the chiral $SO(4) = SU(2)_L \otimes SU(2)_R$ symmetry is spontaneously broken down to $SO(3) = SU(2)_{L=R}$ corresponds to the antiferromagnetic Néel phase of the undoped cuprates in which the $SO(3)_s$ spin rotational symmetry is broken down to $SO(2)_s$ due

to the spontaneous generation of a staggered magnetization. The high-temperature superconducting phase of the doped cuprates with spontaneous $U(1)_{em}$ breaking corresponds to the color superconducting phase of two flavor QCD in which the $SU(3)_c$ gauge symmetry is expected to break down to $SU(2)_c$. Finally, the quark-gluon plasma corresponds to the high-temperature metallic phase of the cuprates.

5.1 Background: The Antiferromagnet and High-Temperature Superconductors

QCD in the color superconducting phase is a genuine high-temperature superconductor. The mechanism that leads to quark Cooper pair binding is direct one-gluon exchange in the attractive color anti-triplet channel. This is in contrast to ordinary (low-temperature) superconductors in which the direct electron-electron Coulomb interaction (mediated by one-photon exchange) is repulsive. Ordinary superconductivity is due to an indirect phonon-mediated attraction which occurs at rather low energies and thus gives rise to small transition temperatures. The mechanism that leads to high-temperature superconductivity in the cuprates is presently not understood, but is expected to be due to processes that happen at a rather high energy scale unrelated to phonon exchange. Both in the cuprates and in QCD the phase transition that separates the phases of broken global and local symmetries is driven by a chemical potential (for electrons and quarks, respectively).

Furthermore, the solution of microscopic models for the cuprates (such as the Hubbard model) is prevented by a severe sign problem. Still, there are interesting attempts to understand superconductivity in the cuprates in analogy to simpler condensed matter systems. In particular, Zhang has conjectured that a transition that separates the antiferromagnetic Néel phase from the high-temperature superconducting phase is analogous to the spin flop transition of the staggered magnetization in a 3-d anisotropic antiferromagnet [15]. This transition is driven by an external uniform magnetic field B which plays the role of a chemical potential. Due to the anisotropy,

such an antiferromagnet has only a $\mathbb{Z}_2 \otimes SO(2)_s$ (not the full $SO(3)_s$) spin rotational symmetry. At small B, the staggered magnetization $\mathbf{n} = (n_1, n_2, n_3)$ points along the easy 3-axis, while at large B it flops into the 12-plane. The spin flop transition is illustrated in Fig. 5-1. The flop transition is a first order phase transition line that
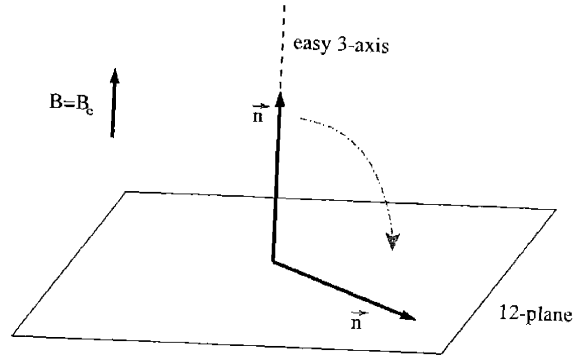
Figure 5-1: The spin flop transition of an anisotropic antiferromagnet in a magnetic field $\mathbf{B}$. For $B < B_c$ the staggered magnetization vector $\mathbf{n}$ points along the easy 3-axis, and for $B > B_c$ it flops into the 12-plane.

ends in a bicritical point from which two second order phase transition lines emerge — one in the 3-d Ising and one in the 3-d XY model universality class. At the bicritical point the $\mathbb{Z}_2 \otimes SO(2)_s$ symmetry is dynamically enhanced to $SO(3)_s$ [91].

Zhang has argued that a similar type of symmetry unification may occur for high-temperature superconductors [15]. He combined the 3-component staggered magnetization and the 2-component Cooper pair condensate to an $SO(5)$ "superspin" vector $\mathbf{n} = (n_1, n_2, n_3, n_4, n_5)$. In the $SO(5)$ theory the transition between the antiferromagnetic Néel phase and the high-temperature superconducting phase is a first order superspin flop transition. At small doping (small μ) the superspin lies in the $SO(3)_s/SO(2)_s = S^2$ easy sphere describing the staggered magnetization vector. At larger μ the superspin flops into the $U(1)_{em} = S^1$ plane now describing the Cooper pair condensate. The superspin flop transition is expected to end in a bicritical point from which two second order lines emerge — one in the 3-d Heisenberg and one in the 3-d XY universality class. Zhang has argued that the bicritical point has a dynamically enhanced $SO(5)$ symmetry although the microscopic Hamiltonian is only

$SO(3)_s \otimes U(1)_{em}$ invariant. The expected phase diagram of an $SO(N) \otimes SO(M)$ invariant theory with potential dynamical symmetry enhancement to $SO(N + M)$ is shown in Fig. 5-2. For the cuprates $N = 2$ and $M = 3$, while for anisotropic anti-ferromagnets $N = 2$ and $M = 1$. As we will see next, for QCD $N = 6$ and $M = 4$.
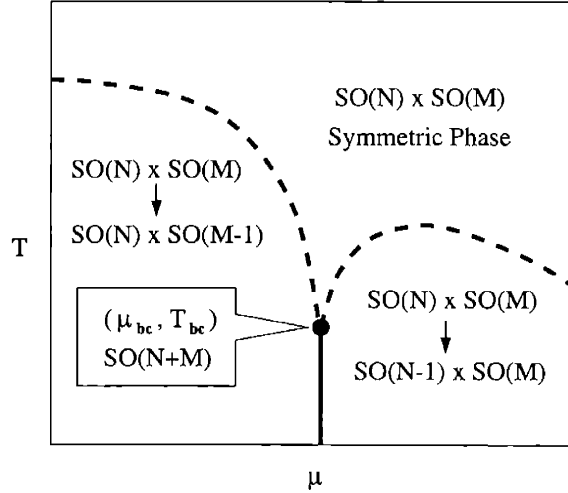
Figure 5-2: Expected phase diagram of an $SO(N) \otimes SO(M)$ invariant theory with potential dynamical symmetry enhancement to $SO(N + M)$. The first order flop transition (solid) line ends in a bicritical point (T_{bc}, μ_{bc}). Two second order (dashed) lines emerge vertically from this point.

5.2 Unifying Color Superconductivity and Chiral Symmetry Breaking

Recently, Chandrasekharan and Wiese[92] have generalized the $SO(5)$ unified theory of high-temperature superconductivity and antiferromagnetism to an $SO(10)$ unified description of color superconductivity and chiral symmetry breaking in QCD. Although the unifying group is the same as in a grand unified theory, the unification scale would now be around 10 MeV. They considered left and right-handed quark fields $\Psi_L^{f,c}$ and $\Psi_R^{f,c}$ with two flavors $f = 1, 2$ and three colors $c = 1, 2, 3$. The chiral

symmetry breaking order parameter

$$(\bar{\Psi}\Psi)^{fg} = \sum_c \bar{\Psi}_L^{f,c}\Psi_R^{g,c} \tag{5.1}$$

is a color singlet, $SU(2)_L$ and $SU(2)_R$ doublet, with baryon number zero. The color symmetry breaking order parameter

$$(\Psi\Psi)^c = \sum_{f,g,a,b} \epsilon_{fg}\epsilon_{abc}(\Psi_{L,R}^{f,a})^T C \Psi_{L,R}^{g,b}, \tag{5.2}$$

on the other hand, is a color anti-triplet, $SU(2)_L \otimes SU(2)_R$ singlet, with baryon number 2/3. Similarly, $(\bar{\Psi}\bar{\Psi})^c$ is a color triplet, $SU(2)_L \otimes SU(2)_R$ singlet, with baryon number $-2/3$. The group $SO(10)$ contains $SU(3)_c \otimes SU(2)_L \otimes SU(2)_R \otimes U(1)_B$ as a subgroup. The 10-dimensional vector representation of $SO(10)$ decomposes into

$$\{10\} = \{1,2,2\}_0 \oplus \{\bar{3},1,1\}_{2/3} \oplus \{3,1,1\}_{-2/3}, \tag{5.3}$$

and thus naturally combines the order parameters for chiral symmetry breaking and color superconductivity to a 10-component "supervector" $\mathbf{n} = (n^1, n^2, ..., n^{10})$ with

$$n^c = (\Psi\Psi)^c + (\bar{\Psi}\bar{\Psi})^c,$$
$$n^{c+3} = -i[(\Psi\Psi)^c - (\bar{\Psi}\bar{\Psi})^c], \ c \in \{1,2,3\},$$
$$n^7 = (\bar{\Psi}\Psi)^{11} + (\bar{\Psi}\Psi)^{22},$$
$$n^8 = -i[(\bar{\Psi}\Psi)^{12} + (\bar{\Psi}\Psi)^{21}],$$
$$n^9 = (\bar{\Psi}\Psi)^{12} - (\bar{\Psi}\Psi)^{21},$$
$$n^{10} = -i[(\bar{\Psi}\Psi)^{11} - (\bar{\Psi}\Psi)^{22}]. \tag{5.4}$$

In the chirally broken phase at small μ the 4-component vector (n^7, n^8, n^9, n^{10}) develops an expectation value, thus breaking $SU(2)_L \otimes SU(2)_R$ spontaneously to $SU(2)_{L=R}$. The corresponding Goldstone pions are described by fields in the easy 3-sphere $SU(2)_L \otimes SU(2)_R/SU(2)_{L=R} = S^3$. In the color superconducting phase at larger μ, on the

other hand, the 6-component vector $(n^1, n^2, ..., n^6)$ gets an expectation value and the supervector flops into the 5-sphere $SU(3)_c/SU(2)_c = S^5$ that describes the quark Cooper pair condensate. In this case, one would expect that the first order supervector flop line ends at a bicritical point with dynamical symmetry enhancement to $SO(10)$. However, a renormalization group flow analysis shows that both the $SO(5)$ and $SO(10)$ fixed point are unstable, at least in $(4 - \epsilon)$ dimensions [92]. The purpose of this project is to simulate these systems in three dimensions in order to map out their phase diagram. This is a necessary first step in investigating the detailed nature of the phase transitions to see whether the perturbative results obtained in $(4 - \epsilon)$ dimensions hold when $\epsilon = 1$.
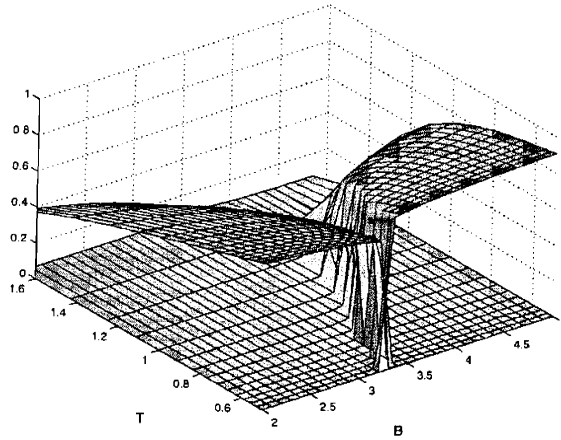
Figure 5-3: Flop transition in an anisotropic antiferromagnet. The two wings correspond to the square of the staggered magnetization n_3^2 along the 3-axis and $n_1^2 + n_2^2$ in the 12-plane.

To illustrate the dynamics of the flop transition, we now construct a unified low-energy effective Lagrangian for the Goldstone modes described by a P $(= N + M)$-component unit vector $\mathbf{n}$. In the absence of $SO(N + M)$ symmetry breaking terms (other than the chemical potential), the low-energy effective action takes the form

$$
\begin{aligned}
S[\mathbf{n}] &= \int_0^{1/T} dt \int d^3x \, \frac{F^2}{2} [\partial_i n^\alpha \partial_i n^\alpha \\
&+ \frac{1}{c^2} (\partial_0 n^\alpha + A_0^{\alpha\beta} n^\beta)(\partial_0 n^\alpha + A_0^{\alpha\beta} n^\beta)].
\end{aligned}
\tag{5.5}
$$

71

The chemical potential μ couples as an imaginary non-Abelian constant vector potential

$$A_0^{\alpha\beta} = i\mu \sum_{c=1,\dots,N/2} \left(\delta^{\alpha,c} \delta^{c+N/2,\beta} - \delta^{\alpha,c+N/2} \delta^{c,\beta} \right) \tag{5.6}$$

in the Euclidean time direction. To account for explicit $SO(N + M)$ breaking to $SO(N) \otimes SO(M)$ we add a potential term $-V_0[(n^{N+1})^2 + \dots + (n^{N+M})^2]$ to the action that favors the easy $(M-1)$-sphere. In the case of QCD this leads to chiral symmetry breaking. The total potential for constant fields $\mathbf{n}$ then takes the form

$$
\begin{aligned}
V(\mathbf{n}) &= -\frac{F^2}{2c^2}\mu^2[(n^1)^2 + \dots + (n^N)^2] \\
&\quad - V_0[(n^{N+1})^2 + \dots + (n^{N+M})^2].
\end{aligned} \tag{5.7}
$$

For $\mu < \mu_c = \sqrt{2V_0 c^2/F^2}$, it is energetically favorable for the supervector to lie in the easy $(M-1)$-sphere. For $\mu > \mu_c$, on the other hand, the supervector $\mathbf{n}$ flops into the $(N-1)$-sphere. In QCD, this induces a first order phase transition from the chirally broken to the color superconducting phase.

It is interesting to ask if the supervector can play a dynamical role in the real world. In particular, with the strange quark present, a new color superconducting phase with color-flavor locking arises [93]. This phase may be analytically connected to the ordinary hadronic phase [94, 95]. Then there would be no supervector flop transition. However, when the strange quark is sufficiently heavy, a flop transition may exist.

5.3 The Model

In order to explore the phase diagrams (that is, the symmetry-breaking patterns) of all three models— the antiferromagnet, the high-T_c superconductor, and the color superconductor, we employed a simple classical Hamiltonian containing the relevant symmetries. While such a generic Hamiltonian may be written "from scratch," it can also be obtained from the effective action, eq. (5.5). Near the critical points, which

form the region of interest to us, the correlation length becomes large ($\xi \gg 1/T$) and the system dimensionally reduces. The fields are then essentially constant in the Euclidean time direction, so the time derivatives $\partial_0 n^\alpha$ vanish. The spatial derivatives are replaced by their lattice approximations

$$(\partial_i n^\alpha)(\partial_i n^\alpha) \rightarrow \left(\frac{n_i^\alpha - n_{i-1}^\alpha}{a}\right)\left(\frac{n_i^\alpha - n_{i-1}^\alpha}{a}\right) = \frac{2}{a}\left[1 - n_{i-1}^\alpha n_i^\alpha\right],$$

so that the kinetic term becomes the nearest-neighbor interaction on the lattice (a is the lattice spacing, as always). Generalizing the coefficient of the kinetic term to differ for the first M and the last N components, one arrives at the Hamiltonian for the $SO(M) \otimes SO(N)$ model,

$$\beta H = \beta \left\{ \sum_{<xy>} \left[g_M \mathbf{n}_x^{(M)} \cdot \mathbf{n}_y^{(M)} + g_N \mathbf{n}_x^{(N)} \cdot \mathbf{n}_y^{(N)}\right] + \mu \sum_x |\mathbf{n}_x^{(M)}|^2 \right\}$$

which can be recast in terms of three independent parameters (β', g', μ') as

$$\beta H = \beta' \left\{ -\sum_{<xy>} \left[\mathbf{n}_x \cdot \mathbf{n}_y + (g'-1)\mathbf{n}_x^{(N)} \cdot \mathbf{n}_y^{(N)}\right] + \mu' \sum_x |\mathbf{n}_x^{(M)}|^2 \right\}. \tag{5.8}$$

Note that for $g' \neq 1$, the Hamiltonian is explicitly *not* $SO(M+N)$-symmetric for any combination of β' and μ'. An $SO(M+N)$ symmetry, if present, must necessarily be generated dynamically.

Chapter 6

Simulating the $SO(M) \otimes SO(N)$ Model

To perform the numerical simulations, we used a combination of three algorithms which jointly provide for ergodicity and detailed balance. The **Wolff algorithm** is a classical cluster algorithm that efficiently rotates the spin vectors in $\mathbb{R}^{M+N}$, but does not alter the relative length of the two sub-radii. The modified **microcanonical overrelaxation** algorithm can sample different distributions of the sub-radii, but it does not quite satisfy ergodicity. Thus, we also employ a **Metropolis step** to assure that we sample the entire radius distribution.

6.1 Wolff Algorithm

The Wolff algorithm is a cluster algorithm; as in the quantum AFHM, it proceeds by creating bonds between lattice sites to form a cluster, and then updating the entire cluster at once. To understand the Wolff algorithm, consider first the Ising model,

$$\beta H_{\text{Ising}} = -\beta \sum_{<xy>} s_x s_y, \tag{6.1}$$

where the $s_x = \pm 1$ are Ising spins. The rule for creating a bond on a link between two neighboring spins is then the following:

- **Parallel spins:** The weight of this configuration is e^{β}. Create a bond between these two spins with probability $1 - e^{-2\beta}$

- **Antiparallel spins:** The weight of this configuration is $e^{-\beta}$. Never create a bond between these two spins.

This rule then satisfies detailed balance locally, since

$$
\begin{aligned}
W(\mathcal{C}) \cdot p(\mathcal{C}{\to}\mathcal{C}') &= W(\mathcal{C}') \cdot p(\mathcal{C}'{\to}\mathcal{C}) \\
e^{\beta} \cdot e^{-2\beta} &= e^{-\beta} \cdot 1
\end{aligned}
$$

How does the Wolff algorithm generalize to multi-component spin systems? For the moment, let us consider only an $SO(M)$ model such as

$$
\beta H_{\mathrm{M}} = -\beta \sum_{<xy>} \mathbf{n}_x \cdot \mathbf{n}_y, \tag{6.2}
$$
$$
\mathbf{n}_x \in \mathbb{R}^M, \mathbf{n}_x^2 = 1
$$

The algorithm proceeds by choosing a unit vector $\mathbf{w}$ in $\mathbb{R}^M$. This vector specifies the plane about which we will "flip" the spins in the cluster (this would the analogue of the horizontal plane in the Ising model). Then the interaction between the spins at x and at y can be written as

$$
\begin{aligned}
\beta \sum_{<xy>} \mathbf{n}_x \mathbf{n}_y &= -\beta \left[\mathbf{n}_{x\parallel} \cdot \mathbf{n}_{y\parallel} + \mathbf{n}_{x\perp} \cdot \mathbf{n}_{y\perp} \right], \\
&= \underbrace{-\beta_{\mathrm{eff}} s_x s_y}_{\text{Ising}} -\beta \mathbf{n}_{x\perp} \cdot \mathbf{n}_{y\perp} \tag{6.3} \\
s_x &= \mathrm{sgn}(\mathbf{n}_x \cdot \mathbf{w}) \\
\mathbf{n}_{x\parallel} &= (\mathbf{n}_x \cdot \mathbf{w})\,\mathbf{w}, \\
\mathbf{n}_{x\perp} &= \mathbf{n}_x - \mathbf{n}_{x\parallel}, \\
\beta_{\mathrm{eff}} &= \left(\beta |\mathbf{n}_{x\parallel}| |\mathbf{n}_{y\parallel}| \right)
\end{aligned}
$$

This decomposition maps the "parallel" part of the problem onto the Ising formulation. The variables s_x and s_y in eq. (6.3) are Ising spins now, just as in eq. (6.1), with

coupling β_{eff}. The breakup probability when the two signs are alike is then $1 - e^{-2\beta_{\text{eff}}}$. Flipping a cluster once again means reversing the sign of these Ising variables, which involves taking s_x to $-s_x$. In terms of the full vector,

$$\mathbf{n}_x \rightarrow \mathbf{n}'_x = \mathbf{n}_x - 2\left(\mathbf{w} \cdot \mathbf{n}_x\right)\mathbf{w}$$

It should be clear that as long as we choose $\mathbf{w}$ randomly in S^{M-1}, these rules will satisfy ergodicity and detailed balance. Note that the "perpendicular" part of the action is not affected. This rule is illustrated in Fig. 6-1.
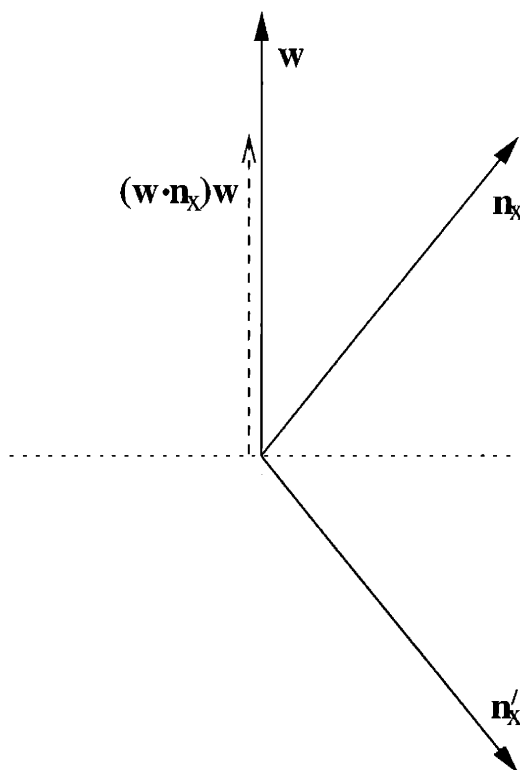
Figure 6-1: Spin update under the Wolff algorithm. The spin $\mathbf{n}$ is reflected upon the plane normal to the Wolff vector $\mathbf{w}$.

For our full model, eq. (5.8), we apply the Wolff algorithm to the $\mathbb{R}^M$ and $\mathbb{R}^N$ parts of the Hamiltonian separately. At each simulation step on the lattice, then, we are again updating the components of the spin parallel to the chosen Wolff vector $\mathbf{w}$. The probability to create a bond involves β_{eff}, and that is where detailed balance

76

is invoked. The "perpendicular" part of the action in both the $\mathbb{R}^M$ and $\mathbb{R}^N$ spaces, as well as the the chemical potential term, are unchanged, and hence need not be considered. Note, however, that the chemical potential term is irrelevant precisely because the length of the radii in the two subspaces is unchanged. The Wolff algorithm thus provides for ergodicity with respect to $SO(M)$ and $SO(N)$ rotations, but not with respect to shifting the radii from one subspace to another (i.e. $SO(M+N)$ rotations). That is why further algorithms are needed to assure complete ergodicity.

6.2   Modified Microcanonical Overrelaxation

Microcanonical overrelaxation[96, 97] algorithms generate new configurations while maintaining the value of the action. In the present context, a modified version is used to shift the relative radii among the two subspaces. In a pure $SO(P)$ model, such an algorithm generates a new configuration with the same action, and hence requires no probabilistic choice. This also holds true for the $SO(M) \otimes SO(N)$ model at $\mu = 0$. A non-zero chemical potential, however, requires an additional Monte Carlo step to ensure that detailed balance is obeyed (that is why this is a "modified" overrelaxation algorithm). Furthermore, this algorithm does not quite satisfy ergodicity.

The idea behind microcanonical overrelaxation is simple: it reflects each spin around the sum of its nearest neighbors. At each lattice update step, the algorithm visits each site x in turn and computes the vector sum σ_x of the nearest neighbors:

$$\sigma^i = \sum_{<y>_x} g_i n_y^i \tag{6.4}$$

$$g_i = \begin{cases} 1 & \text{if } 1 \leq i \leq M \\ g' & \text{if } M < i \leq P \end{cases}$$

where the notation $< y >_x$ denotes all the nearest neighbor sites y of x. The update consists of reflecting $\mathbf{n}_x$ about σ_x,

$$\mathbf{n}_x \rightarrow \mathbf{n}_x' = 2 \left(\sigma_x \cdot \mathbf{n}_x \right) \sigma_x - \mathbf{n}_x. \tag{6.5}$$

It is straightforward to verify that this transformation preserves the norm of n_x, as well as the nearest neighbor dot-product $\sigma_x \cdot \mathbf{n}_x$. This latter dot product comprises the $\mu = 0$ part of the $SO(M) \otimes SO(N)$ Hamiltonian,

$$\sum_x \sigma_x \cdot \mathbf{n}_x,$$

so that any change in the Boltzmann weight due to this algorithm must necessarily appear in the $\mu' \sum_x |\mathbf{n}_x^{(M)}|^2$ term. To enforce detailed balance with non-vanishing μ', the simulations then apply a Metropolis decision, eq. (3.8), to the chemical potential part of the Hamiltonian alone.
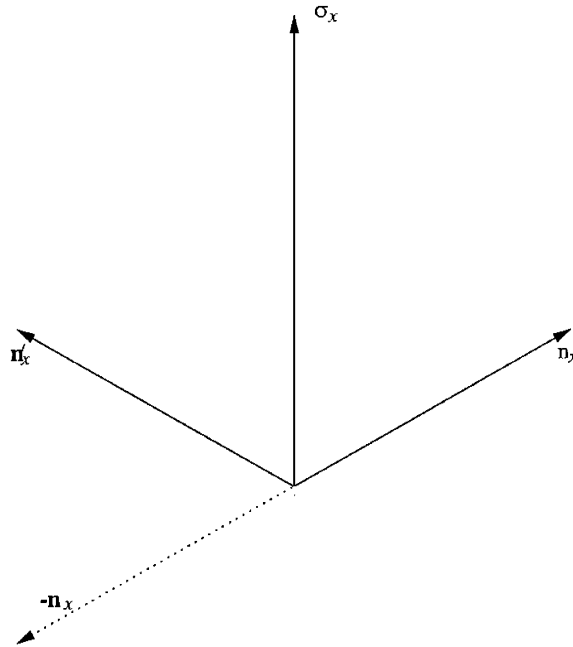
Figure 6-2: The modified microcanonical overrelaxation algorithm. The lattice spin $\mathbf{n}_x$ is reflected about the sum σ_x of its nearest neighbors.

While this algorithm promises to be relatively efficient (in that we may expect large acceptance rate for small enough μ', and indeed, total acceptance when $\mu' = 0$), it does not satisfy ergodicity. For example, if all the spins in the lattice are oriented entirely in one subspace and not the other, no sequence of microcanonical overrelaxation steps will take any spin into the other subspace (and conversely, if the spins have non-zero

projections onto both subspaces, the lattice cannot reach a configuration where only one subspace is occupied). Clearly, yet a third algorithm is needed to ensure that all configurations are reachable.

6.3 Radius Metropolis

The most obvious way to ensure that we indeed sample all the possible unit vectors in $\mathbb{R}^{M+N}$, where the superspin lives, is to choose a randomly oriented point in S^{M+N-1}, and then accept or reject using the usual Metropolis criterion. This mechanism would indeed update both the angle and the radius of the subspins. Combined with the preceding two algorithms, it would ensure ergodicity, but that need not mean that it would be easy to implement favorable large-scale changes in the lattice. Indeed, as was argued previously, it could potentially be inefficient in the neighborhood of critical phenomena.

Since we already have an efficient algorithm that updates the angles in $\mathbb{R}^M$ and $\mathbb{R}^N$ separately, and a presumably-efficient algorithm that updates both the angles and (in most cases) the radii, we decided to use a different algorithm that merely reweighs the radius lengths in the two subspaces but does not change the angle of the spins in each of the two subspaces. Part of the rationale for doing this is to isolate the radial and angular contributions to the various parts of the actions, rather than having changes to both occur at the same time. Qualitatively, it seems more likely that a configuration be accepted in which the angle between the spins in $\mathbb{R}^M$, say, is kept the same though the length changes, than one in which a, say, ferromagnetic spin-spin coupling becomes antiferromagnetic because both angle and length were changed.

To derive the distribution of radius lengths in the two subspaces, one evaluates the integral

$$\int (d^P r)\delta(r - R) = R^{P-1} \int d\Omega_{P-1} = R^{P-1}\Omega_{P-1}.$$

Considering $\mathbf{r}$ in the expression on the left as being given by $\mathbf{r} = (\mathbf{a}, \mathbf{b})$, $\mathbf{a} \in \mathbb{R}^M$,

$\mathbf{b} \in \mathbb{R}^N$, one obtains

$$
\begin{aligned}
\int (d^P r)\delta(r - R) &= \int (d^M a)(d^N b)\delta(r - R) \\
&= \left(\int d\Omega_{M-1} \right) \left(\int d\Omega_{N-1} \right) \\
&\quad \cdot \int_0^\infty a^{M-1} da \int_0^\infty b^{N-1} db\, \delta\!\left(b - \sqrt{R^2 - a^2} \right) \frac{R}{\sqrt{(R^2 - a^2)}} \\
&= \left(\int d\Omega_{M-1} \right) \left(\int d\Omega_{N-1} \right) \int_0^R a^{M-1} da\, R \left(R^2 - a^2 \right)^{\frac{N}{2} - 1},
\end{aligned}
$$

where, in the second step, the expression at the end is the Jacobian factor arising from the change of arguments in the delta function. In this derivation, $a = |\mathbf{a}|$ is the radius in $\mathbb{R}^M$, whose distribution we wish to obtain. Setting $R = 1$, the integral becomes

$$
\underbrace{\int d\Omega_{M+N-1}}_{S^{M+N-1}} = \underbrace{\left(\int d\Omega_{M-1} \right)}_{S^{M-1}} \underbrace{\left(\int d\Omega_{N-1} \right)}_{S^{N-1}} \underbrace{\int_0^1 a^{M-1} da \left(1 - a^2 \right)^{\frac{N}{2} - 1}}_{\text{(radius distribution)}}.
$$

The last integrand, the beta integrand, is the desired radius distribution function. Once normalized to unity, it can be used as the probability density function (PDF) from which the radius vectors may be drawn. Expressed in terms of the squared $\mathbb{R}^M$ radius a^2, this PDF becomes

$$
F_{M,N}(a^2)\, d(a^2) = \frac{\left(a^2 \right)^{\frac{M}{2} - 1} \left(1 - a^2 \right)^{\frac{N}{2} - 1}}{\beta \left(\frac{M}{2}, \frac{N}{2} \right)} d(a^2), \tag{6.6}
$$

where $\beta(m, n) = \frac{\Gamma(m)\Gamma(n)}{\Gamma(m+n)}$ is the beta function. Obviously, the distribution of b^2 in $\mathbb{R}^N$ has a completely analogous form. The distribution for the three systems of interest are shown in Fig. 6-3.

To implement this algorithm, the simulation generates a beta variate from the distribution in eq. (6.6), using the efficient scheme set forth in Ref. [98].
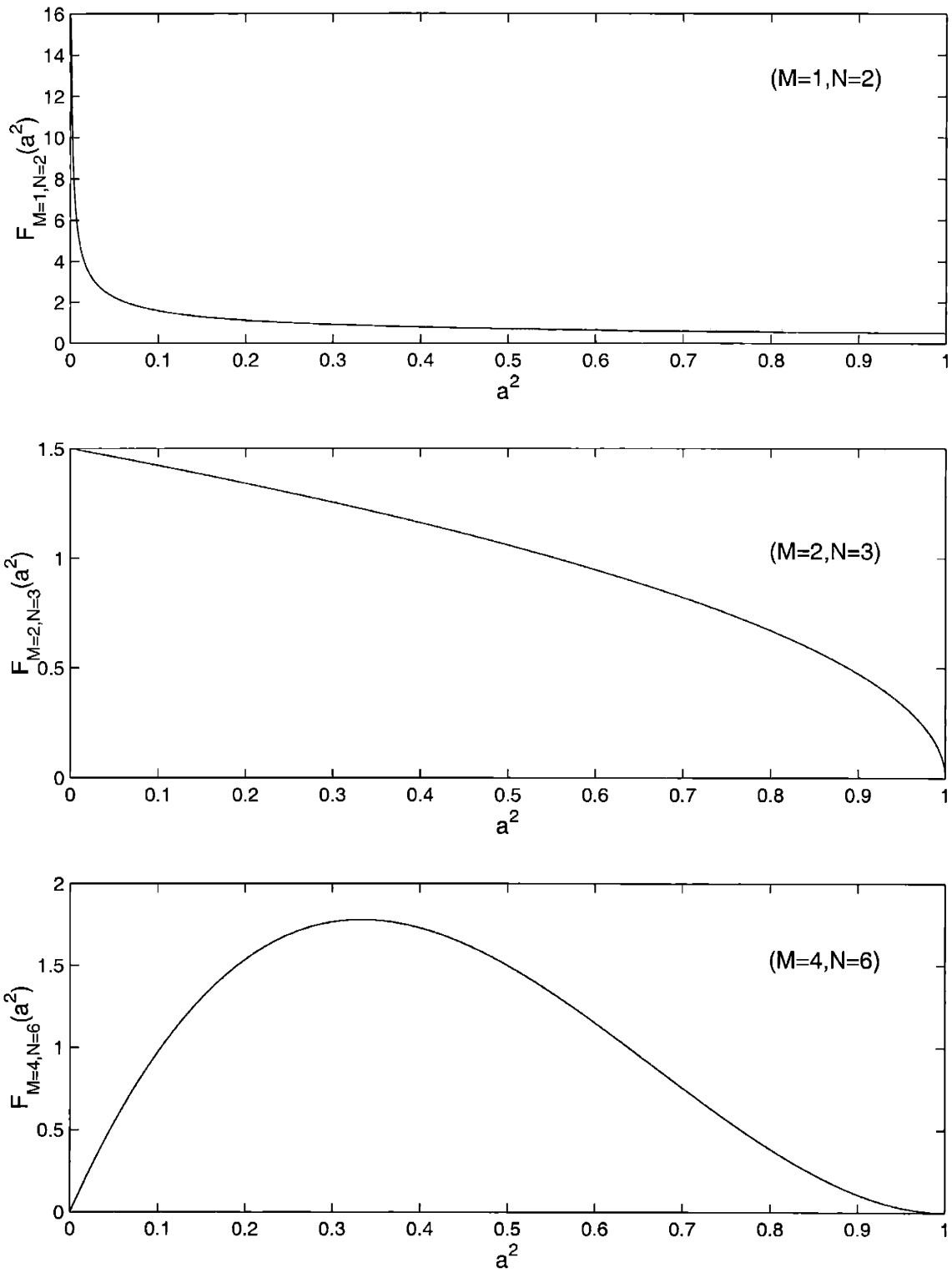
Figure 6-3: The subspace distribution in $\mathbb{R}^M$ of a unit vector uniformly distributed in $\mathbb{R}^{M+N}$, eq. (6.6). The top, middle, and bottom plots are for $(M, N) = (1, 2)$, $(2, 3)$, and $(4, 6)$, respectively.

Chapter 7

The Phase Diagram for the $SO(M) \otimes SO(N)$ Model

The algorithms described in the previous chapter were combined to simulate three systems, $SO(2) \otimes \mathbf{Z}_2$, $SO(2) \otimes SO(3)$, and $SO(4) \otimes SO(6)$. By studying a few order parameters, I was able to map the (finite size) phase diagrams for the three systems, and from there obtain estimates for the location of the bicritical points (Table 7). I discuss below the order parameters and how they were used to obtain the phase diagrams.

(M, N)	Lattice size L^d	est. β'_c	est. μ'_c
$(1, 2)$	20^3	$(3.8, 4.0)$	$(-8.8, -8.4)$
$(2, 3)$	20^3	$(0.700, 0.725)$	$(-7.4, -7.2)$
$(4, 6)$	10^3	$(1.40, 1.45)$	$(-7.0, -6.4)$

Table 7.1: Estimates for the location of the bicritical points in the three $SO(M) \otimes SO(N)$ systems. These estimates were obtained from the phase diagrams discussed in the text.

7.1   Order Parameters

In order to distinguish among the various phases, I looked at a few observables that highlight the various symmetries of the systems of size L^d ($d = 3$ in all these simula-

tions).

The **mean lengths** in each subspace should be a good measure of the flop transition between $\mathbb{R}^M$ and $\mathbb{R}^N$. Across the first order line, one of the lengths should increase suddenly at the expense of the other, while a smooth crossover should exist in the disordered phase. These quantities are defined by ($K = M$ or N)

$$R_K^2 \;=\; \left\langle \frac{1}{L^d} \sum_x \left(\mathbf{n}^{(K)}\right)^2 \right\rangle \tag{7.1}$$

Since each of the spins has unit length, the mean lengths satisfy

$$R_M^2 + R_N^2 = 1. \tag{7.2}$$

The **susceptibilities** are a signal of the $SO(M)$ or $SO(N)$ ordering that takes place on either side of the first order line. Because the flop transition is accompanied by $SO(K)$ ordering, each of the two ordered phases will exhibit an accompanying (staggered) magnetization; since the system is radially symmetric in these phases, the squares of the magnetizations (the susceptibilities) provide non-trivial thermal averages. In the disordered phase, the magnetizations should vanish. The susceptibilities are defined by

$$\chi_K \;=\; \left\langle \frac{1}{L^d} \left[\sum_x \mathbf{n}^{(K)} \right]^2 \right\rangle \tag{7.3}$$

The **mean dot product** is another measure of the ordering of the symmetric phases. In the disordered phase, the random orientation of the vectors should produce a vanishing mean dot product, whereas in the ordered phases the dot product should be non-trivial. The mean dot products are

$$D_K \;=\; \left\langle \frac{1}{dL^d} \sum_{<xy>} \mathbf{n}_x^{(K)} \cdot \mathbf{n}_y^{(K)} \right\rangle \tag{7.4}$$

The **internal energy** is particularly useful for observing two coexisting phases at

the first-order phase transition. The two phases have different internal energies, but it is the tug between the energy and the entropy factors that causes the system to jump discontinuously between the two phases. The internal energy, of course, is just the thermal average of the Hamiltonian and can be written

$$E = \left\langle \frac{1}{L^d} H \right\rangle \tag{7.5}$$

$$= \left\langle d \left(g_M D_M + g_N D_N \right) + \mu R_M^2 \right\rangle. \tag{7.6}$$

The **Binder cumulants** are moments of the internal energy which approach nontrivial (but L-dependent) values in the neighborhood of phase transitions[99, 100]. The fourth- and sixth-order cumulants are given by

$$B_4 = 1 - \langle H^4 \rangle / \left(3 \langle H^2 \rangle^2 \right) \tag{7.7}$$

$$B_6 = 1 - \langle H^4 \rangle / \left(2 \langle H^2 \rangle^2 \right) + \langle H^6 \rangle / \left(30 \langle H^2 \rangle^3 \right). \tag{7.8}$$

7.2 Results for the $SO(2) \otimes \mathbb{Z}_2$ System

I simulated the $SO(2) \otimes \mathbb{Z}_2$ system (corresponding to $M = 1, N = 2$) on a three-dimensional lattice of length $L = 20$ with an asymmetry parameter $g' = 3$. I alternated the three algorithms described in the previous chapter, and measured every fourth iteration to obtain a total of 10^5 measurements. In the following pages, I show (β', μ') plots of the order parameters, as well as the second moments of these quantities (except for B_4 and B_6). The second moments are of particular significance as they show a sharp signal near a first or second phase transition, since the spread of sampled values is higher there than well within a given phase. Strictly speaking, of course, the phase transitions occur only in the thermodynamic limit $L \to \infty$; what one observes in computer simulations are just the finite-size cross-over regions which correspond to the infinite-volume transitions. As L increases, the cross-over regions become narrower, and finer (β', μ') meshes are required in order to sample enough cross-over points to make the second-moment signals actually visible.

The mean lengths, R_M^2 and R_N^2, are shown in Fig. 7-1. The flop transitions onto $\mathbb{R}^M$ and $\mathbb{R}^N$ are clearly visible; much harder to see is the disordered phase, which appears as leaf with a slightly different slope. In the second moment plot, however, one sees not only the ridge corresponding to the flop transition, but also two ridges corresponding to the presumed second-order transitions in Fig. 5-2. This ridge does not appear in simulations on a smaller lattice with $L = 10$.

The susceptibilities (Figs. 7-2 and 7-3) and the dot products (Figs. 7-4 and 7-5) also show clearly each of the ordered phases. The D_N second moment plot shows only the slightest hint of a secondary ridge marking the disordered phase. The Binder cumulants (Fig. 7-6), on the other hand, show a very clear (albeit small, 1 part in 10^3) signal for the cross-overs corresponding to the presumed first- and second-order phase transitions.

The cross-over regions seen in each of those plots actually fall on top of each other. It is then possible to generate a rough phase diagram by mapping the ridges of B_4 and B_6 and of the second moments of R_K^2, χ_K and D_K. This leads to the finite-volume
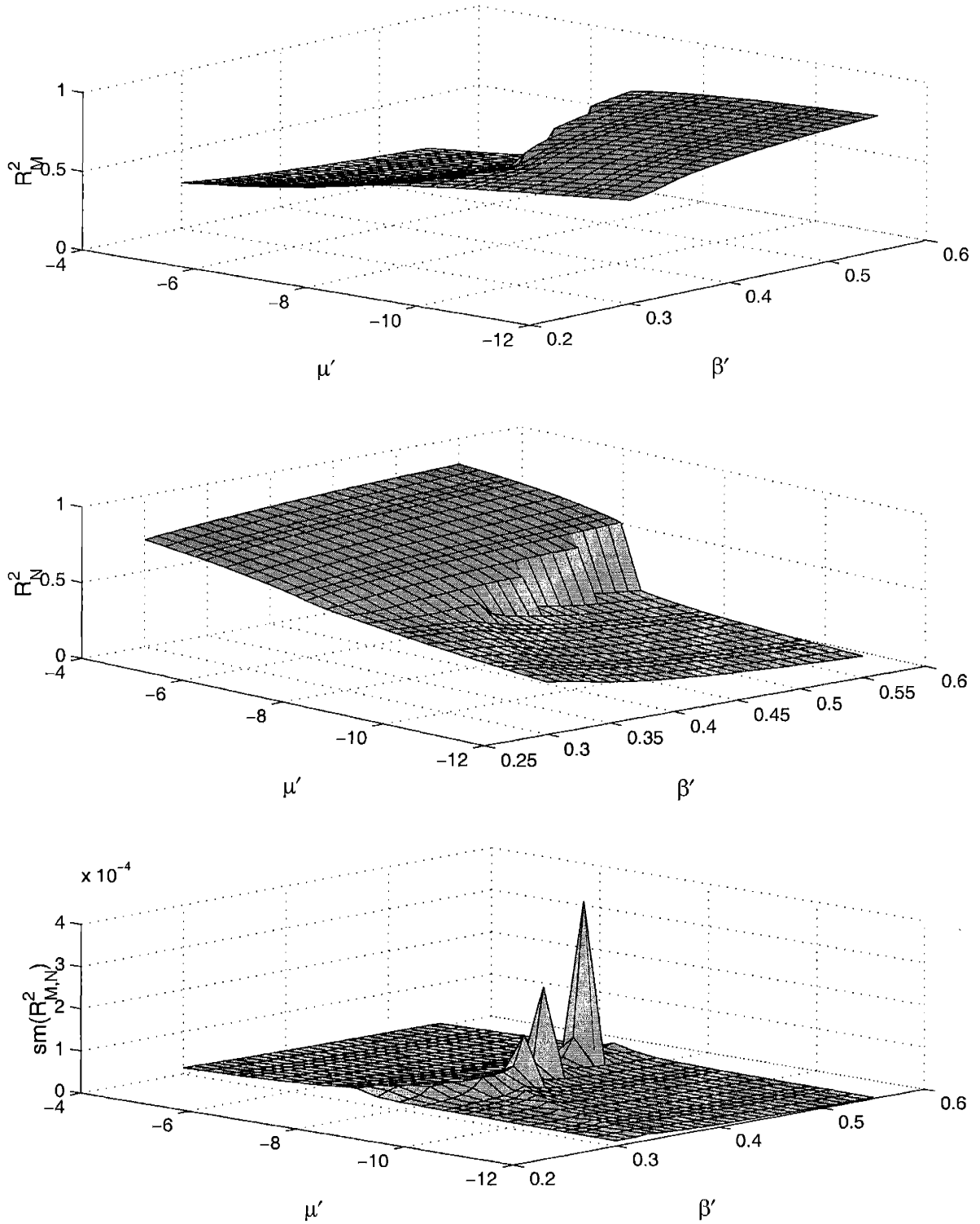
Figure 7-1: Mean lengths R_M^2 (top) and R_N^2 (middle), and their second moment (bottom) for the $SO(2) \otimes \mathbf{Z}_2$ system at $g' = 3$. Note that due to eq.7.2, the second moments of R_M^2 and R_N^2 are numerically identical.
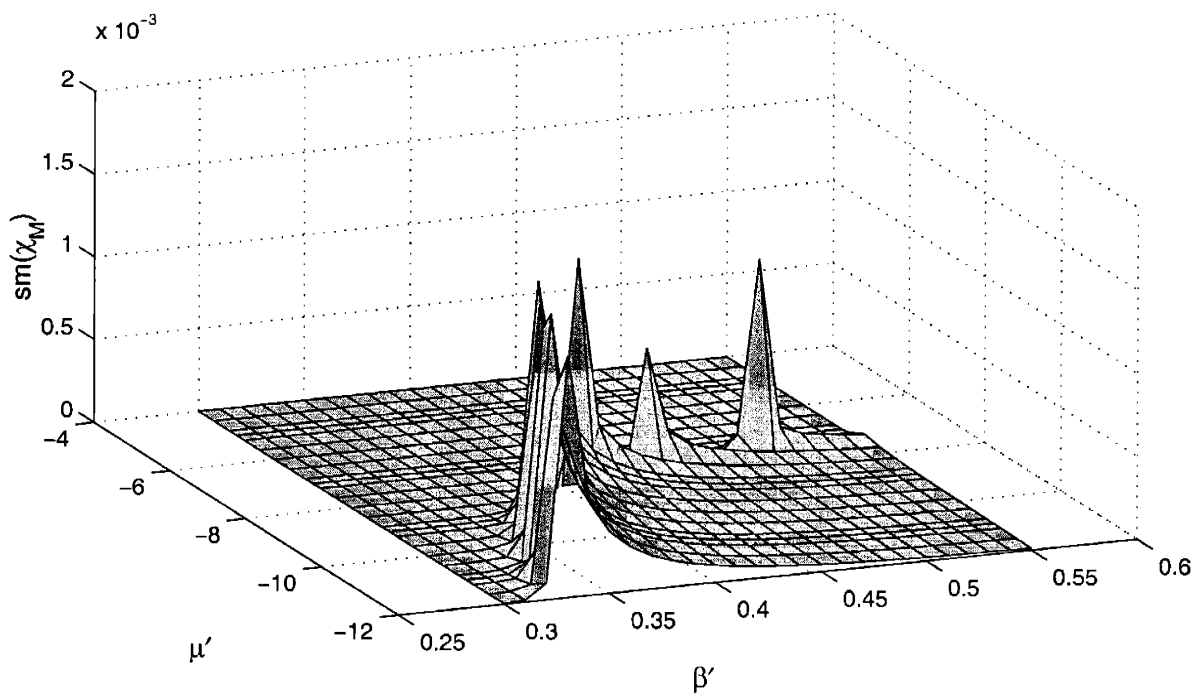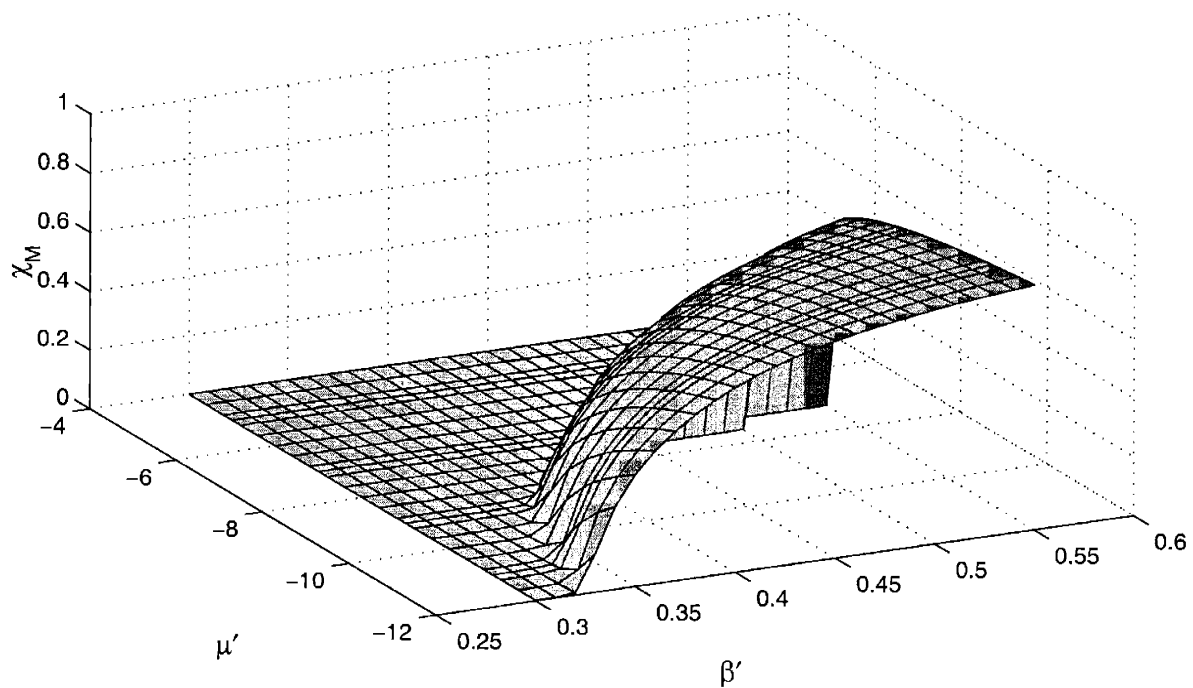
Figure 7-2: Susceptibility in $\mathbb{R}^M$ (top) and its second moment (bottom) for the $SO(2) \otimes \mathbf{Z}_2$ system at $g' = 3$. Note the clear distinction between the ordered and disordered phases.
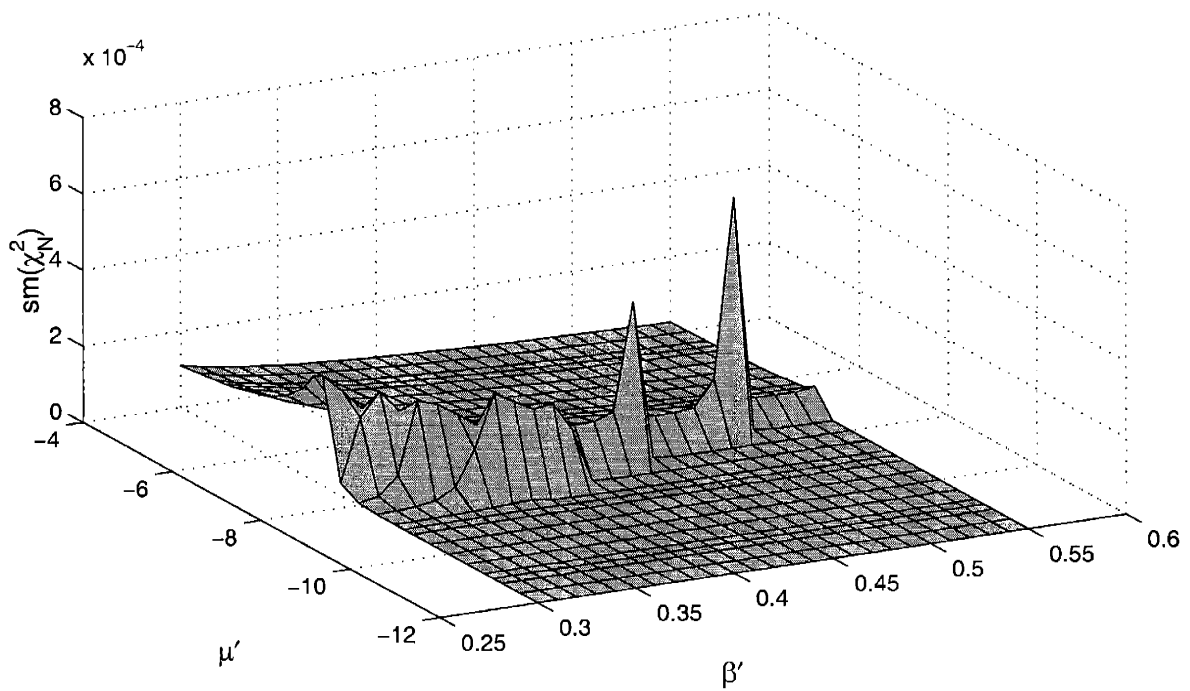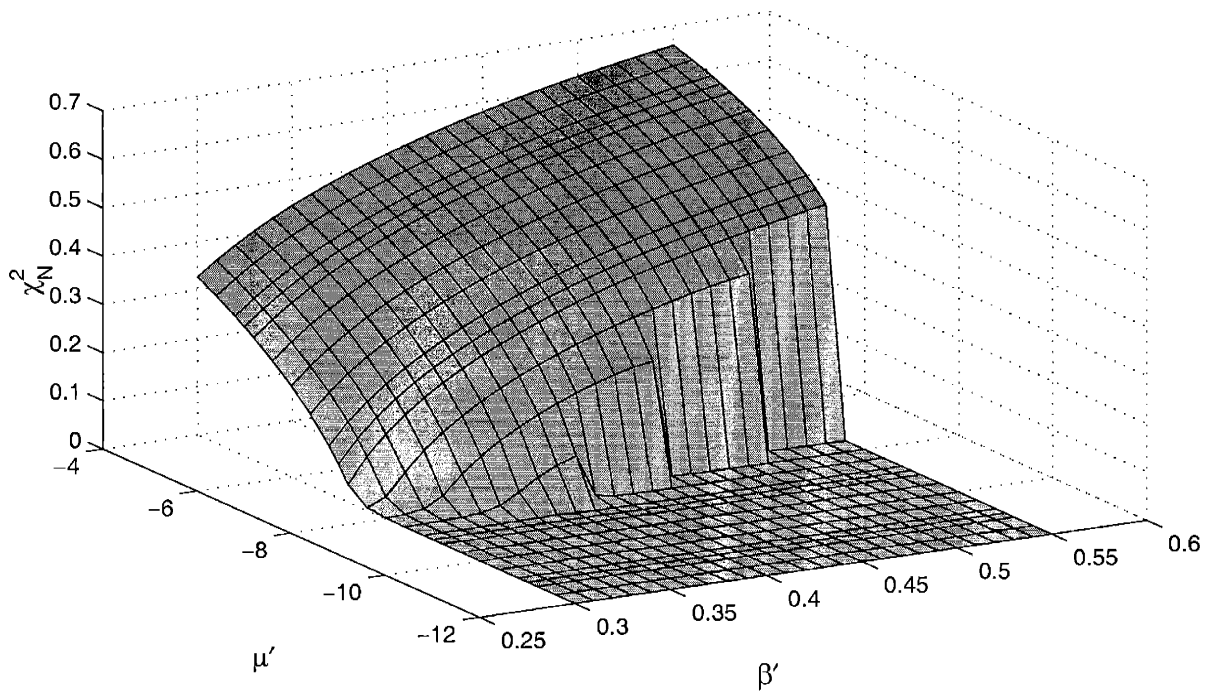
Figure 7-3: Susceptibility in $\mathbb{R}^N$ (top) and its second moment (bottom) for the $SO(2) \otimes \mathbf{Z}_2$ system at $g' = 3$. Here, too, the ordered and disordered phases are clearly visible.
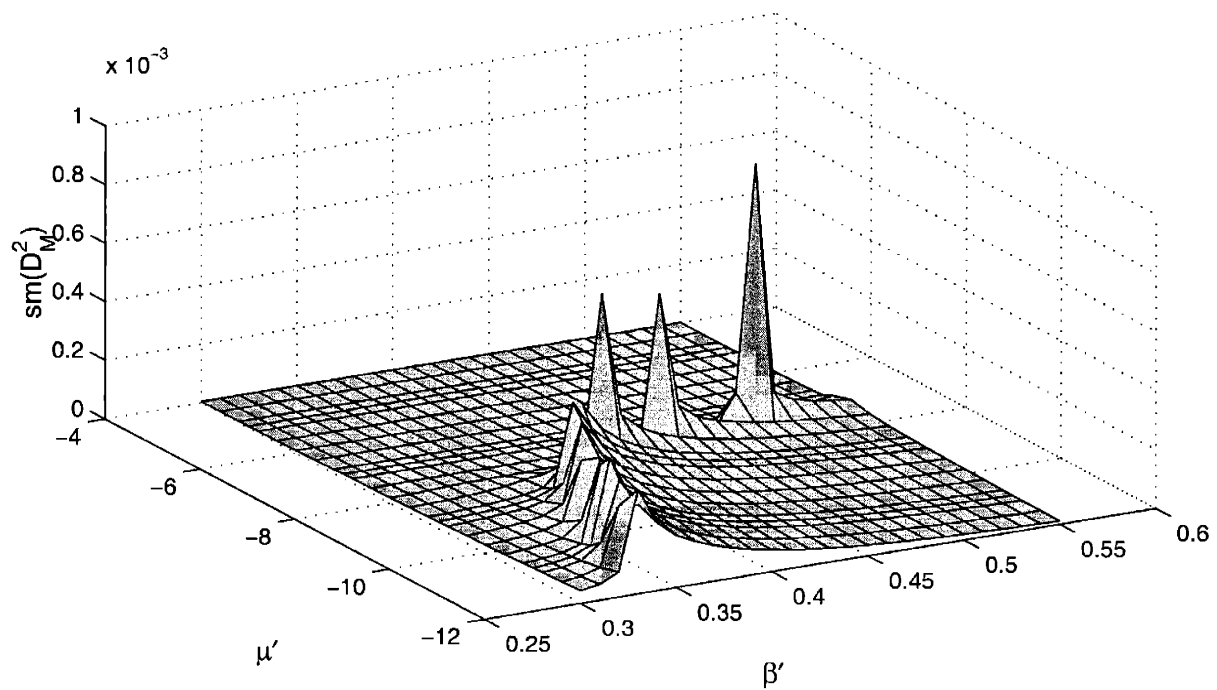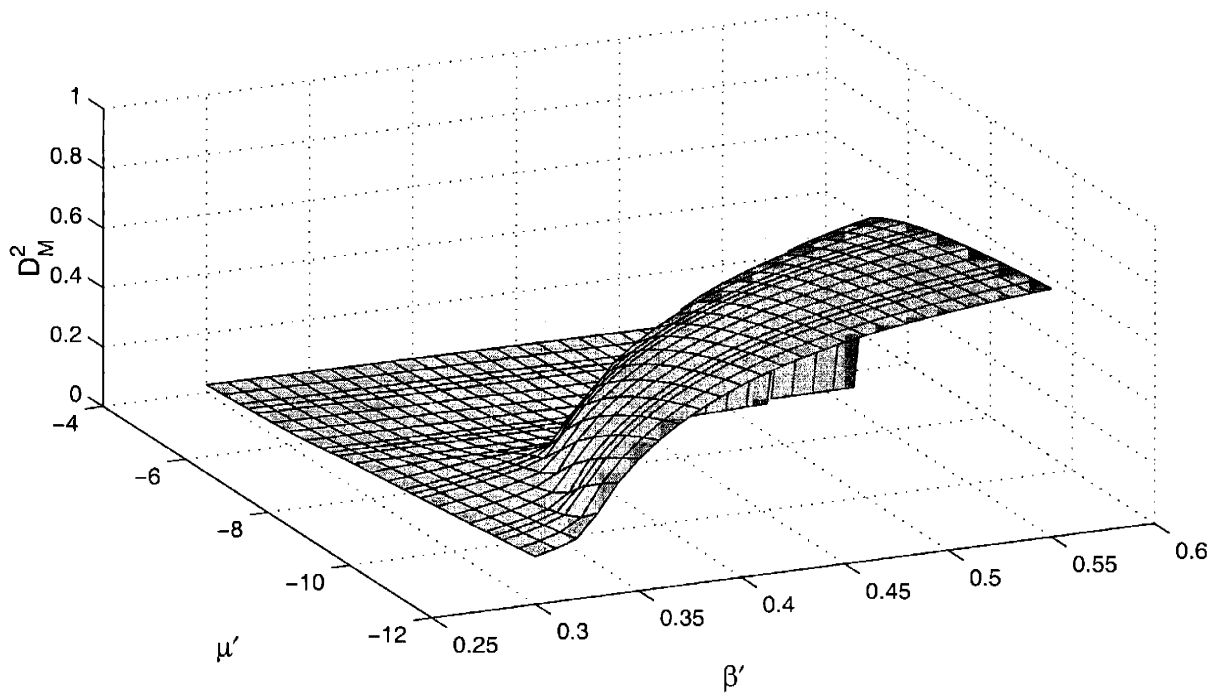
Figure 7-4: The mean dot product D_M (top) and its second moment (bottom) for the $SO(2) \otimes \mathbf{Z}_2$ system at $g' = 3$.
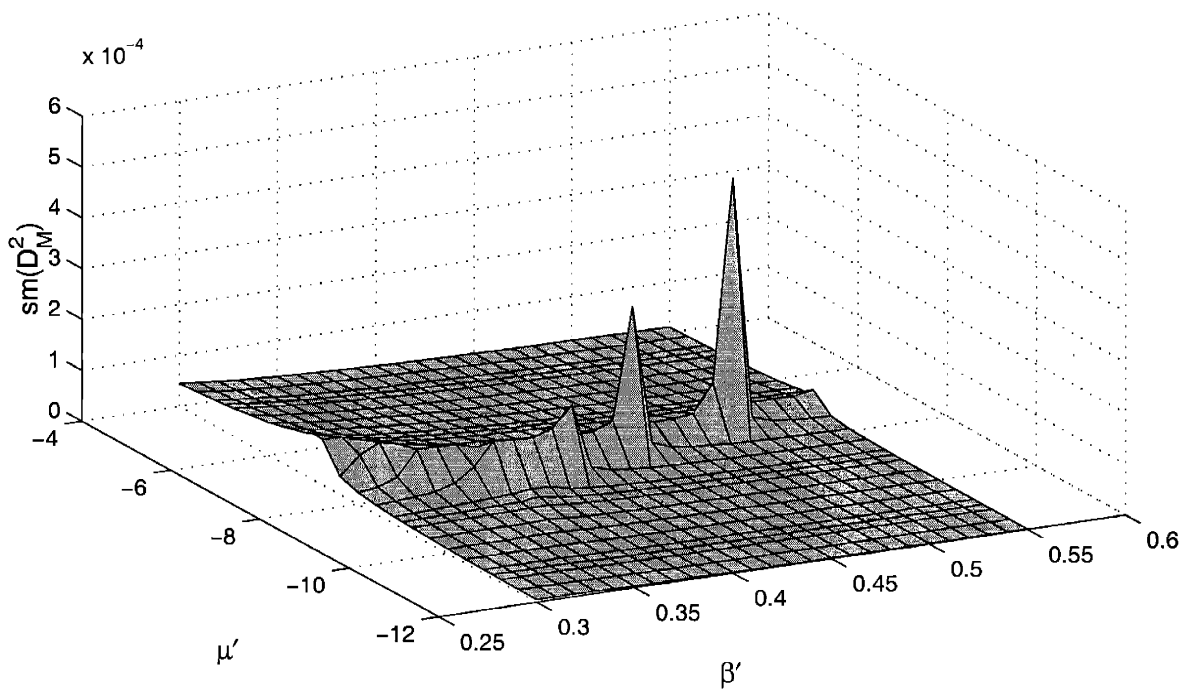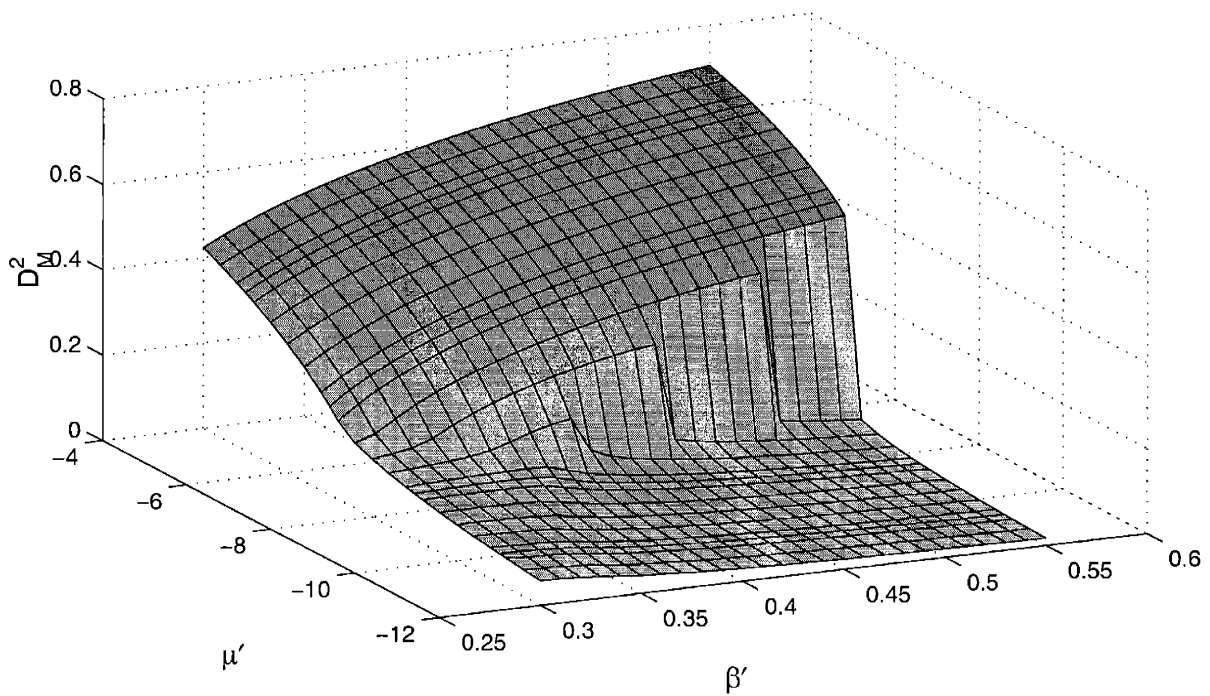
Figure 7-5: The mean dot product D_N (top) and its second moment (bottom) for the $SO(2) \otimes \mathbf{Z}_2$ system at $g' = 3$. A small secondary ridge coinciding with the $SO(M)$ ordering is visible here.
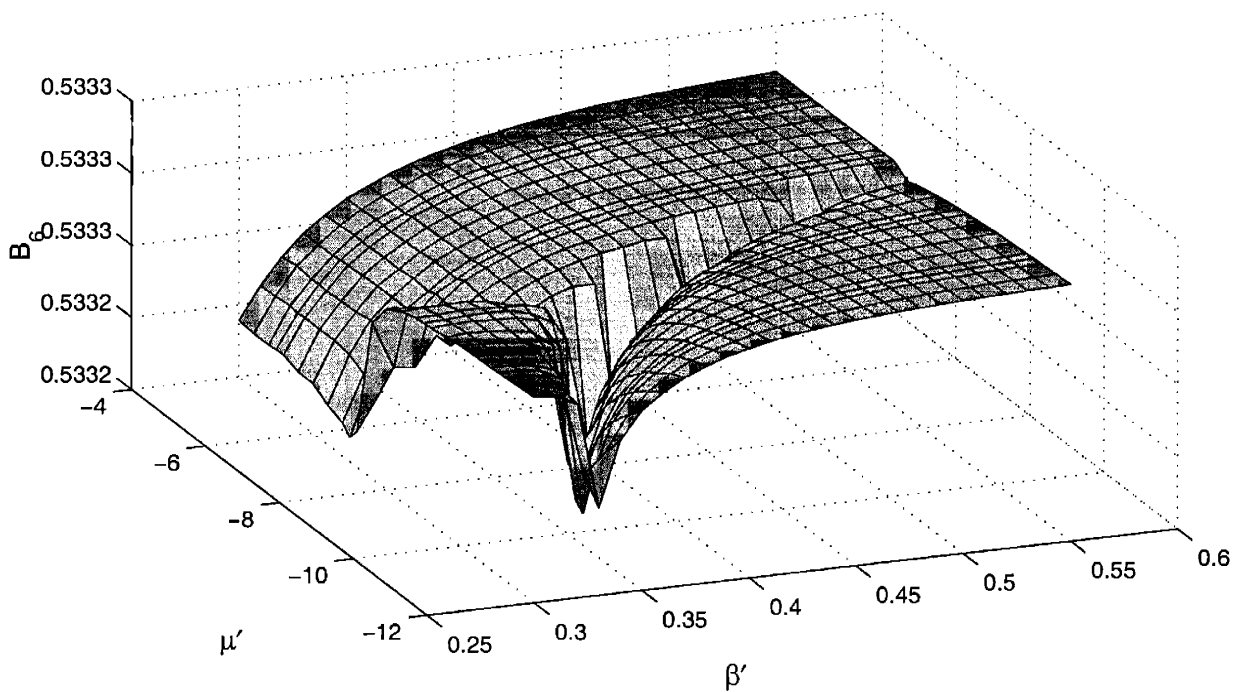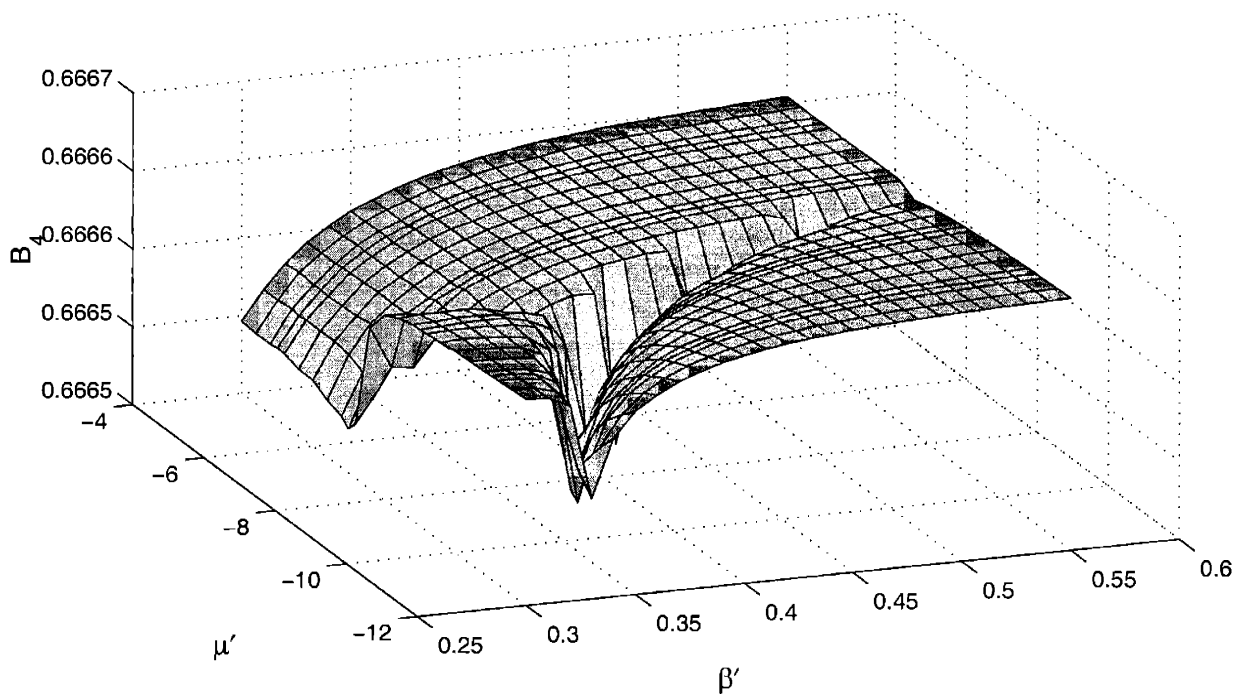
Figure 7-6: The Binder cumulants B_4 and B_6 for the $SO(2) \otimes \mathbf{Z}_2$ system at $g' = 3$ show a small but distinct signal at the phase boundaries. Note that both quantities appear to behave in the same fashion.

phase diagram depicted in Fig. 7-7. From this diagram, one can estimate that the
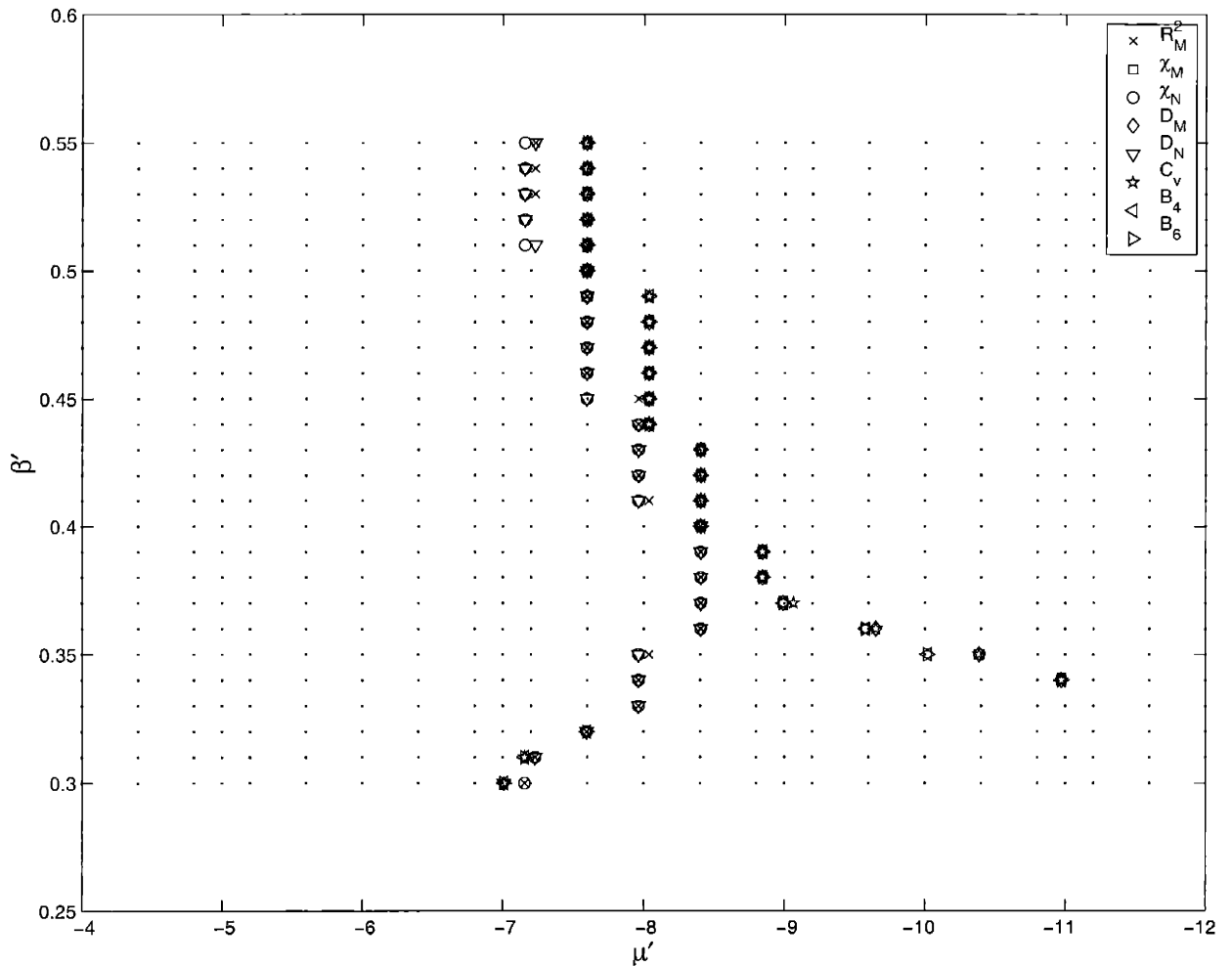
Figure 7-7: Phase diagram for the $SO(2) \otimes \mathbf{Z}_2$ system. The symbols denote the local extrema of the corresponding quantities, as explained in the text. The dots in the background of the figure are the points at which the simulation was run

expected bicritical point lies in the range $\beta'_c \in (3.8, 4.0)$ and $\mu'_c \in (-8.8, -8.4)$.

To refine this estimate for the bicritical point, it turns out that a much finer mesh in (β', μ') is needed. The crux of the problem is that the cross-over region has become so narrow already at $L = 20$ that the (β', μ') mesh shown in the plots above (and even a tenfold refinement thereof) is not enough to sample the (finite-size) coexistence region. If one can sample this region reliably, then analytical methods such as Ferrenberg and Swendsen's histogram reweighing technique[101, 102] can be

applied to determine with some accuracy the infinite-volume transition lines. An ideal run for which this method would work is shown in Fig. 7-8, where the tunneling back and forth between the two phases can be clearly seen. The histograms for the various observables, shown in Fig. 7-9, display the characteristic bimodal distribution associated with first order transitions. Unfortunately, not all runs along the estimated phase boundaries in Fig. 7-7 show this behavior. Quite frequently, the time series displays a long-lived metastable state decaying to another state, with no tunneling back even in an extended run; the histograms obtained in such a simulation are inherently unreliable.
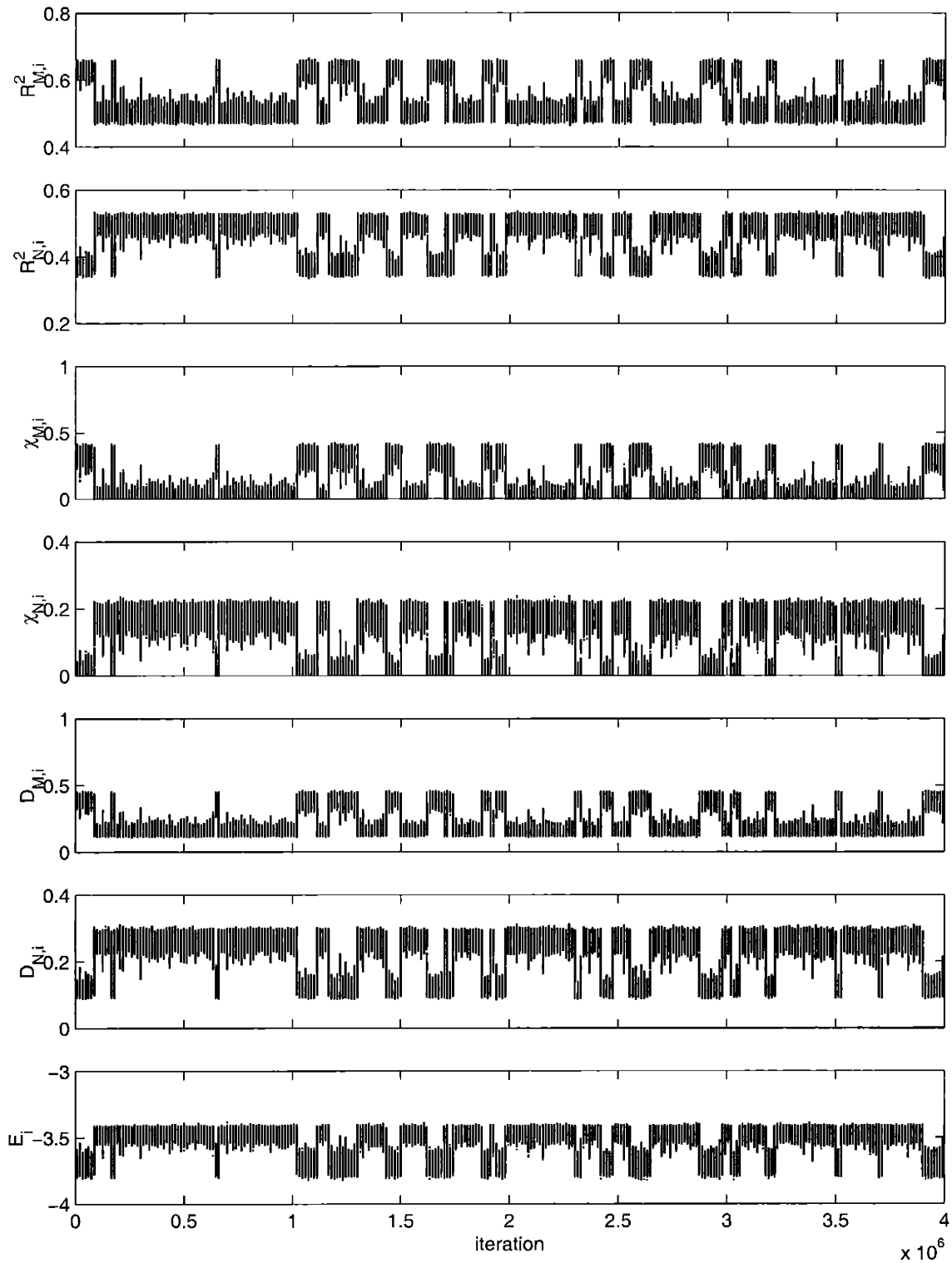
Figure 7-8: Time-series history near the first-order transition line for an $SO(2) \otimes \mathbb{Z}_2$ system at $\beta' = 0.42$ and $\mu' = -8.2$. This point shows the tunneling back and forth between states that is typical of the first-order transition. Unfortunately, most of the runs did not exhibit this ideal behavior, as explained in the text.
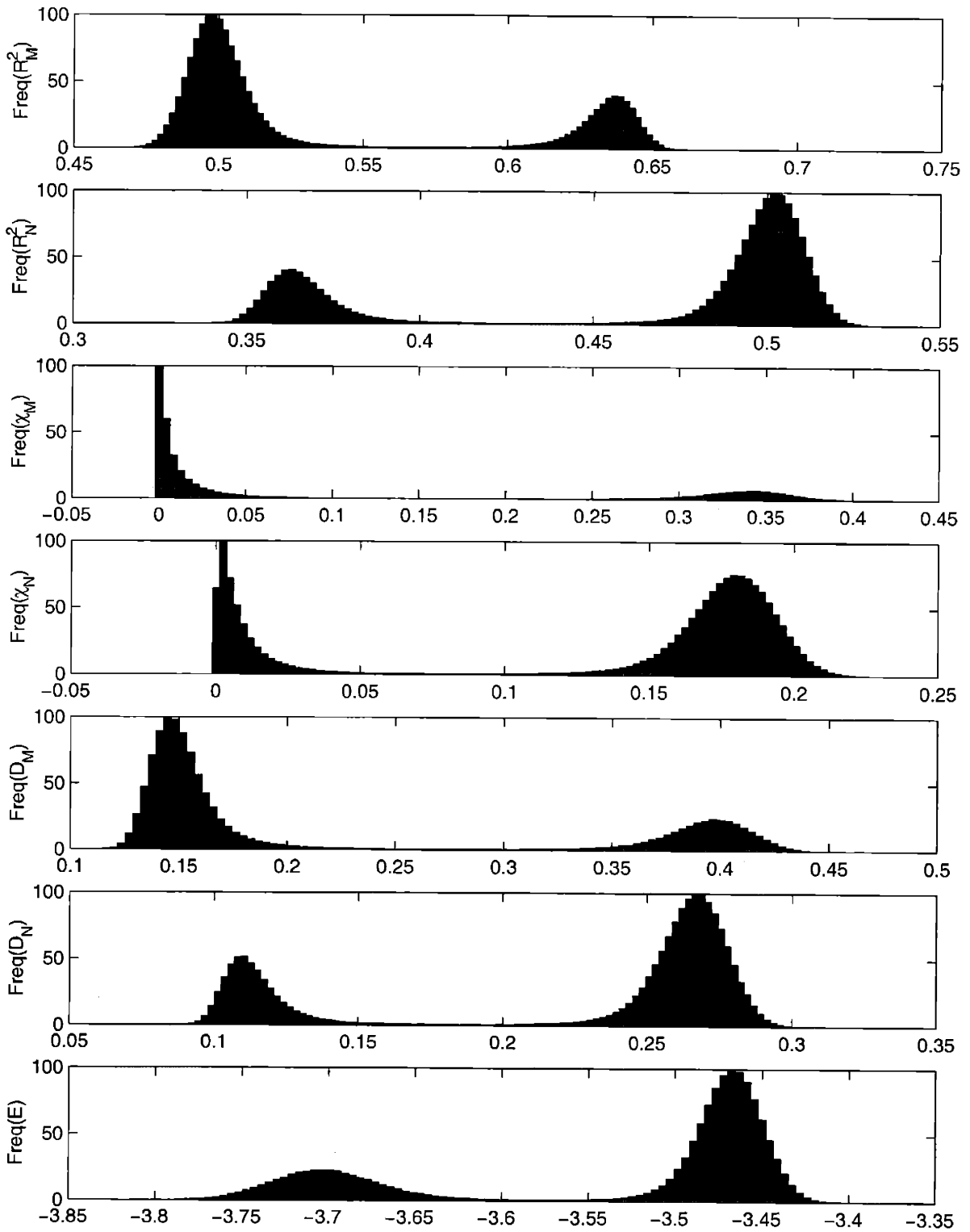
Figure 7-9: Bi-modal distributions near the first-order transition line. This distribution corresponds to the time series depicted in Fig.7-8, and can be used to interpolate the location of the (finite-size) first order line

7.3 Results for the $SO(2) \otimes SO(3)$ System

For the $SO(2) \otimes SO(3)$ system ($M = 2, N = 3$), I also ran simulations on a 20^3 lattice with 10^5 measurements at $g' = 3$. The (β', μ') mesh was finer here than in the $SO(2) \otimes \mathbb{Z}_2$ system, and the various phases are once again clearly visible. The second-moment signals show up quite distinctly in the plots for $R^2_{M,N}$ (Fig. 7-11) and $\chi_{M,N}$ (Figs. 7-12 and 7-13). An interesting feature here is the existence of a single point which dominates the second moment plots by an order of magnitude at $(\beta' = 0.8, \mu' = -7.0)$. This point also shows up as a large spike in the plots of B_4 and B_6, Fig. 7-14. By mapping the ridges in the observables, one obtains the general phase diagram once again, as shown in Fig. 7-10. The bicritical point appears to lie in the region $\beta'_c \in (0.700, 0.725)$ and $\mu'_c \in (-7.4, -7.2)$.
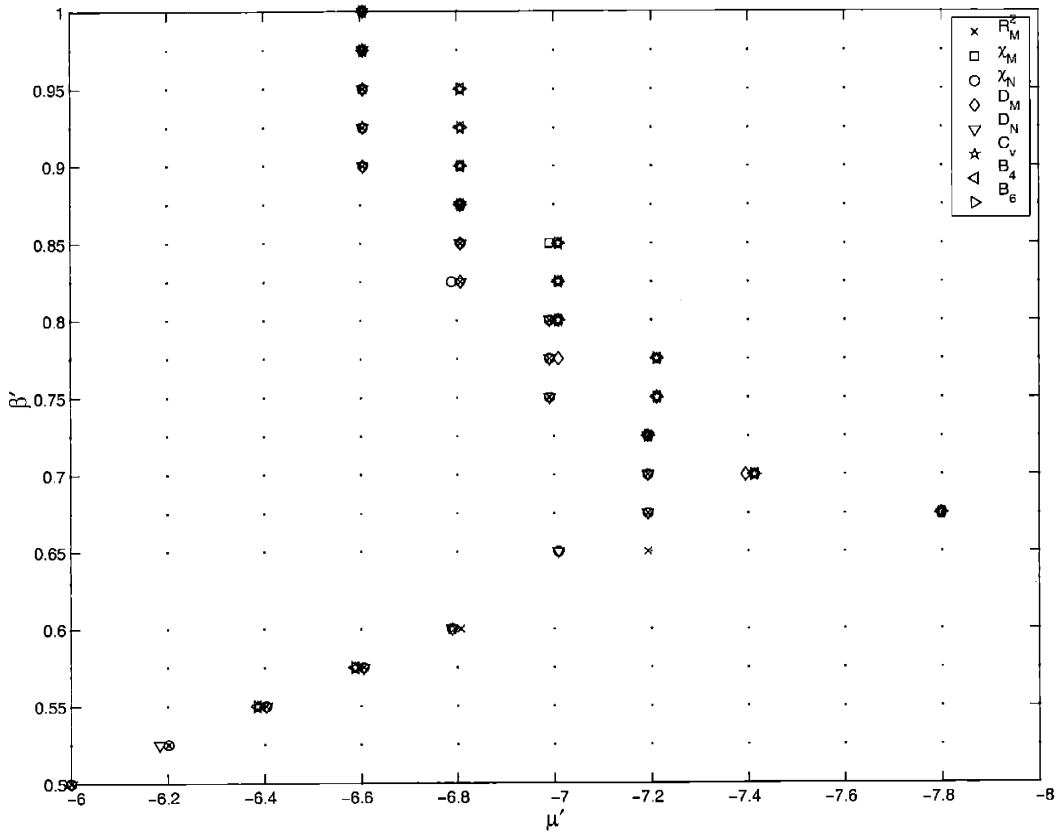
Figure 7-10: Phase diagram for $SO(2) \otimes SO(3)$ system at $g' = 3$.
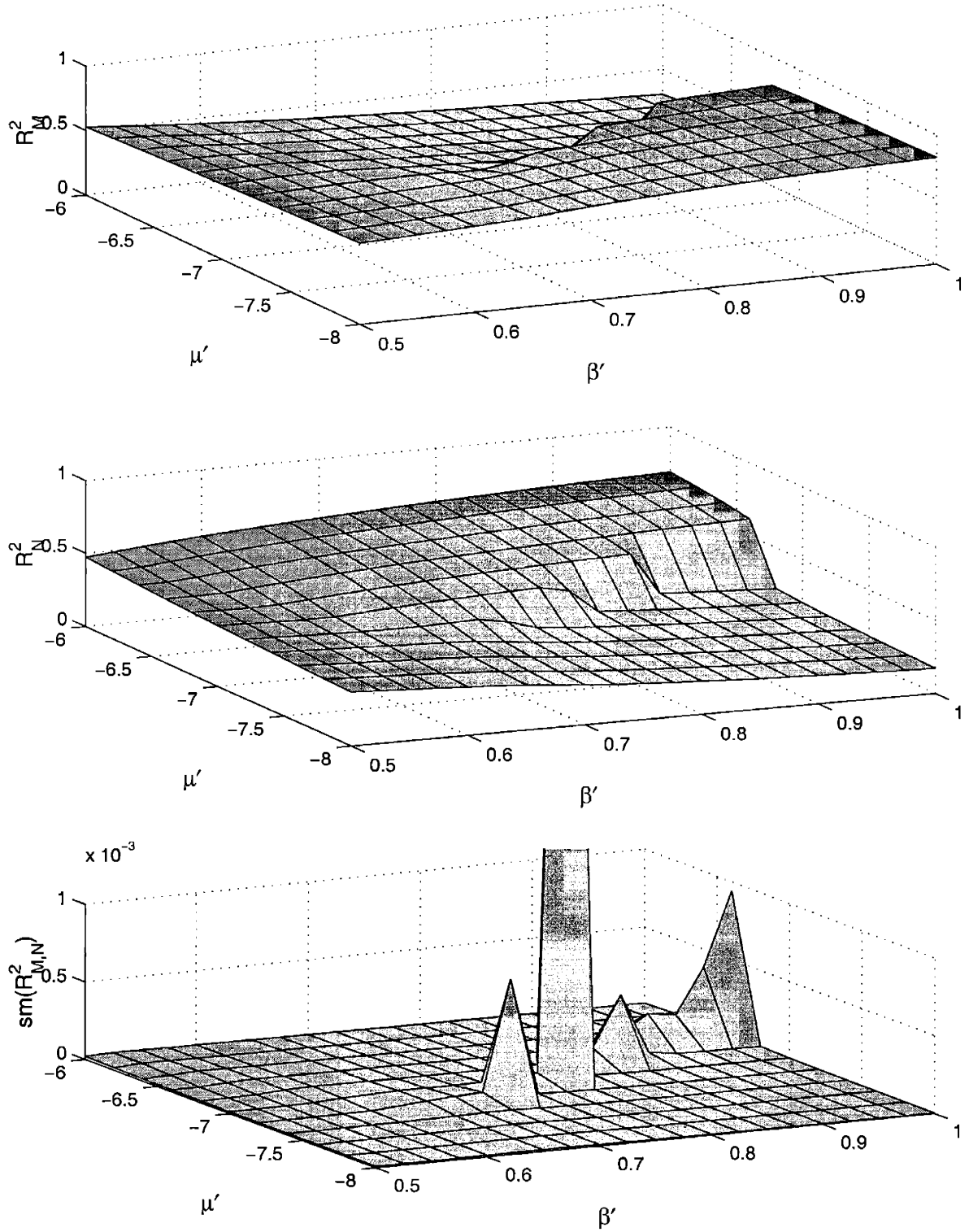
Figure 7-11: Mean lengths R_M^2 (top) and R_N^2 (middle), and their second moment (bottom) for $SO(2) \otimes SO(3)$ system at $g' = 3$.
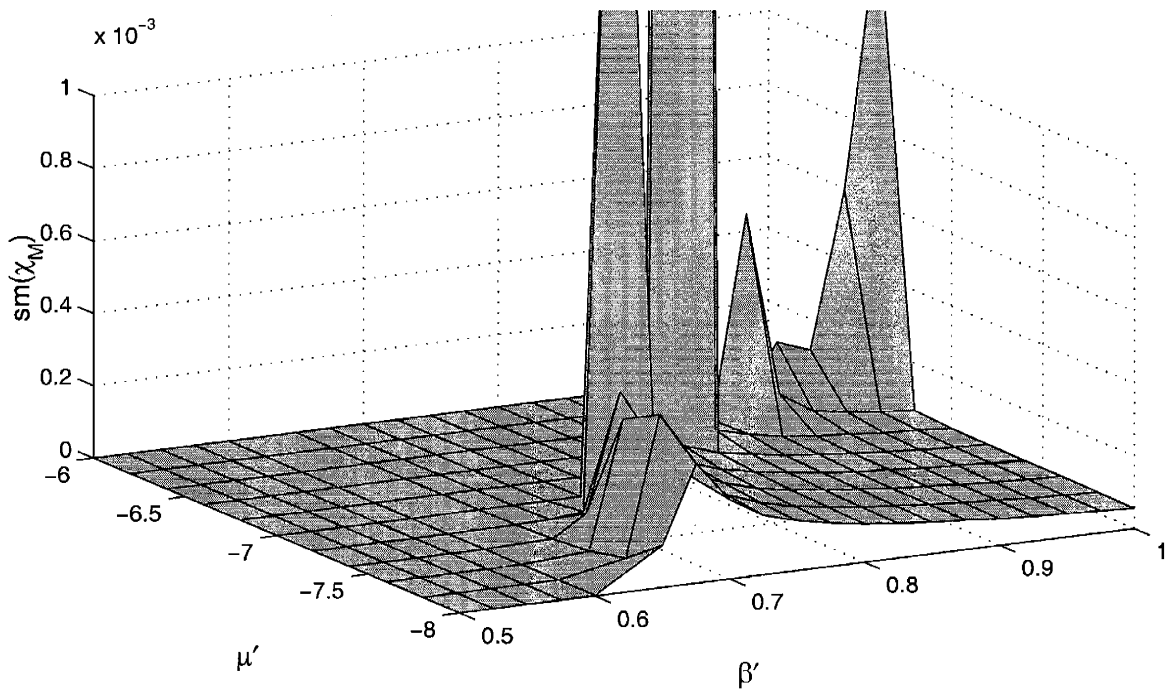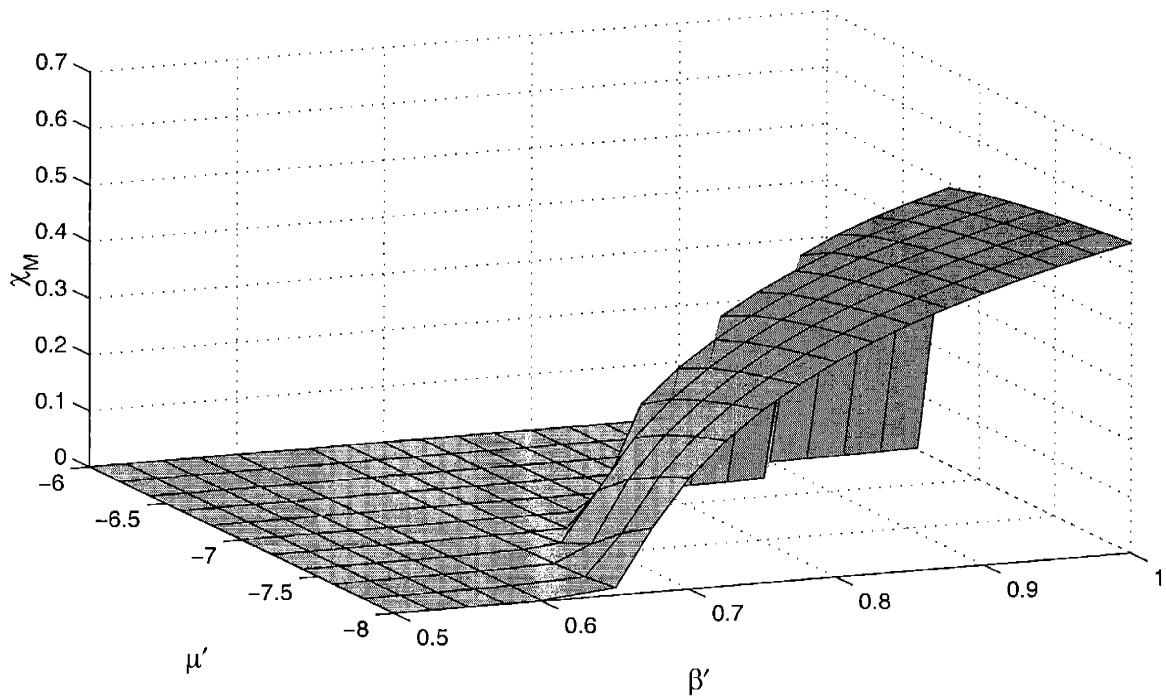
Figure 7-12: Susceptibility in $\mathbb{R}^M$ (top) and its second moment (bottom) for $SO(2) \otimes$ $SO(3)$ system at $g' = 3$. The plot for D_M has a similar structure.
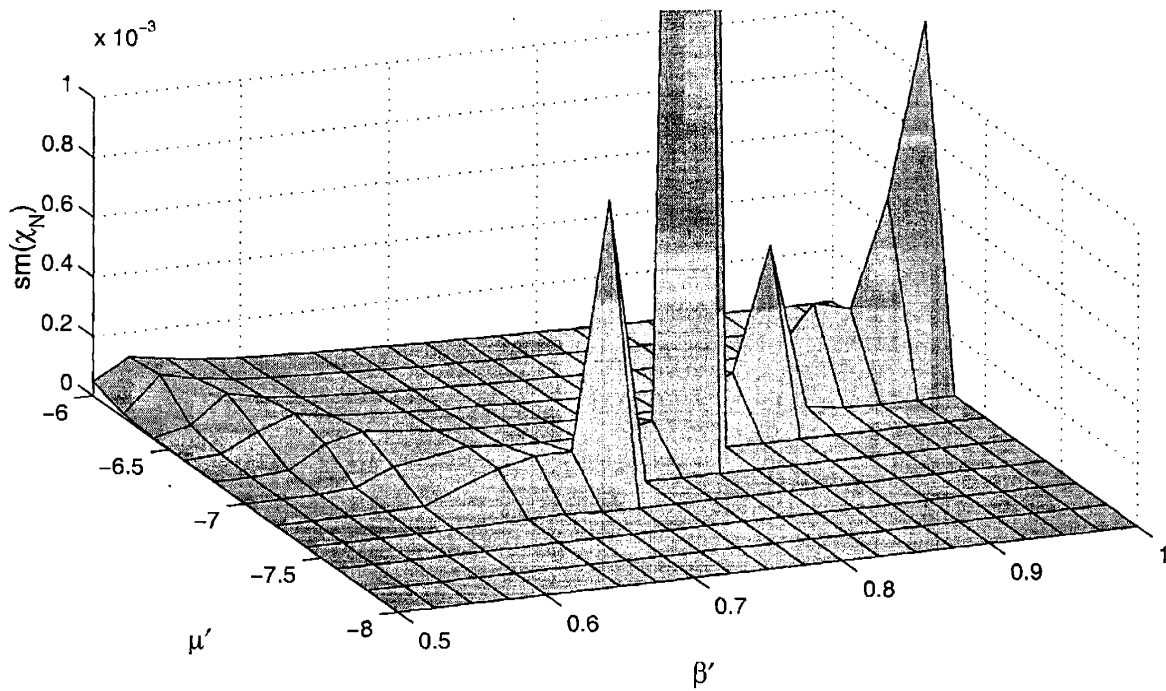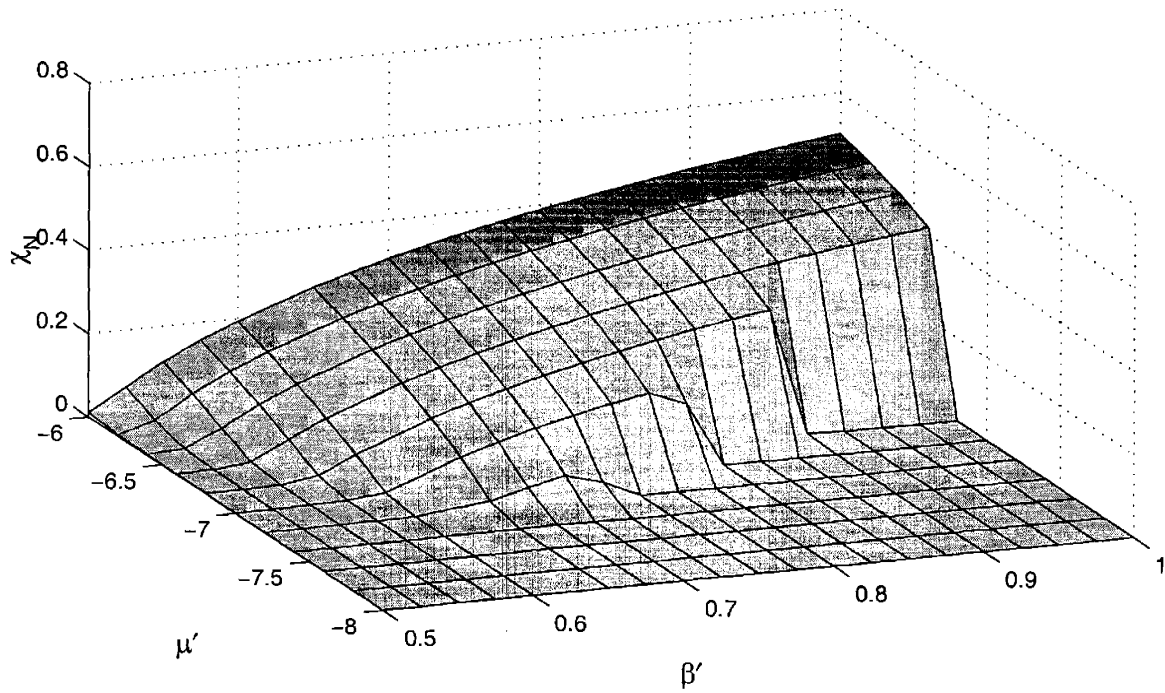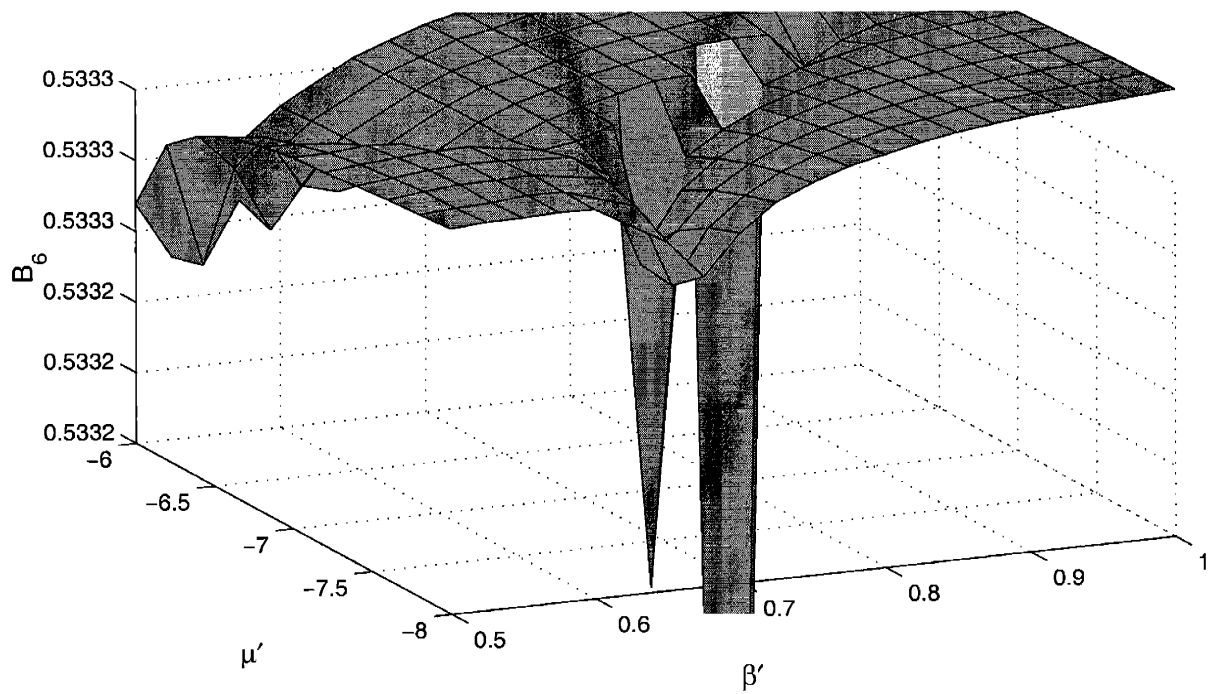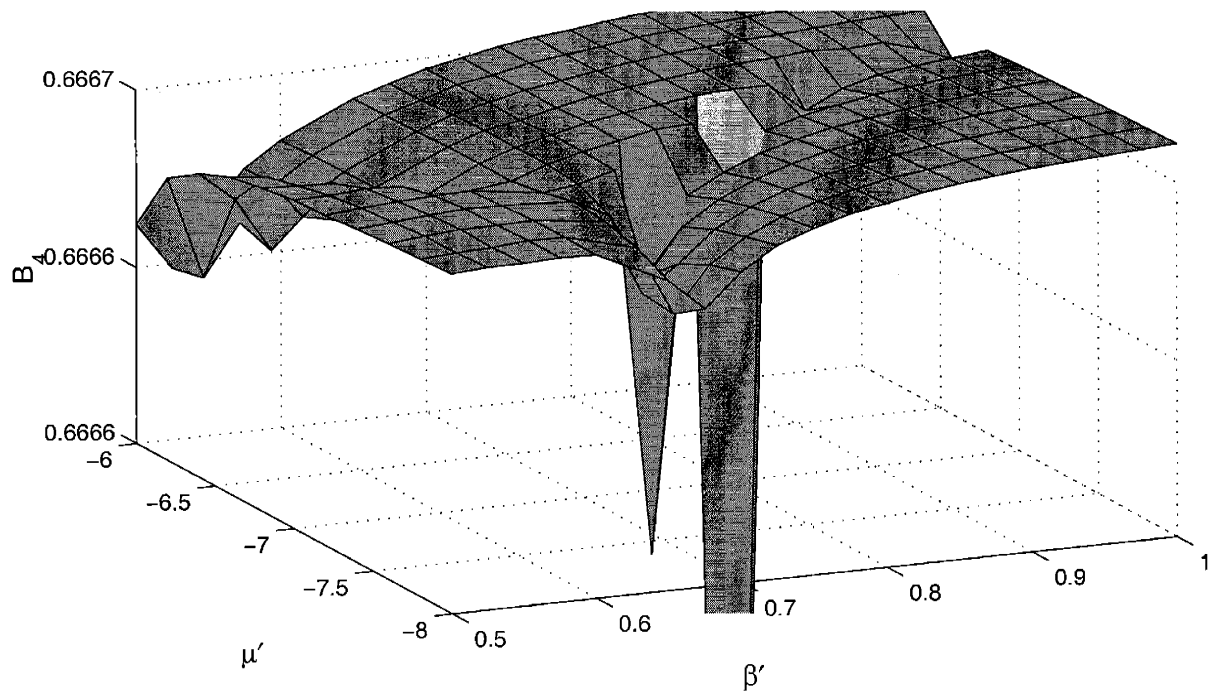
Figure 7-13: Susceptibility in $\mathbb{R}^N$ (top) and its second moment (bottom) for $SO(2) \otimes SO(3)$ system at $g' = 3$. The plot for D_N has a similar structure.

Figure 7-14: The Binder cumulants B_4 and B_6 for $SO(2) \otimes SO(3)$ system at $g' = 3$ also show a distinct signal at the phase transitions.

7.4 Results for the $SO(4) \otimes SO(6)$ System

I ran simulations of the $SO(4) \otimes SO(6)$ system ($M = 4, N = 6$) on a 10^3 lattice this time, but again with 10^5 measurements at $g' = 3$. While the $R^2_{M,N}$ plots (Figs. 7-16) look much the same as for the previous two systems, the second moment plots of $\chi_{M,N}$ (Figs. 7-17 and 7-18) display a characteristic "soufflé" shape— indicating that there are more fluctuations about the mean in the ordered phase than in the disordered phase. The plots for $D_{M,N}$ once again have the same structure as those for the susceptibilities. Interestingly, the plots of B_4 and B_6 (Fig. 7-19) do not show any significant structure except for a strange, pronounced dip at $(\beta' = 0.5, \mu' = 5)$. The data suggest the phase diagram depicted in Fig. 7-15, from which a reasonable estimate for the $L = 10$ bicritical point is $\beta'_c \in (1.40, 1.45)$ and $\mu'_c \in (-7.0, -6.4)$.
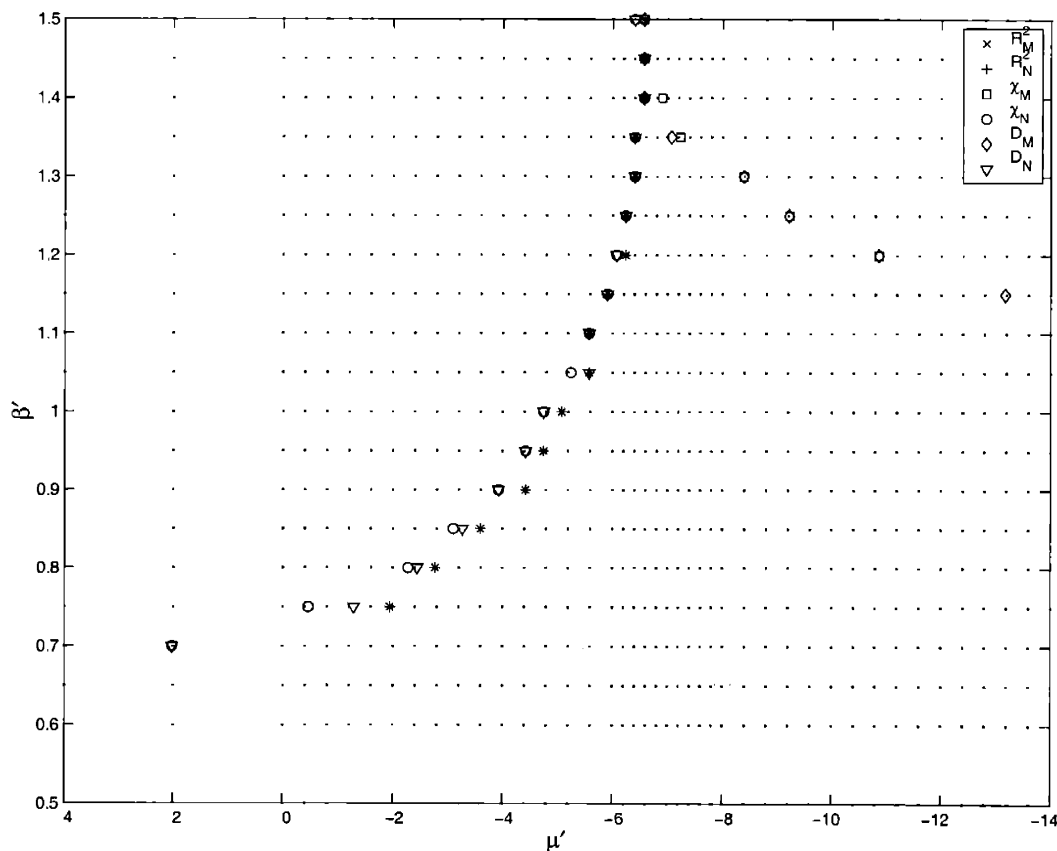

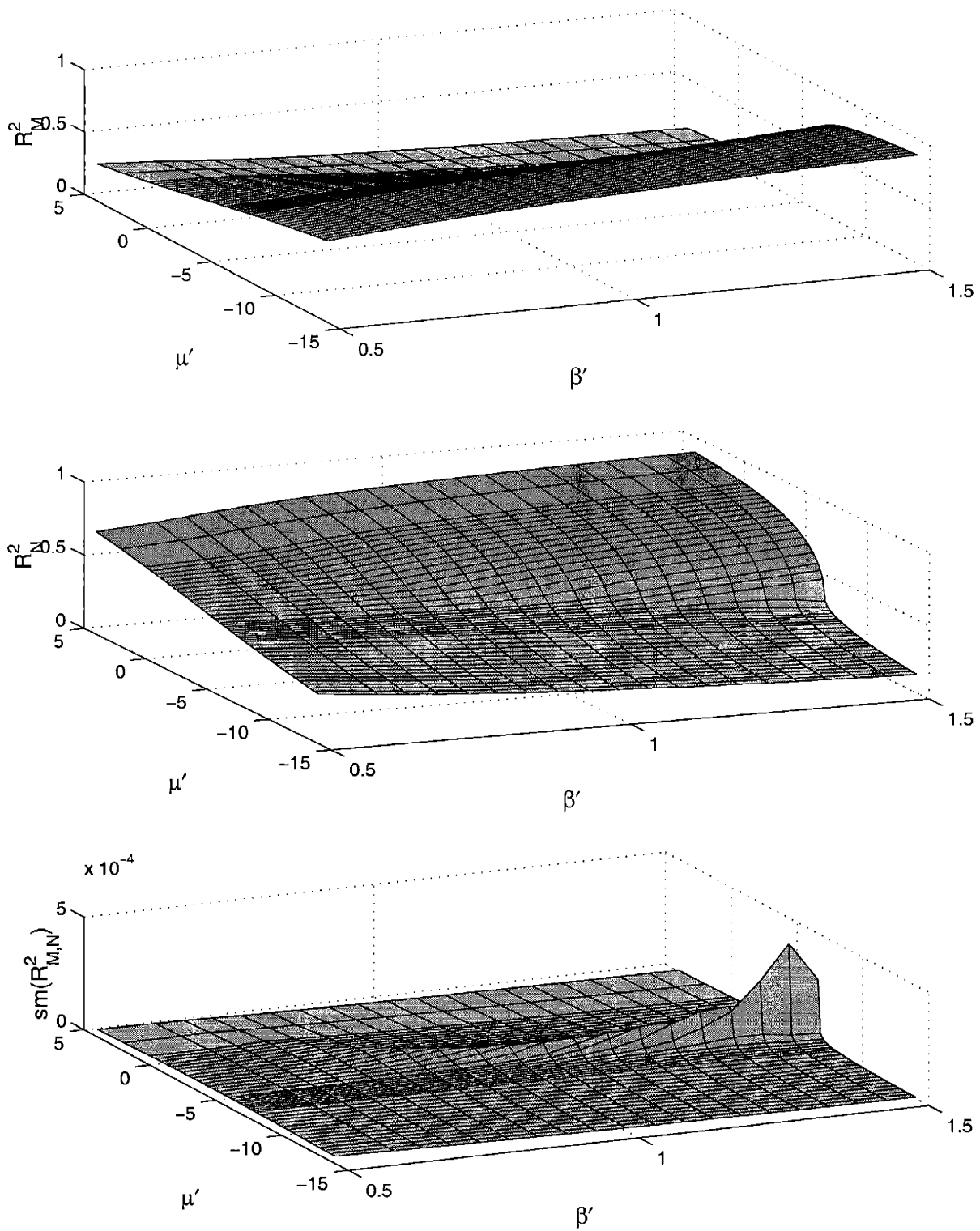Figure 7-15: Phase diagram for $SO(4) \otimes SO(6)$ system at $g' = 3$.

Figure 7-16: Mean lengths R_M^2 (top) and R_N^2 (middle), and their second moment (bottom) for $SO(4) \otimes SO(6)$ system at $g' = 3$.
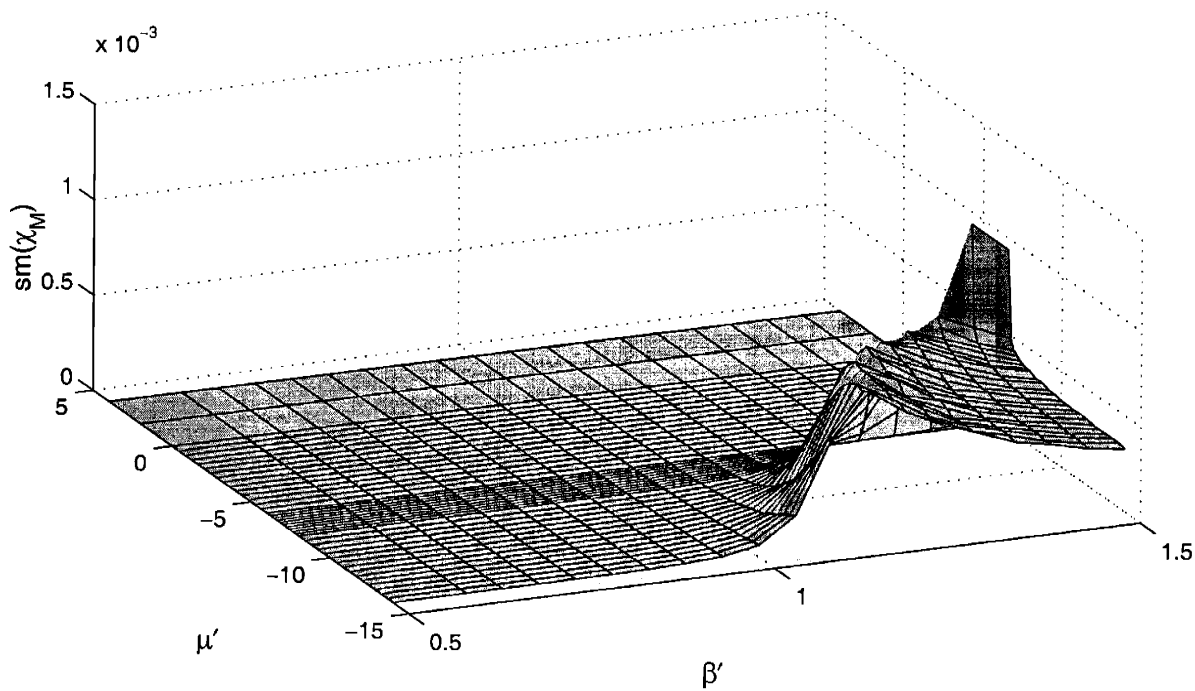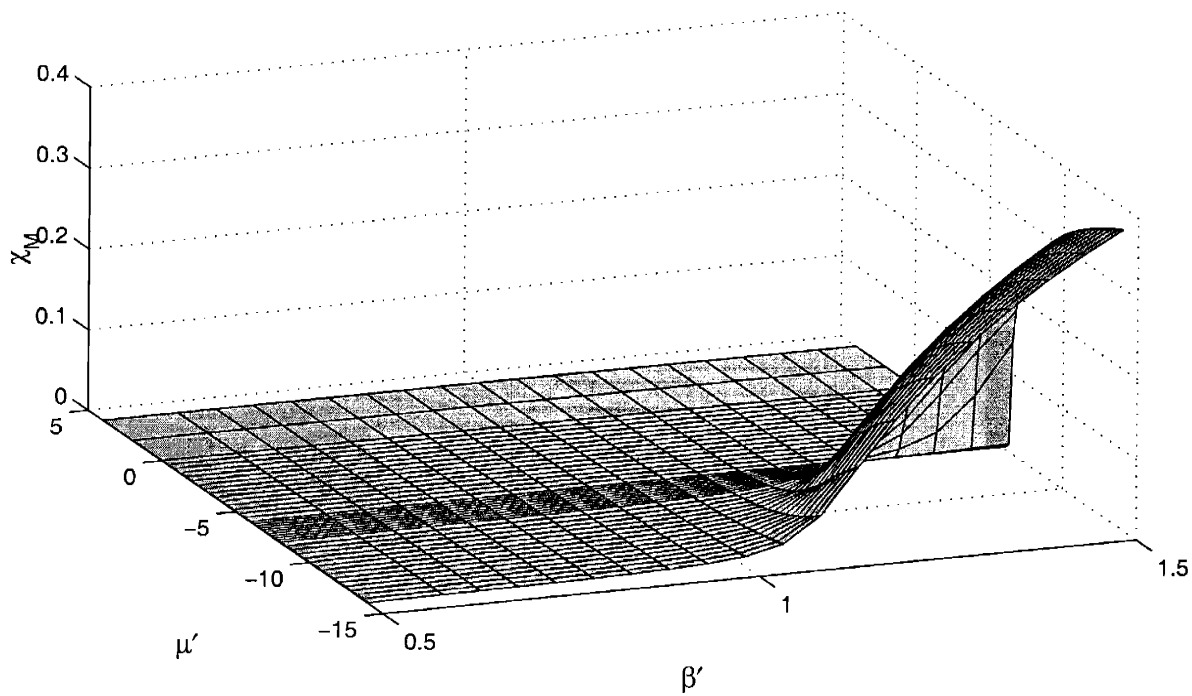
Figure 7-17: Susceptibility in $\mathbb{R}^M$ (top) and its second moment (bottom) for $SO(4) \otimes SO(6)$ system at $g' = 3$. The plot for D_M has a similar structure.
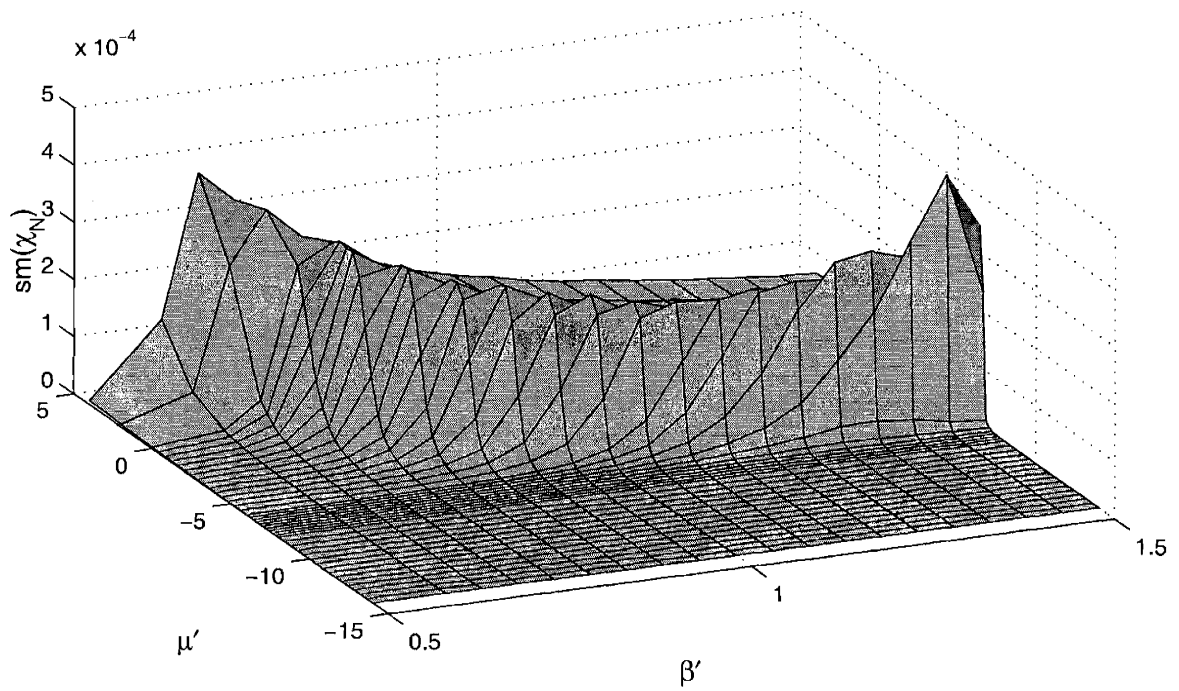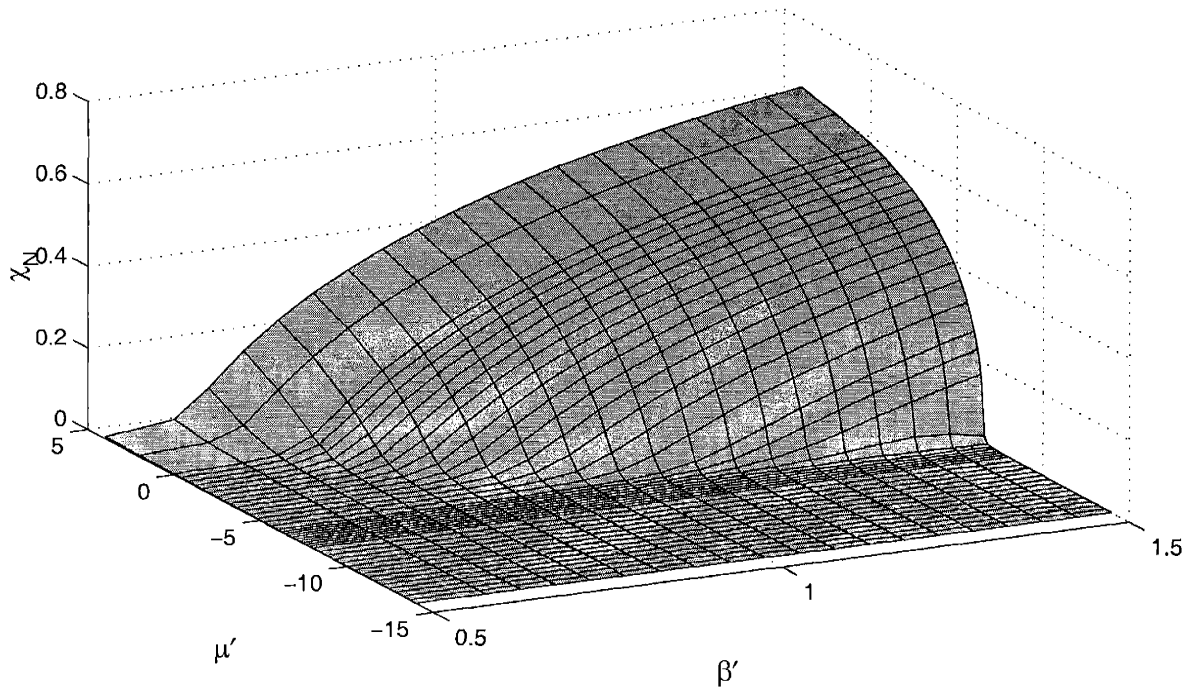
Figure 7-18: Susceptibility in $\mathbb{R}^N$ (top) and its second moment (bottom) for $SO(4) \otimes SO(6)$ system at $g' = 3$. The plot for D_N has a similar structure.
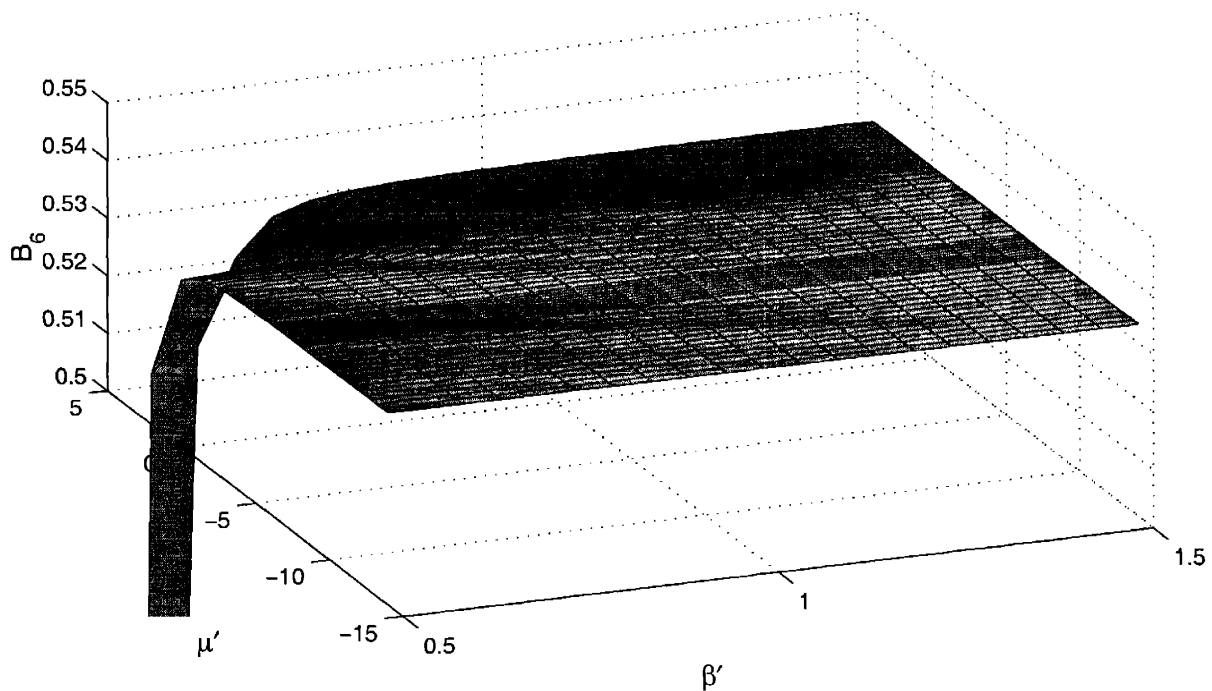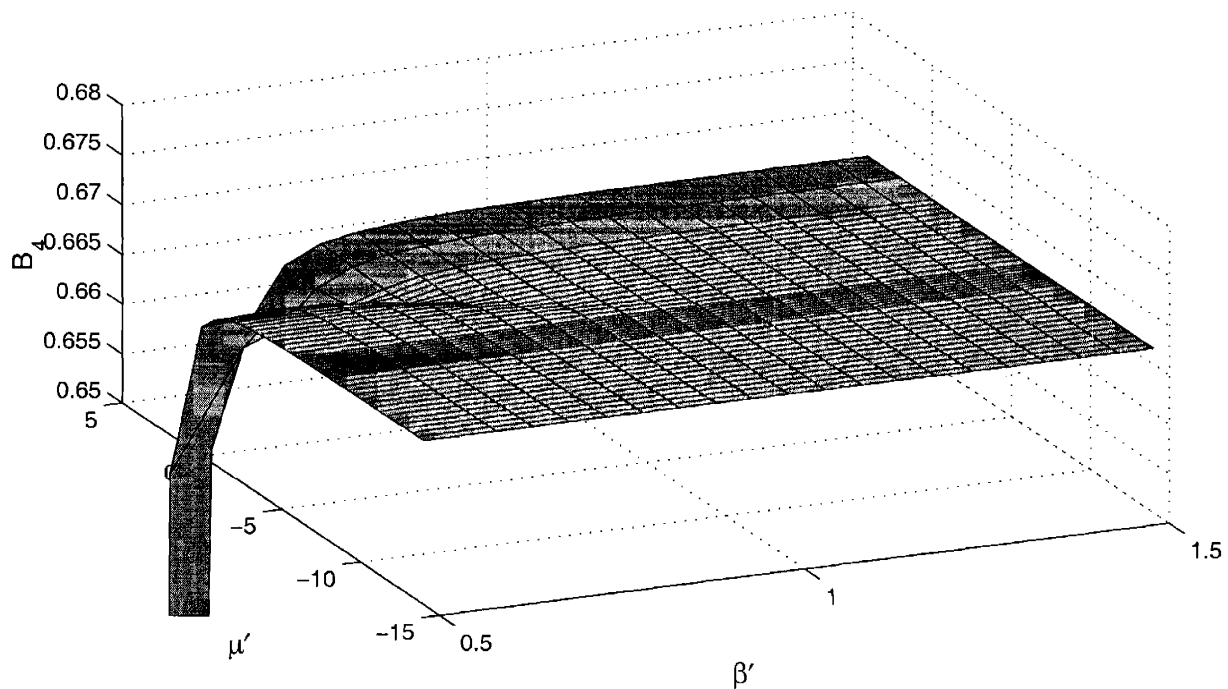
Figure 7-19: The Binder cumulants B_4 and B_6 for $SO(4) \otimes SO(6)$ system at $g' = 3$, interestingly enough, do not show a clear signal at the phase transitions but instead have an unexplained dip at one corner of the (β', μ') plane.

Chapter 8

Conclusion

In this dissertation, I have analyzed two strongly-coupled systems, the quantum Heisenberg antiferromagnet and the superspin magnet. Although the present work has provided significant insight into the nature of these two systems, much remains to be learned. The devil, as they say, is in the details.

In studying the antiferromagnetic Heisenberg model, we have confirmed numerically that the large spin-dependent discrepancies between the spin $S > 1/2$ correlation length ξ of the AFHM and its low-temperature description by the quantum field theory of the $d = 2$ $O(3)$ model are well explained by Hasenfratz's correction for cutoff effects in the spin model. With data fits of our quantum Monte Carlo results for spins $S = 1 - 5/2$ and $\xi/a \lesssim 10^5$, we found that the predictions of third-order spin-wave expansion for the spin stiffness and spin-wave velocity are nearly correct for $S = 1$, and for $S > 1$ are fully sufficient for the field-theoretical predictions to describe the correlation lengths from $\xi/a \sim 100$ up to $\xi/a \sim 10^5$.

We recovered scaling of the correlation length $\xi(L)$ in the AFHM according to the universal scaling function of the $O(3)$ model. This enabled us to achieve large infinite-volume correlation lengths from small finite-volume simulation data $\xi(L)$ with $L = 10 - 180$ using a finite-size scaling technique for the $O(3)$ model. Furthermore, this is a non-trivial support of the common assumption that the AFHM and the $O(3)$ model are in the same universality class. However, we showed that it is not the equal-time structure factor function $S(\mathbf{q})$ but the magnetic susceptibility function

$\chi(\mathbf{q})$ which enables universal scaling of the correlation length in the AFHM. This "time-averaged" correlation length is consistent with the $O(3)$ model scaling function, and the field-theoretical prediction up to extreme $\xi/a \sim 10^{30}$, and also with high-temperature series expansion for small $\xi/a \approx 0.5 - 10$.

Our QMC data connects consistently the regime of large and moderate correlation lengths, where the cutoff-corrected field-theoretical prediction applies, with the regime of small correlation lengths where high-temperature and semi-classical results apply. The diverse approaches are thereby reconciled. Furthermore, we showed that the remaining residual $\sim 10\%$ discrepancy between the field-theoretical prediction and ξ in the regime $\xi/a < 200$ of neutron scattering experiments has essentially reached the classical $S \to \infty$ limit at $S = 5/2$.

It would be interesting to continue the analysis of the AFHM by refining these fits. For example, one may continue the approach first used by Beard and Wiese for $S = 1/2$ and use susceptibility data to break the strong positive correlation between ρ_s and c. So, too, would it be interesting to measure the spatial susceptibility to obtain values for the low-energy parameters, and see how well they compare with the results obtained here.

Ultimately, of course, I come back to the original motivation. D-theory and cluster algorithms, which proved so useful for the antiferromagnet, promise to help us unravel the secrets of low-energy QCD. With the algorithmic know-how gained in the present project, I hope that my collaborators and I will, at some point, be able to successfully apply these ideas to gauge theories. We have made a valiant attempt to tackle the U(1) model, and yet we were stymied by an inefficiency that made the code, in practice if not in theory, not ergodic. We are still considering this problem, and hope to untangle it soon. Indeed, we are tantalized by having a D-theory formulation of QCD but not an efficient algorithm to implement it.

The simulations of the three related $SO(M) \otimes SO(N)$ systems reveal the existence of three phases, as expected. I was able to verify the existence of a flop transition, in which the spins jump discontinuously from $\mathbb{R}^M$ to $\mathbb{R}^N$, and to observed the more gradual (and, we expect, second-order) transitions from these ordered phases to the

disordered phase. It was gratifying to note that the various order parameters all agreed as to the location of the transition lines, leading to coherent, if somewhat coarse, finite-size phase diagrams.

From this phase diagram it is possible to estimate where the possible $SO(M+N)$ enhanced symmetry point lies; ultimately, one is interested in exploring whether Wiese and Chandrasekharan's arguments in $(4-\epsilon)$ dimensions hold in our 3-d world. There are several analytic techniques which may be used to extract answers from the Monte Carlo simulations. For example, Ferrenberg and Swendsen's histogram reweighing approach[101, 102] interpolates in the (β', μ') plane between the points where the simulations were actually run. To capture the correct physics of the phase transitions, however, the data files that are used as inputs to the reweighing calculation must sample both phases. As remarked above, though, quite often in my simulations there was no evidence that the system had settled comfortably in a crossover region— rather, there was a long lived transient state which would lead to incorrect predictions for the exact location of the transitions lines.

The next step, then, would be to simulate in a finer mesh so as to accurately capture the physics at the crossover regions. One could then obtain quite precise estimates for the transition lines, and start exploring the region of their intersection for enhanced symmetry. This latter could be handled, by, for example, Kolmogorov-Smirnov statistics[103] to see whether the distribution of a long-range observable (such as the susceptibility) in one of the subspaces follows the beta distribution $F_{M,N}(a^2)$ as one would expect if an $\mathbb{R}^{M+N}$ symmetry were generated dynamically. It is reasonable to expect that such an approach would finally answer whether this elegant model accurately reflects essential aspects of the fascinating physics of color superconductivity.

Bibliography

[1] K. G. Wilson, "Confinement of quarks," *Phys. Rev.* **D10** (1974) 2445–2459.

[2] U.-J. Wiese, "Quantum spins and quantum links: The d-theory approach to field theory," *Prog. Theor. Phys. Suppl.* **131** (1998) 483, hep-lat/9811025.

[3] R. Brower, S. Chandrasekharan, and U.-J. Wiese, "QCD as a quantum link model," *Phys. Rev.* **D60** (1999) 094502, hep-th/9704106.

[4] R. Brower, S. Chandrasekharan, and U.-J. Wiese, "Green's functions from quantum cluster algorithms," cond-mat/9801003.

[5] B. B. Beard *et al.*, "D-theory: Field theory via dimensional reduction of discrete variables," *Nucl. Phys. Proc. Suppl.* **63** (1998) 775–789, hep-lat/9709120.

[6] B. B. Beard and U.-J. Wiese, "Simulations of discrete quantum systems in continuous euclidean time," *Phys. Rev. Lett.* **77** (1996) 5130–5133.

[7] M. Harada, K. Troyer and N. Kawashima, "The two-dimensional S=1 quantum Heisenberg antiferromagnet at finite temperatures," *J. Phys. Soc. Jpn.* **67** (1998) 1130–1133, cond-mat/9712292.

[8] S. Chandrasekharan, B. Scarlet, and U.-J. Wiese, "Meron-cluster simulation of quantum spin ladders in a magnetic field," cond-mat/9909451.

[9] J. Cox, C. Gattringer, K. Holland, B. Scarlet, and U.-J. Wiese, "Meron-cluster solution of fermion and other sign problems," *Nucl. Phys. Proc. Suppl.* **83** (2000) 777–791, hep-lat/9909119.

[10] S. Chandrasekharan, J. Cox, K. Holland, and U.-J. Wiese, "Meron-cluster simulation of a chiral phase transition with staggered fermions," *Nucl. Phys.* **B576** (2000) 481–500, `hep-lat/9906021`.

[11] S. Chandrasekharan and U.-J. Wiese, "Meron-cluster solution of a fermion sign problem," *Phys. Rev. Lett.* **83** (1999) 3116–3119, `cond-mat/9902128`.

[12] S. Chandrasekharan, "Fermion cluster algorithms," *Nucl. Phys. Proc. Suppl.* **83** (2000) 774–776, `hep-lat/9909007`.

[13] B. Scarlet, *Solving Sign Problems with Meron Cluster Algorithms: Simulating Field Theories at Non-zero Chemical Potential.* PhD thesis, Massachusetts Institute of Technology, 2000.

[14] J. Cox, *Solution of sign and complex action problems with cluster algorithms.* PhD thesis, Massachusetts Institute of Technology, 2001.

[15] S.-C. Zhang, "A unified theory based on SO(5) symmetry of superconductivity and antiferromagnetism," *Science* **275** (1997) 1089–1096.

[16] B. B. Beard, V. Chudnovsky, and P. Keller-Marxer, "The spin correlation length in the antiferromagnetic two-dimensional square lattice O(3) quantum Heisenberg model for spins S=1/2-5/2 at low temperatures." In preparation.

[17] P. Keller-Marxer, *The Antiferromagnetic Square-Lattice O(3) Quantum Heisenberg Model for Spins $S = 1/2 - 5/2$ at Low Temperatures.* PhD thesis, University of Bern, 1999.

[18] B. B. Beard, V. Chudnovsky, and P. Keller-Marxer, "Reconciling the correlation length for high-spin Heisenberg antiferromagnets," *Nucl. Phys. Proc. Suppl.* **83** (2000) 682–684, `cond-mat/9910291`.

[19] S. Chandrasekharan, V. Chudnovsky, B. Schlittgen, and U. J. Wiese, "Flop transitions in cuprate and color superconductors: From so(5) to so(10)

unification?," *Nucl. Phys. Proc. Suppl.* **94** (2001) 449–452, arXiv:hep-lat/0011054.

[20] T. Barnes *Int. J. Mod. Phys* **C2** (1991) 659.

[21] E. Manousakis, "The spin-1/2 Heisenberg antiferromagnet on a square lattice and its application to the cuprous oxides," *Rev. Mod. Phys.* **63** (1991) 1–62.

[22] A. V. Chubukov and S. Sachdev, "Universal magnetic properties of $La_{2-\delta}Sr_\delta CuO_4$ at intermediate temperatures," *Phys. Rev. Lett.* **71** (1993) 169–172.

[23] A. V. Chubukov, S. Sachdev, and J. Ye, "Theory of two-dimensional quantum Heisenberg antiferromagnets with a nearly critical ground state," *Phys. Rev.* **B49** (1994) 11919–11961.

[24] N. Elstner, R. L. Glenister, R. R. P. Singh, and A. Sokol, "Scaling regimes, crossovers, and lattice corrections in two-dimensional Heisenberg antiferromagnets," *Phys. Rev.* **B51** (1995) 8984–8995.

[25] A. Sokol, N. Elstner, and R. R. P. Singh, "Crossover phase diagram of 2d Heisenberg ferro- and antiferromagnets," (95) cond-mat/9505148.

[26] N. Elstner *et al.*, "Spin dependence of correlations in two-dimensional square-lattice quantum Heisenberg antiferromagnets," *Phys. Rev. Lett.* **75** (1995) 938–941.

[27] S. Chakravarty, B. I. Halperin, and D. R. Nelson, "Two-dimensional quantum Heisenberg antiferromagnet at low temperatures," *Phys. Rev.* **B39** (1989) 2344–2371.

[28] H. Neuberger and T. Ziman, "Finite-size effects in Heisenberg antiferromagnets," *Phys. Rev.* **B39** (1989) 2608–2618.

[29] P. Hasenfratz and F. Niedermayer, "The exact correlation length of the antiferromagnetic d = (2+1) Heisenberg model at low temperatures," *Phys. Lett.* **B268** (1991) 231–235.

[30] P. Hasenfratz and H. Leutwyler, "Goldstone boson related finite size effects in field theory and critical phenomena with O(N) symmetry," *Nucl. Phys.* **B343** (1990) 241–284.

[31] P. Hasenfratz and F. Niedermayer *Z. Phys.* **B92** (1993) 91.

[32] M. Greven *Z. Phys* **B96** (1995) 465.

[33] B. B. Beard, R. J. Birgeneau, M. Greven, and U.-J. Wiese, "Square-lattice Heisenberg antiferromagnet at very large correlation lengths," *Phys. Rev. Lett.* **80** (1998) 1742–1745.

[34] K. Nakajima *Z. Phys* **B96** (1995) 479.

[35] Y. S. Lee *et al.*, "Spin correlations in the two-dimensional spin-5/2 Heisenberg antiferromagnet Rb_2MnF_4," *Eur. Phys. J.* **B5** (1998) 15–22.

[36] R. L. Leheny *et al.*, "Spin correlations in an isotropic spin-5/2 two-dimensional antiferromagnet," *Phys. Rev. Lett.* **82** (1999) 418–421, cond-mat/9809178.

[37] A. Cuccoli, V. Tognetti, P. Verrucchi, and R. Vaia, "Heisenberg antiferromagnet on the square lattice for $S \geq 1$," *Phys. Rev.* **58** (1998) 14151–14154.

[38] P. Hasenfratz, "The correlation length of the Heisenberg antiferromagnet with arbitrary spin S," *Eur. Phys. J.* **B13** (2000) 11–14, cond-mat/9901355.

[39] J. Neves and F. Peres *Phys. Lett.* **A114** (1986) 331.

[40] T. Barnes *Int. J. Mod. Phys* **C2** (1991) 659.

[41] U.-J. Wiese and H.-P. Ying *Z. Phys.* **93** (1994) 147.

[42] M. Greven *et al.*, "Spin correlations in the 2d Heisenberg antiferromagnet Sr$_2$CuO$_2$Cl$_2$: Neutron scattering, Monte Carlo simulation, and theory," *Phys. Rev. Lett.* **72** (1994) 1096–1099.

[43] J. Gasser and H. Leutwyler, "Chiral perturbation theory to one loop," *Ann. Phys.* **158** (1984) 142.

[44] N. D. Mermin and H. Wagner, "Absence of ferromagnetism or antiferromagnetism in one- or two-dimensional isotropic Heisenberg models," *Phys. Rev. Lett.* **17** (1966) 1133–1136.

[45] S. Coleman, "There are no Goldstone bosons in two-dimensions," *Commun. Math. Phys.* **31** (1973) 259–264.

[46] P. Hasenfratz, M. Maggiore, and F. Niedermayer, "The exact mass gap of the O(3) and O(4) nonlinear sigma models in d = 2," *Phys. Lett.* **B245** (1990) 522–528.

[47] P. Hasenfratz and F. Niedermayer, "The exact mass gap of the $O(N)$ sigma model for arbitrary N is >= 3 in $d = 2$," *Phys. Lett.* **B245** (1990) 529–532.

[48] S. Hikami and E. Brezin, "Three loop calculations in the two-dimensional nonlinear sigma model," *J. Phys.* **A11** (1978) 1141–1150.

[49] H.-P. Ying, U.-J. Wiese, and D.-R. Ji *Phys. Lett.* **A183** (1993) 441.

[50] K. Kim, J and M. Troyer, "Low temperature behavior and crossovers of the square lattice quantum Heisenberg antiferromagnet," *Phys. Rev. Lett* **80** (1998) 2705–2708.

[51] Z. Weihong, J. Oitmaa, and C. J. Hamer, "Square-lattice Heisenberg antiferromagnet at $T=0$," *Phys. Rev.* **B43** (1991) 8321–8330.

[52] J. Igarashi, "1/S expansion for thermodynamic quantities in a two-dimensional Heisenberg antiferromagnet at zero temperature," *Phys. Rev.* **B46** (1992) 10763–10771.

[53] C. Hamer, Z. Weihong, and J. Oitmaa, "Spin-wave stiffness of the Heisenberg antiferromagnet at zero temperature," *Phys. Rev.* **B50** (1994) 6877–6888.

[54] W. Zheng and C. J. Hamer, "Spin-wave theory and finite size scaling for the heisenberg antiferromagnet," *Phys. Rev.* **B47** (1993) 7961–1970.

[55] H. F. Trotter, "On the product of semi-groups of operators," *Proc. Am. Math. Soc* **10** (1959) 545–551.

[56] M. Suzuki, "Relationship between d-dimensional quantal spin systems and $(d+1)$-dimensional Ising systems," *Prog. Theor. Phys.* **56** (1976) 1454.

[57] N. Metropolis *et al.*, "Equations of state calculations by fast computing machines," *J. Chem. Phys.* **21** (1953) 1087.

[58] G. Bhanot, "The Metropolis algorithm," *Rep. Prog. Phys.* **51** (1988) 429–457.

[59] H. G. Evertz, "The loop algorithm," in *Numerical Methods for Lattice Quantum Many-Body Problems*, D. J. Scalapino, ed., Frontiers in Physics. Perseus Books, 2000. `cond-mat/9707221`.

[60] N. Kawashima and J. E. Gubernatis, "Loop algorithms for Monte Carlo simulations of quantum spin systems," *Phys. Rev. Lett.* **73** (1994) 1295–1298.

[61] N. Kawashima and J. E. Gubernatis *J. Stat. Phys.* **80** (1995) 169.

[62] B. B. Beard, V. Chudnovsky, P. Keller-Marxer, and C. Mochon. In preparation.

[63] The full set of correlation length data is available at http://www.cbu.edu/~bbbeard/highspin.htm.

[64] T. Jolicoeur and J. C. LeGuillou *Mod. Phys. Lett.* **5** (1991) 593.

[65] A. Sokol, N. Elstner, and R. R. P. Singh (1995) `cond-mat/9505148`.

[66] B. Allés, G. Cella, M. Dilaver, and Y. Gündüç, "Testing fixed points in the 2d O(3) nonlinear sigma model," *Phys. Rev. D.* **59** (1999) 067703.

[67] D.-S. Shin, "Correction to four-loop RG functions in the two-dimensional lattice $O(N)$ sigma-model," *Nucl. Phys.* **B546** (1999) 669–690, `hep-lat/9810025`.

[68] S. Caracciolo *et al.*, "Extrapolating Monte Carlo simulations to infinite volume: Finite-size scaling at $\xi/L \gg 1$," *Phys. Rev. Lett.* **74** (1995) 2969–2972.

[69] J.-K. Kim, "Asymptotic scaling of the mass gap in the two-dimensional O(3) nonlinear sigma model: A numerical study," *Phys. Rev.* **D50** (1994) 4663–4667.

[70] J.-K. Kim, "Application of finite size scaling to Monte Carlo simulations," *Phys. Rev. Lett.* **70** (1993) 1735–1738.

[71] S. Caracciolo, R. G. Edwards, A. Pelissetto, and A. D. Sokal, "Wolff type embedding algorithms for general nonlinear sigma models," *Nucl. Phys.* **B403** (1993) 475–541, `hep-lat/9205005`.

[72] M. S. Makivić and H. Q. Ding, "Two-dimensional spin-1/2 Heisenberg antiferromagnet: A quantum Monte Carlo study," *Phys. Rev.* **B43** (1991) 3562–3574.

[73] A. Sokol, R. R. P. Singh, and N. Elstner, "sotropic spin-wave theory of short-range magnetic order," *Phys. Rev. Lett.* **76** (1996) 4416–4419.

[74] N. Elstner *et al.*, "Scaling regimes, crossovers, and lattice corrections in two-dimensional Heisenberg antiferromagnets," *Phys. Rev.* **B51** (1995) 8984–8995.

[75] H. Flyvbjerg, "Some exact results for the $O(N)$ symmetric nonlinear sigma model to $O(1/N)$," *Nucl. Phys.* **B348** (1991) 714–736.

[76] P. Biscari, M. Campostrini, and P. Rossi, "Quantitative picture of the scaling behavior of lattice nonlinear sigma models from the 1/n expansion," *Phys. Lett.* **B242** (1990) 225–233.

[77] M. Campostrini, A. Pelissetto, P. Rossi, and E. Vicari, "On the evaluation of universal non-perturbative constants in $O(N)$ sigma models," *Phys. Lett.* **B402** (1997) 141–146, `hep-lat/9702010`.

[78] A. V. Chubukov and A. O. Starykh, "On the behaviour of a two-dimensional Heisenberg antiferromagnet at very low temperatures," *J. Phys.: Condens. Matter* **11** (1999) L169–L174.

[79] J. Balog *et al.*, "Comparison of the O(3) bootstrap sigma model with lattice regularization at low energies," *Phys. Rev.* **D60** (1999) 094508.

[80] M. B. Priestley, *Spectral Analysis and Time Series.* Academic Press, 1981.

[81] T. W. Anderson, *The Statistical Analysis of Time Series.* Wiley, 1971.

[82] J. D. Hamilton, *Time Series Analysis.* Princeton University Press, 1994.

[83] N. Madras and A. D. Sokal *J. Stat. Phys* **50** (1987) 109.

[84] A. D. Sokal, "Bosonic algorithms," in *Quantum Fields on the Computer,* M. Creutz, ed. World Scientific, 1992.

[85] R. M. Neal, *Probabilistic Inference Using Markov Chain Monte Carlo Methods.* 1993.

[86] R. Schlittgen and H. J. Streitberg, *Zeitreihenanalyse.* Oldenbourg, 1995.

[87] H. Flyvbjerg, "Error estimates on averages of correlated data," in *Advances in Computer Simulation,* no. 501 in Lecture Notes in Physics. Springer, 1996.

[88] D. Bailin and A. Love, "Superfluidity and superconductivity in relativistic fermion systems," *Phys. Rept.* **107** (1984) 325.

[89] M. Alford, K. Rajagopal, and F. Wilczek, "QCD at finite baryon density: Nucleon droplets and color superconductivity," *Phys. Lett.* **B422** (1998) 247–256, `hep-ph/9711395`.

[90] R. Rapp, T. Schafer, E. V. Shuryak, and M. Velkovsky, "Diquark Bose condensates in high density matter and instantons," *Phys. Rev. Lett.* **81** (1998) 53–56, hep-ph/9711396.

[91] M. E. Fisher and D. R. Nelson, "Spin flop, supersolids, and bicritical and tetracritical points," *Phys. Rev. Lett* **32** (1974) 1350–1353.

[92] S. Chandrasekharan and U.-J. Wiese, "SO(10) unification of color superconductivity and chiral symmetry breaking?," hep-ph/0003214.

[93] M. Alford, K. Rajagopal, and F. Wilczek, "Color-flavor locking and chiral symmetry breaking in high density QCD," *Nucl. Phys.* **B537** (1999) 443–458, hep-ph/9804403.

[94] T. Schäfer and F. Wilczek, "Continuity of quark and hadron matter," *Phys. Rev. Lett.* **82** (1999) 3956–3959, hep-ph/9811473.

[95] T. Schäfer and F. Wilczek, "Quark description of hadronic phases," *Phys. Rev.* **D60** (1999) 074014, hep-ph/9903503.

[96] S. L. Adler, "Over-relaxation method for the monte carlo evaluation of the partition function for multiquadratic actions," *Phys. Rev.* **D23** (1981) 2901–2904.

[97] F. R. Brown and T. J. Woch, "Overrelaxed heat-bath and metropolis algorithms for accelerating pure gauge monte carlo calculations," *Phys. Rev. Lett.* **58** (1987) 2394–2396.

[98] R. C. H. Cheng, "Generating beta variates with nonintegral shape parameters," *Comm. ACM* **21** (1978) 317–322.

[99] K. Binder, "Critical properties from monte carlo coarse graining and renormalization," *Phys. Rev. Lett.* **47** (1981) 693–696.

[100] M. S. S. Challa, D. P. Landau, and K. Binder, "Finite-size effects at temperature-driven first-order transitions," *Phys. Rev.* **B34** (1986) 1841–1852.

[101] A. M. Ferrenberg and R. H. Swendsen, "New Monte Carlo technique for studying phase transitions," *Phys. Rev. Lett.* **61** (1988) 2635–2638.

[102] A. M. Ferrenberg and R. H. Swendsen, "Optimized Monte Carlo data analysis," *Phys. Rev. Lett.* **63** (1989) 1195–1198.

[103] W. H. Press, S. A. Teukolsky, and W. T. Vetterling, *Numerical Recipes in C,* ch. Statistical Description of Data. Cambridge University Press, 1992. Available at http://www.nr.com/.

Index

algorithm

    cluster, 11, 33

        continuous time, 35

        higher spin, 37

        improved estimators, 12, 42

    Metropolis, 32

    modified microcanonical overrelaxation, 77

    radius metropolis, 79

    Wolff, 74

beta distribution, 80

Binder cumulants, 84

CH_2N_2 formula, 23

CH_3N_2B formula, 26

chiral perturbation theory, 21

chiral symmetry, 14

correlation length

    equal-time, 57

    reconciles various regimes, 64

    second-moment definition of, 57

    time-averaged, 58

CPT, *see* chiral perturbation theory

dimensional reduction, 11

finite-size scaling, 54

Heisenberg model

    3-d $O(3)$ effective theory for, 21

    cutoff effects in, 23, 25, 50

    dimensionally reduced 2-d $O(3)$ effective theory for, 21

    motivation for, 13, 18

    quantum Hamiltonian for, 20

high-temperature expansion, 62

histogram reweighing technique, 92

HTE, *see* high-temperature expansion

importance sampling, 31

internal energy, 83

Kolmogorov-Smirnov statistics, 108

mean dot product, 83

mean lengths, 83

"Memphis chart", 44

Mermin-Wagner-Coleman theorem, 21

$O(3)$ model

    correlation length of, 22, *see* CH_2N_2 formula

    exact mass gap of, 22

plaquette, 29